

REPORT DOCUMENTATION PAGE			Form Approved OMB NO. 0704-0188		
<p>The public reporting burden for this collection of information is estimated to average 1 hour per response, including the time for reviewing instructions, searching existing data sources, gathering and maintaining the data needed, and completing and reviewing the collection of information. Send comments regarding this burden estimate or any other aspect of this collection of information, including suggestions for reducing this burden, to Washington Headquarters Services, Directorate for Information Operations and Reports, 1215 Jefferson Davis Highway, Suite 1204, Arlington VA, 22202-4302. Respondents should be aware that notwithstanding any other provision of law, no person shall be subject to any penalty for failing to comply with a collection of information if it does not display a currently valid OMB control number.</p> <p>PLEASE DO NOT RETURN YOUR FORM TO THE ABOVE ADDRESS.</p>					
1. REPORT DATE (DD-MM-YYYY) 24-04-2015		2. REPORT TYPE MS Thesis		3. DATES COVERED (From - To) -	
4. TITLE AND SUBTITLE PERFORMANCE EVALUATION OF AN AIR-COUPLED PHASED-ARRAY RADAR FOR NEAR-FIELD DETECTION OF STEEL			5a. CONTRACT NUMBER W911NF-13-1-0301		
			5b. GRANT NUMBER		
			5c. PROGRAM ELEMENT NUMBER 611103		
6. AUTHORS Jonathan Razinger			5d. PROJECT NUMBER		
			5e. TASK NUMBER		
			5f. WORK UNIT NUMBER		
7. PERFORMING ORGANIZATION NAMES AND ADDRESSES University of Vermont 85 South Prospect Street, 340 Waterman Building Burlington, VT 05405 -0160			8. PERFORMING ORGANIZATION REPORT NUMBER		
9. SPONSORING/MONITORING AGENCY NAME(S) AND ADDRESS (ES) U.S. Army Research Office P.O. Box 12211 Research Triangle Park, NC 27709-2211			10. SPONSOR/MONITOR'S ACRONYM(S) ARO		
			11. SPONSOR/MONITOR'S REPORT NUMBER(S) 63445-EL-RIP.2		
12. DISTRIBUTION AVAILABILITY STATEMENT Approved for public release; distribution is unlimited.					
13. SUPPLEMENTARY NOTES The views, opinions and/or findings contained in this report are those of the author(s) and should not be construed as an official Department of the Army position, policy or decision, unless so designated by other documentation.					
14. ABSTRACT Every second, millions of Americans depend on a vast U.S. infrastructure that extends from coast to coast and is exceeding its design life. The health and state of the concrete roadways and bridge decks that commuters rely on a daily basis can be efficiently examined and monitored with the use of ground penetrating radar (GPR). Repair and maintenance of these concrete structures is slow and expensive. The development and implementation of a faster and more reliable, near to mid field, air-coupled phased-array GPR system would help to solve these two problems. The objective of the study was to see how accurately the phased array system can detect subsurface objects and					
15. SUBJECT TERMS ground penetrating radar, phased array, near-field detection, air-coupled					
16. SECURITY CLASSIFICATION OF:			17. LIMITATION OF ABSTRACT	15. NUMBER OF PAGES	19a. NAME OF RESPONSIBLE PERSON
a. REPORT UU	b. ABSTRACT UU	c. THIS PAGE UU			Dryver Huston
					19b. TELEPHONE NUMBER 802-656-1922

Report Title

PERFORMANCE EVALUATION OF AN AIR-COUPLED PHASED-ARRAY RADAR FOR NEAR-FIELD DETECTION OF STEEL

ABSTRACT

Every second, millions of Americans depend on a vast U.S. infrastructure that extends from coast to coast and is exceeding its design life. The health and state of the concrete roadways and bridge decks that commuters rely on a daily basis can be efficiently examined and monitored with the use of ground penetrating radar (GPR). Repair and maintenance of these concrete structures is slow and expensive. The development and implementation of a faster and more reliable, near to mid field, air-coupled phased-array GPR system would help to solve these two problems. The objective of the study was to see how accurately the phased-array system can detect subsurface objects and corrosion. A concrete slab with an embedded object was used to simulate a concrete bridge deck or roadway. The concrete slab was placed under the phased-array radar system which emitted electromagnetic energy into the slab and the reflected signal was analyzed to see if the system can detect subsurface objects like rebar which can often be found in concrete structures. The results show that varying the frequency, height and orientation of the source antennas increases or decreases the magnitude of the return signal. This study outlines which configuration of parameters best optimizes the phased-array system's ability to detect subsurface objects. The reflected signals gathered from the experiments were also compared to a theoretical model of the phased-array's reflected signal providing valuable information on the systems performance and provide concepts for improved designs. A commercial phased-array GPR trailer could be built in the near future that could scan and detect delaminations, cracks, voids and corrosion of concrete roadways and bridge decks with faster data collection capabilities due to the phased-arrays electronic sweeping feature.

PERFORMANCE EVALUATION OF AN AIR-COUPLED PHASED-ARRAY
RADAR FOR NEAR-FIELD DETECTION OF STEEL

A Thesis Presented

by

Jonathan Razinger

to

The Faculty of the Graduate College

of

The University of Vermont

In Partial Fulfillment of the Requirements
for the Degree of Master of Science
Specializing in Mechanical Engineering

May, 2014

Accepted by the Faculty of the Graduate College, The University of Vermont, in partial fulfillment of the requirements for the degree of Master of Science specializing in Mechanical Engineering.

Thesis Examination Committee:

Dryver Huston, Ph.D. Advisor

Junru Wu, Ph.D.

Tian Xia, Ph.D. Chairperson

Cynthia J. Forehand, Ph.D. Dean, Graduate College

Date: March 28, 2014

ABSTRACT

Every second, millions of Americans depend on a vast U.S. infrastructure that extends from coast to coast and is exceeding its design life. The health and state of the concrete roadways and bridge decks that commuters rely on a daily basis can be efficiently examined and monitored with the use of ground penetrating radar (GPR). Repair and maintenance of these concrete structures is slow and expensive. The development and implementation of a faster and more reliable, near to mid field, air-coupled phased-array GPR system would help to solve these two problems. The objective of the study was to see how accurately the phased-array system can detect subsurface objects and corrosion. A concrete slab with an embedded object was used to simulate a concrete bridge deck or roadway. The concrete slab was placed under the phased-array radar system which emitted electromagnetic energy into the slab and the reflected signal was analyzed to see if the system can detect subsurface objects like rebar which can often be found in concrete structures. The results show that varying the frequency, height and orientation of the source antennas increases or decreases the magnitude of the return signal. This study outlines which configuration of parameters best optimizes the phased-array system's ability to detect subsurface objects. The reflected signals gathered from the experiments were also compared to a theoretical model of the phased-array's reflected signal providing valuable information on the systems performance and provide concepts for improved designs. A commercial phased-array GPR trailer could be built in the near future that could scan and detect delaminations, cracks, voids and corrosion of concrete roadways and bridge decks with faster data collection capabilities due to the phased-arrays electronic sweeping feature.

ACKNOWLEDGEMENTS

I would like to take this moment to give a special thanks to my advisor Dryver Huston Ph.D. for guiding me through this academic challenge and giving me the opportunity to further my studies at the University of Vermont. I would also like to thank the other members of my committee, Tian Xia Ph.D. and Junru Wu Ph.D., for the helpful suggestions they made throughout the thesis process. Lastly, I would also like to thank the UVM colleagues that shared their knowledge, and helped me conduct some crucial tests. This includes Dylan Burns Ph.D., Anbu Vankatachalam, Zhang Yu and Amr Ahmed. The experiences and the knowledge gained during my time at the University of Vermont will surely guide me toward future success.

This work was supported in part by the U.S. Department of Transportation USDOT DTOS5908G00102 and the NIST TIP Program 70NANB9H9012.

TABLE OF CONTENTS

	Page
ACKNOWLEDGEMENTS	ii
LIST OF TABLES	vii
LIST OF FIGURES	viii
LIST OF EQUATIONS	xvi
CHAPTER 1: INTRODUCTION	1
CHAPTER 2: BACKGROUND	4
2.1. Concrete/Pavement Properties	4
2.2. Concrete/Pavement Damage	4
2.3. Steel Corrosion Process	5
2.4. Ground Penetrating Radar	9
2.4.1. Electromagnetic Wave Propagation	10
2.4.2. Electromagnetic Radiation Scattering Effects	15
2.4.3. Field Regions	20
2.4.4. Antenna Radiation Pattern	22
2.5. Phased-Array Radar	25
2.5.1. Antenna Array Mechanics	26
2.5.2. Theoretical Reflected Signal from a Two-Element Array	27

2.5.3. Mutual Coupling in Antenna Arrays	28
2.5.4. Antenna Array Design Considerations	29
CHAPTER 3: METHODS	31
3.1. Phased-Array System Setup	31
3.1.1. Components used in Phased-Array Radar System	31
3.1.2. Phased-Array Antenna Setup.....	33
3.2. Network Analyzer Software Setup	34
3.3. Laboratory Experiments	35
3.3.1. Different Concrete Slab Configurations	36
3.3.2. Position Increment Step Size	38
3.3.3. Varying Source Frequencies	40
3.3.4. Varying Antenna Height.....	41
3.3.5. Changing Antenna Orientations	42
CHAPTER 4: RESULTS AND DISCUSSION.....	45
4.1. Varying Concrete Slab Configurations.....	45
4.2. Varying Increment Size	49
4.2.1. Comparison between Different Increment Sizes	49
4.2.2. Comparison with Theoretical Reflective Model.....	53
4.3. Varying Antenna Height.....	55
4.4. Varying Source Frequency	59
4.5. Varying Antenna Orientation	65
4.6. Antenna Coupling.....	69

CONCLUSION.....	79
REFERENCES	85
APPENDIX A: TABLE OF EXPERIMENTS	87
APPENDIX B: TABLE OF PORT POWERS.....	90
APPENDIX C: INSTRUCTIONS FOR NETWORK ANALYZER SOFTWARE SETUP	91
Appendix.C.1: Cable Calibration	91
Appendix.C.2: Assigning Antenna Power.....	93
Appendix.C.3: Phase Sweep Function.....	95
Appendix.C.4: S41 and S43 Network Analyzer Software Setup	100
APPENDIX D: PHASED-ARRAY PLOTS FROM MULTIPLE TESTS AT DIFFERENT PHASE OFFSETS.....	104
APPENDIX E: A.H. SYSTEMS DOUBLE RIDEGE HORN ANTENNA SPECIFICATIONS.....	113
APPENDIX F: HOME-MADE GIMA ANTENNA SPECIFICATIONS.....	117
APPENDIX G: MATLAB CODES USED TO ANALYZE DATA FROM EXPERIMENTS	121
Appendix.G.1: Code for tests 10-13	121
Appendix.G.2: Code for tests 3-5a, 13-15, 20-29, 30, 32.....	124
Appendix.G.3: Function file used for all tests	129
Appendix.G.4: Code for comparing slab configurations.....	130
Appendix.G.5: Code for comparing increment size	131

Appendix.G.6: Code for comparing antenna height	132
Appendix.G.7: Code for comparing source frequencies.....	134
Appendix.G.8: Code for comparing antenna orientations	137
Appendix.G.9: Code for measuring the amount of antenna coupling	140
Appendix.G.10: Code for determining mutual coupling between antennas.....	141
Appendix.G.11: Code for comparing experimental S41 reflected signal to theoretical model of an S41 reflected signal with coupling	143

LIST OF TABLES

Table	Page
Table 1: Electromagnetic Scattering Classification [14]	16
Table 2: List of Components in Figure 4	32
Table 3: List Tests.....	87
Table 4: List of Port Power for Each Test	90

LIST OF FIGURES

Figure	Page
Figure 1: Steel corrosion process [1]	8
Figure 2: Pitting process [2].....	9
Figure 3: Image of subsurface object using GPR creating a B-Scan [1]	10
Figure 4: Electromagnetic wave propagation, an A-Scan and relative dielectric constants for multiple materials [1].	14
Figure 5: Uniform plain wave scattering off a rectangular plate [14].	20
Figure 6: Uniform plain wave scattering off a circular cylinder [14].....	20
Figure 7: Antenna field regions [16].....	22
Figure 8: Coordinate system for antenna radiation pattern [16]	23
Figure 9: Principal E-Plane and H-Plane patterns [16].....	24
Figure 10: Diagram of radiation lobes [16].	25
Figure 11: Phased-array setup geometry modeled after a two-element array	27
Figure 12: Components used for phased-array system	31
Figure 13: Phased-array system laboratory setup	36

Figure 14: Concrete slab configurations	37
Figure 15: Position setting rig with 3” (7.62cm) increment size	39
Figure 16: Position setting rig with ½” (1.27cm) increment size	40
Figure 17: Position setting rig with ¼” (.635cm) increment size	40
Figure 18: Antenna Configuration #1	43
Figure 19: Antenna Configuration #2	43
Figure 20: Antenna Configuration #3	44
Figure 21: Maximum amplitude reflected signals when the slab configurations were varied. For all slab configurations this occurred at a phase offset of 180 degrees. The vertical black lines represent the locations of the antennas. Two different position rigs where used and location 1 shows the 3” (7.62cm) shift between the two.	45
Figure 22: Maximum amplitude reflected signals when the increment size was varied. For 0.25” (0.635cm) increment size the phase offset was at 315 degrees and for .5” (1.27cm) increment size the phase offset was at 135 degrees. The vertical black line represents the location of the receiving antenna and the black and green dashed lines represent the approximate signal envelopes.	49
Figure 23: Theoretical reflective signal compared to the reflected signals acquired during Test 10 at an increment size of .5” (1.27cm).	53
Figure 24: Maximum amplitude reflected signals when the antenna height was varied. At 19.5” (49.53 cm) the phase offset was at 315 degrees and at 26” (66.04cm) the phase	

offset was at 225 degrees. Vertical black lines represent the locations of the antennas and the black dashed line represents the approximate signal envelope. 55

Figure 25: Reflected signals at 315 degree phase offset when the antenna height was varied. Vertical black lines represent the locations of the antennas. 55

Figure 26: Reflected signals at 225 degree phase offset when the antenna height was varied. Vertical black lines represent the locations of the antennas. 56

Figure 27: Maximum amplitudes of the reflected signals when the source frequency was varied. At 4GHz the phase offset was at 225 degrees and at 6GHz the phase offset was at 180 degrees. Vertical black lines represent the locations of the antennas and the black dashed oval shows an area of increased resolution. Locations 1 and 2 are shifts between the signals near the receiving antenna. 59

Figure 28: Reflected signals at 180 degree phase offset when the source frequency was varied. Vertical black lines represent the locations of the antennas and the black dashed oval shows an area of increased resolution. Locations 1, 2 and 3 are peak-to-peak distances of the reflected signal at 6GHz..... 59

Figure 29: Phase angles of reflected signals at 180 degrees phase offset when the source frequencies were varied. Vertical black lines represent the locations of the antennas. . 60

Figure 30: Reflected signals at 180 degree phase offset, at a 6GHz source frequency, when source antenna #2 was changed. Vertical black lines represent the locations of the antennas and the black dashed oval shows an area of increased resolution. The green dashed line represents the approximate envelope of the reflected signal with a new source antenna #2..... 62

Figure 31: Maximum amplitude reflected signals, when the antenna orientations were varied. For configuration #1 the phase offset was 315 degrees, for configuration #2 the phase offset was 180 degrees and for configuration #3 the phase offset was 225 degrees. Vertical black lines represent the locations of the antennas and the black dashed line shows the approximate shape of the reflected signal envelope for configuration #2.	65
Figure 32: Maximum amplitude reflected signals of configuration #1 and configuration #3. For configuration #1 the phase offset was 315 degrees and for configuration #3 the phase offset was 225 degrees. The center vertical black line represents the location of the receiving antenna. Location 1 shows a shift of .0903m between the two tests. The blue dashed line shows the approximate shape of the reflected signal envelope for configuration #2 and the green dashed line shows the approximate shape of the reflected signal envelope for configuration #1.	65
Figure 33: Diagram of multiple signals that the receiving antenna might see.....	70
Figure 34: Comparisons of S41 and S43 tests	71
Figure 35: Comparisons of an S43 test to identify the extent of mutual coupling between the source and receiving antennas throughout a range of frequencies. Solid blue line represents the signal due to mutual coupling, the solid red line represents a signal with mutual coupling and a reflected signal from an object 7ft (2.14m) away and the solid black line represents a signal with mutual coupling and a reflected signal from an object 4ft (1.22m) away.	75
Figure 36: Comparison of an experimental S41 test (solid black line) with a theoretical mathematical model representing an S41 test with coupling (solid blue line). The solid red line represents the tapering of the experimental data as the reflective object moves beyond the radiation pattern of the antennas.	76

Figure C.1: Calibrating cables with electronic calibration module. (a) Finding the Cal Wizard and (b) choosing the ECal option.....	91
Figure C.2: Making sure calibrated cables are under the right channel.....	93
Figure C.3: Assigning power to network analyzer ports	94
Figure C.4: (a) Creating new trace and (b) activating receivers	96
Figure C.5: (a) Selecting the correct sweep type and (b) applying the correct phase sweep parameters	97
Figure C.6: Making sure all phase sweep parameter are correct. (a) Opening the phase control window. (b) The phase control window.	98
Figure C.7: Checking the phase control parameters	99
Figure C.8: (a) Running phase sweep function. (b) Saving the data.	100
Figure C.9: (a) Creating new trace. (b) Selecting the correct S-Parameters.....	102
Figure C.10: (a) Selecting the correct sweep type. (b) Applying the correct frequency sweep parameters.	103
Figure D.1: Test 3 Plotting Phase Offsets Every 45 Degrees	104
Figure D.2: Test 4a Plotting Phase Offsets Every 45 Degrees	104
Figure D.3: Test 5a Plotting Phase Offsets Every 45 Degrees	105
Figure D.4: Test 10 Plotting Phase Offsets Every 45 Degrees	105

Figure D.5: Test 12 Plotting Phase Offsets Every 45 Degrees	106
Figure D.6: Test 13 Plotting Phase Offsets Every 45 Degrees	106
Figure D.7: Test 14 Plotting Phase Offsets Every 45 Degrees	107
Figure D.8: Test 15 Plotting Phase Offsets Every 45 Degrees (Retest of Test 13)	107
Figure D.9: Test 20 Plotting Phase Offsets Every 45 Degrees	108
Figure D.10: Test 21 Plotting Phase Offsets Every 45 Degrees	108
Figure D.11: Test 22 Plotting Phase Offsets Every 45 Degrees	109
Figure D.12: Test 23 Plotting Phase Offsets Every 45 Degrees	109
Figure D.13: Test 25 Plotting Phase Offsets Every 45 Degrees	110
Figure D.14: Test 27 Plotting Phase Offsets Every 45 Degrees	110
Figure D.15: Test 28 Plotting Phase Offsets Every 45 Degrees	111
Figure D.16: Test 30 Plotting Phase Offsets Every 45 Degrees	111
Figure D.17: Test 32 Plotting Phase Offsets Every 45 Degrees	112
Figure E.1: A.H. Systems double ridge horn antenna radiation pattern [24].....	116
Figure F.1: GIMA antenna design with critical dimensions [28]	117

Figure F.2: SWR results for the GIMA antenna. Close to ideal impedance throughout the frequency range [28].	118
Figure F.3: Return loss results for the GIMA antenna. Average return loss of -20dB with an accepted power of approximately 99.2%. The antenna is frequency independent and has a high radiation efficiency [28].....	118
Figure F.4: Simulated radiation pattern of the home-made GIMA antenna using HFSS [28].....	119
Figure F.5: Solidworks model of the GIMA antenna used to simulate the antenna radiation pattern [26].....	119
Figure F.6: Simulated radiation pattern of the home-made GIMA antenna at a frequency of 2.8 using HFSS [26].	120

LIST OF EQUATIONS

Equation	Page
2.1: Anodic Chemical Reaction	3
2.2: Cathodic Chemical Reaction	3
2.3: Formation of Ferric Hydroxide	4
2.4: Formation of Ferrous Hydroxide	4
2.5: Formation of Hydrated Ferrous Hydroxide	5
2.6-2.9: Maxwell's Equations	8
2.10: Complex Permittivity	9
2.11: Relative Permittivity	9
2.12: Complex Relative Permittivity	9
2.13: Speed of an Electromagnetic Wave	10
2.14: Penetration Depth of an Electromagnetic Wave	10
2.15: Reflection Coefficient	10
2.16: Electric Field	14
2.17: Magnetic Field	14
2.18: 2D Radar Cross Section	15
2.19: 3D Radar Cross Section	15
2.20: Incident Electric Field	16
2.21: Incident Magnetic Field	16

2.22: Reactive Near-Field Boundary	18
2.23: Radiating Near-Field Boundary	18
2.24: Far-Field Boundary	18
2.25: Far-Field Electromagnetic Field Approximation	24
2.26: Generalized Two Element Array Electromagnetic Field	25
2.27: Electromagnetic Field of Source Antennas	25
2.28: Phase Angles for Time Phase Lag	25
2.29: Source Signal Direction	26
2.30: Reflected Electromagnetic Field	26
2.31: Theoretical Far-Field Two Element Array Reflected Electromagnetic Field	26
3.1: Reliability of a System in Series	33
3.2: Reliability of a System in Parallel	34
4.1: Wavelength	50
4.2: Reflected Electromagnetic Field with Mutual Coupling Terms	76
5.1: Probability Density Function When an Object is Not Present	82
5.2: Probability Density Function When an Object is Present	82
5.3: Probability of Detection	82

CHAPTER 1: INTRODUCTION

Every second, millions of Americans depend on a vast U.S. infrastructure that extends from coast to coast and is exceeding its design life. In Vermont alone, bridges that are greater than 20ft long, 32 percent were classified as being deficient. Out of the 32 percent, 20 percent were structurally deficient (SD) and 12 percent were functionally obsolete (FO). When a bridge is classified as (SD) it has significant deterioration on the deck, supports and other crucial components. A bridge that is (FO) usually is in less than suitable conditions and does not adhere to current design standards. Bridges under either classification are safe for continued use, but need to be closely monitored [6].

The health and state of the concrete roadways and bridge decks that commuters rely on a daily basis can be efficiently examined and monitored with the use of ground penetrating radar (GPR). Repair and maintenance of these concrete structures is slow and expensive. There has been a steady increase in bridge maintenance funding in the last seven years in Vermont. In 2006 bridge maintenance funding was at \$4.7 million and in 2013 it reached \$36.8 million. The increase in funding over the years can also be seen for other areas of Vermont's deteriorating infrastructure. Routine maintenance will extend the service life of a concrete structure. To properly assess the condition of a structure takes an extended period of time and is a labor intensive process. In most cases, traffic lanes must be closed, restricting the flow of traffic and creating an inconvenience to the commuter [7]. The development and implementation of a faster and more reliable, near-field, air-coupled phased-array GPR system could make bridge deck and roadway maintenance more efficient and cost effective.

This study outlines the theory and methodology required for determining the performance, accuracy and reliability of a near-field air-coupled phased-array radar system. Phased-array radar has been extensively studied, researched and implemented for far-field applications. Its implementation in naval warships is the most commonly known use of phased-array radar, but has also been applied to aircraft. The interactions of electromagnetic energy emitted by a phased-array in the far-field is well documented and the system is proven to be very reliable. Moving into the near-field, scattering effects from a reflected object change and the electromagnetic field interactions add another level of complexity that is not fully understood. As we look for new and more efficient ways to monitor and maintain concrete structures, there is no reason why this technology that has been proven in the far-field cannot be repurposed for use in the near-field.

To be able to predict the interactions of electromagnetic radiation of a phased-array radar system, we must first understand how electromagnetic waves propagate through certain materials. The propagation of electromagnetic waves through a media to detect subsurface objects, also known as ground penetrating radar (GPR), has only been in use for around one hundred years. It was not until 1929 that the first GPR survey was conducted by W. Stern to measure the depth of a glacier in Austria. After WWII, the interest for GPR grew and more efficient GPR systems were developed for military applications. GPR only became affordable to civilians in 1985 and reference books on GPR did not become available until the 1990's [8]. For civilian purposes GPR is a relatively new technology, which can be improved and with the state of the U.S. infrastructure there is a market for an improved radar system. The theory and mechanisms behind GPR rely mainly on the theory of electromagnetic wave propagation through dielectric media. For GPR purposes, the

media may consist of concrete, pavement or earth. When GPR is deployed to monitor and maintain roadways and bridge decks, electromagnetic radiation propagates through either concrete or pavement to detect delaminations, cracks, voids or a subsurface object.

CHAPTER 2: BACKGROUND

2.1. Concrete/Pavement Properties

Concrete is a mixture comprised of two components, aggregates and paste. The paste Portland cement and water adheres to the aggregate, sand and gravel or crushed stone, and forms a mass that hardens as a result of the chemical reaction between the cement and water. The material properties of concrete can be altered by changing the concentrations of the ingredients. In general, concrete has a high compressive strength and low tensile strength which is why reinforcing materials are added to the concrete to make it stronger in tension. For concrete structures, steel is most commonly used as the reinforcing material. The degradation of concrete can vary depending on the environment. Concrete as it cures normally shrinks over time and its weakness in tension, makes concrete susceptible to cracking. The cracks usually develop in the matrix (or paste) of the concrete, since most of the strength of the concrete is from the aggregates [1, 2].

2.2. Concrete/Pavement Damage

Environmental conditions are significant factors affecting how concrete degrades over time. Concrete can be damaged in many ways. Cracks or delaminations can occur from: embedded water freezing, further shrinkage due to fire or radiant heat, aggregate expansion, bacterial corrosion, leaching, sea water effects, erosion from flowing water, physical and chemical damage from intrusive agents, and from the expansion of corroding reinforcing steel bars. Degradation of the concrete and corrosion of the steel reinforcing bars from chemical damage can be attributed to carbonation, chlorides, sulfates and distillate water [1, 2].

2.3. Steel Corrosion Process

Metals tend to corrode in acids. The concrete mixture is made up of a Portland cement solution which is a strong alkaline that preserves and protects metals. It is alkaline because pores within the concrete contain high concentrations of soluble calcium, sodium and potassium oxides. These oxides form very alkaline hydroxides with a pH around 12 or 13 when water is present, which forms a passive protective layer around metals. To increase the structural integrity of a concrete structure, steel is the metal of choice for reinforcement. The passivating layer is a thin, dense oxide film that when maintained properly can prevent further corrosion and can be far better than any artificial coating. The passivating layer may be eroded away if the pH of the alkaline concrete decreases or if the integrity of the covering concrete is decreased in any way that might increase the passage of corrosive agents to the steel [1, 2].

Carbonation and chloride attack both break down the protective passive layer around steel. For carbonation to occur, sulfur dioxide and carbon dioxide from the surrounding environment react with hydrated cement and a chemical reaction begins. As sulfur dioxide reacts with the hydrated cement, the surface of the concrete starts to dissolve because it does not diffuse into concrete as quickly. Carbon dioxide begins to diffuse into the concrete and reacts with the hydrated cement to produce calcium carbonate. The presence of sulfur dioxide and carbon dioxide in the concrete does not influence the material properties or the strength of the concrete, but it decreases the overall integrity of a concrete structure that incorporates reinforced steel. The reaction above removes

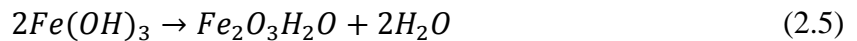
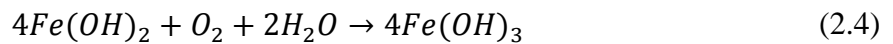
hydroxyl ions ($2OH^-$) from the concrete pores and reduces the pH below 9 or 10 making the steel more prone to corrosion if the sufficient concentrations of water and oxygen are present. A well compacted, dense concrete with a good cover will be more resistant to carbonation than a porous concrete. The greatest rate of carbonation occurs when the relative humidity is between 60% and 75%. [1].

For chloride attack to occur, pores within concrete must have the proper amount of oxygen and free chloride ions present, which then causes a localized breakdown of the protective passive layer around steel. Hydroxyl ions, which are a product of a cathodic reaction, repair the passive layer which decreases the rate of corrosion from chloride. Once the chloride ions to hydroxyl ions ratio exceeds a critical limit, the breakdown of the passive layer cannot be stopped and pitting occurs on the surface of the steel.

Once the protective passivating layer around steel breaks down, rust and other corrosion byproducts begin appearing on the surface. The chemical reactions that then continue to corrode the steel are the same whether the deterioration of the passivating layer is due to chloride attack or carbonation. The two main chemical reactions that govern the corrosion of steel are the anodic and cathodic reactions, which are described in Equations (2.1) and (2.2) and depicted in (Figure 1). [1, 2].



As the steel corrodes, iron dissolves in water or moisture within the pores of the concrete and gives up electrons. To preserve electrical neutrality, the free electrons are consumed by the cathodic reaction. The cathodic reaction produces hydroxyl ions, which like mentioned above regenerate the passive layer. The iron cation (Fe^{2+}) then bonds to hydroxide (OH^-), which might have been a byproduct of another reaction or made its way in through a crack and forms the first type of rust ferrous hydroxide ($Fe(OH)_2$). By continuing to bond to oxygen and water, different types of rust begin to form around the steel bar. The rust can also become ferric hydroxide ($4Fe(OH)_3$) and hydrated ferric hydroxide ($Fe_2O_3H_2O + 2H_2O$). Hydrated ferric hydroxide is the type of rust that has the greatest volume increase and is the one that most likely contributes to cracking and spalling (fragments) of concrete with a volume increase 2 to 10 times that of steel. The volume increase puts the concrete in tension, causing cracks to appear. The amount of corrosion build-up needed to surpass the tensile strength of concrete and create a crack is dependent on the type of concrete and the concentrations of the ingredients. The presence of cracks then increases the rate of corrosion by giving corrosive agents a greater pathway to reach the embedded steel. The chemical reactions for all three forms of rust are described in Equations (2.3-2.5) and shown in (Figure 1) [2].



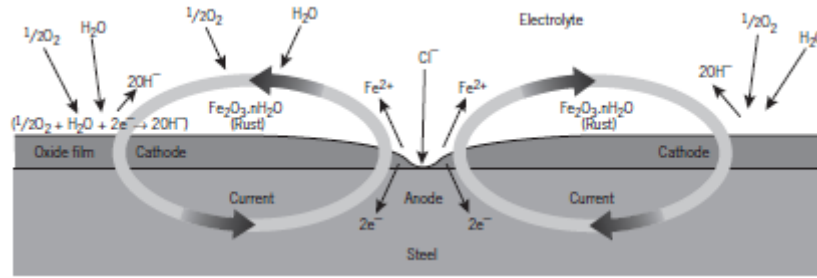


Figure 1: Steel corrosion process [1]

As the number of pits increases and the affected area expands, generalized corrosion can be seen. This appears in (Figure 2). Pitting of the steel bar can occur where there is an impurity or imperfection in the concrete or at an inclusion of the steel bar. At these locations, the protective passive layer is vulnerable and an electrochemical potential is created that attracts chloride ions. The pH in this region decreases and an acid is formed, which dissolves iron and that iron then reacts with water creating rust. This is again shown in Equation (2.3). The rust forms over the pit and concentrates (H^+) acid and prevents the formation of the protective passive layer, which accelerates the rate of corrosion. Corrosion in imbedded steel can also be induced by stray currents. The current jumps from one conductor (in this case a steel bar) to another, through an ionic medium, the concrete. The concrete becomes the cathode and the steel bar becomes the anode and all the chemical reaction equations mentioned above again hold valid [2].

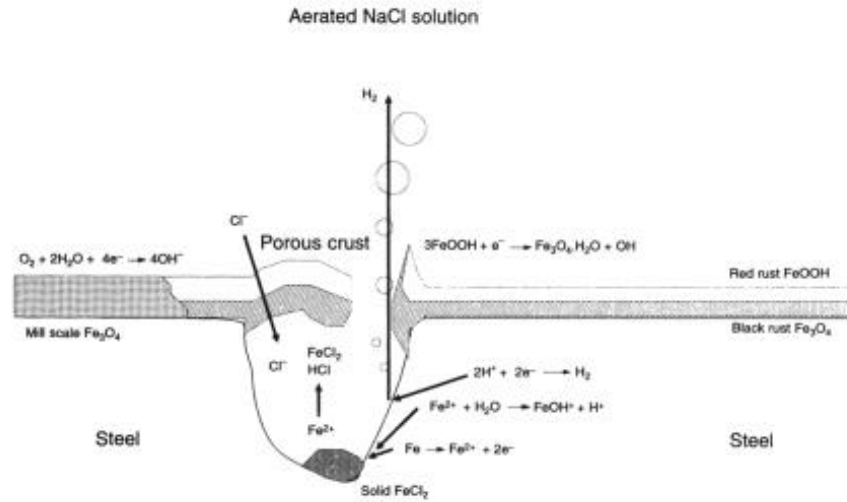


Figure 2: Pitting process [2]

2.4. Ground Penetrating Radar

There are many different techniques that have been developed by the American Concrete Institute (ACI) and the International Concrete Repair Institute (ICRI) to repair damaged and corroded concrete structures, but the structural integrity of concrete structures that are heavily damaged can never be fully recovered. As the extent of damage and corrosion within a concrete structure increases the amount of capital and labor needed to repair the structure also increases. Regular maintenance and early detection of damage and corrosion within concrete structures would save money and extend the life of the structure. Monitoring of roadways and bridge decks, which have concrete has been done for years by the government and by private contractors. Concrete structures can be monitored using destructive and non-destructive methods. Destructive methods may include: taking core and dust samples and the use of the half-cell method. While non-destructive methods

include: impact echo, infrared thermography, acoustic emission, radiography, (GPR) and others.

Non-destructive methods rarely yield direct information on the strength of a concrete structure, but they give important information about the structure without sacrificing structural integrity. To detect subsurface objects, changes in material properties, voids and cracks GPR is often used. GPR sends out electromagnetic radiation into the area of interest, which is usually the ground. An object with a dielectric constant that differs from the surrounding medium, reflects and/or scatters the wave. The receiving antenna on the GPR detects the variation in the return signal. A 2D image is created, where the different reflections appear as the boundaries of objects with different dielectric constants. (Figure 3) shows what a 2D image, a B-scan, looks like with three steel rods embedded at different heights within a concrete slab. The boundaries of the rods are seen as hyperbolas.

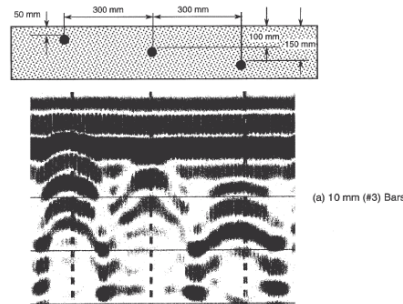


Figure 3: Image of subsurface object using GPR creating a B-Scan [1]

2.4.1. Electromagnetic Wave Propagation

Many theories have been developed to better understand how electromagnetic waves interact with physical media. The research and theories explaining this wave interaction is a fundamental part of understanding how GPR and any other type of radar

system works. The interactions between electromagnetic radiation and physical media are very complex and can be explained with the use of quantum mechanics. Simplifications can be made to these complex theories to make these problems easier to compute. The most common is to use Maxwell's equations, presented as Equations (2.6)-(2.9). These equations express electromagnetic radiation as electric and magnetic field vectors. The electromagnetic waves can be depicted as scalars, but this comes with the loss of directional information. The representation of electromagnetic waves can be further simplified if they are considered to be plane waves. If this approximation is assumed, then a geometric ray tracing model can be used. Because we are only starting to understand near-field phased-array wave interactions, we simplified our theoretical wave reflection model so that we were able to use the geometric ray tracing model [9, 11].

$$\nabla \times E = -M_i - \frac{\partial B}{\partial t} \quad (2.6)$$

$$\nabla \times H = J_i + J_c + \frac{\partial D}{\partial t} \quad (2.7)$$

$$\nabla \cdot D = q_{ev} \quad (2.8)$$

$$\nabla \cdot B = q_{mv} \quad (2.9)$$

Where:

- E = electric field intensity (volts/meter)
- H = magnetic field intensity (amperes/meter)
- D = electric flux density (coulombs/square meter)
- B = magnetic flux density (webers/square meter)
- J_i = impressed (source) electric current density (amperes/square meter)
- J_c = conduction electric current density (amperes/square meter)
- M_i = impressed (source) magnetic current density (volts/square meter)
- q_{ev} = electric charge density (coulombs/cubic meter)
- q_{mv} = magnetic charge density (webers/cubic meter)

The main properties that interfere with the transmitted and reflected electromagnetic energy are the dielectric permittivity and the conductivity of the material. Dielectric permittivity is the amount of electrostatic energy stored per unit volume for a unit potential gradient, while electrical conductivity measures the ease of electrical current through a material. In GPR applications, the emitted electromagnetic waves propagate through low-loss dielectrics such as concrete and many soils. An exception is the metals which are used to increase structural integrity. In concrete the dielectric permittivity is expressed as a complex quantity with real and imaginary terms, which can be seen in Equation (2.10). The real term is known as the dielectric constant (ϵ') while the imaginary term is known as the loss factor (ϵ''). The dielectric constant can be normalized by dividing it by the permittivity of free space ($\epsilon_0 = 8.85 \times 10^{-12}$ farad/m). This ratio is referred to as the relative dielectric permittivity (ϵ_r), shown in Equation (2.11) and the complex relative permittivity is shown in Equation (2.12) [1, 10].

$$\epsilon = \epsilon' + i\epsilon'' \quad (2.10)$$

$$\epsilon_r = \frac{\epsilon}{\epsilon_0} \quad (2.11)$$

$$\epsilon_r = \epsilon'_r + i\epsilon''_r \quad (2.12)$$

The speed of the electromagnetic wave (c) and the depth of the reflective surface (D) can be determined by using Equations (2.13) and (2.14). Where c_o is the speed of light in air. The reflected energy at the interface between two different materials with low-loss

dielectrics can be found by using Equation (2.15). This equation gives the ratio of reflected to incident amplitude of the electromagnetic field, also known as the reflection coefficient ($\rho_{1,2}$). Where 1 and 2 represent two different materials.

$$c = \frac{c_o}{\sqrt{\epsilon_r}} \quad (2.13)$$

$$D = \frac{ct}{2} \quad (2.14)$$

$$\rho_{1,2} = \frac{\sqrt{\epsilon_{r1}} - \sqrt{\epsilon_{r2}}}{\sqrt{\epsilon_{r1}} + \sqrt{\epsilon_{r2}}} \quad (2.15)$$

These equations are the foundation that govern how GPR works. The relative permittivity of a material will dictate the speed and the amplitude of the electromagnetic wave. The time and amplitude that it takes for a reflected signal to reach the receiving antenna on the GPR system will give the user valuable data of what might be lying beneath the surface. The GPR system turns the instantaneous data into an A-Scan. Then multiple A-Scans can be stacked together to create a B-Scan, which depicts the response of the reflected signals over a traveled distance. A diagram of electromagnetic wave propagation emitted by GPR and an A-Scan can be seen in (Figure 4) [1].

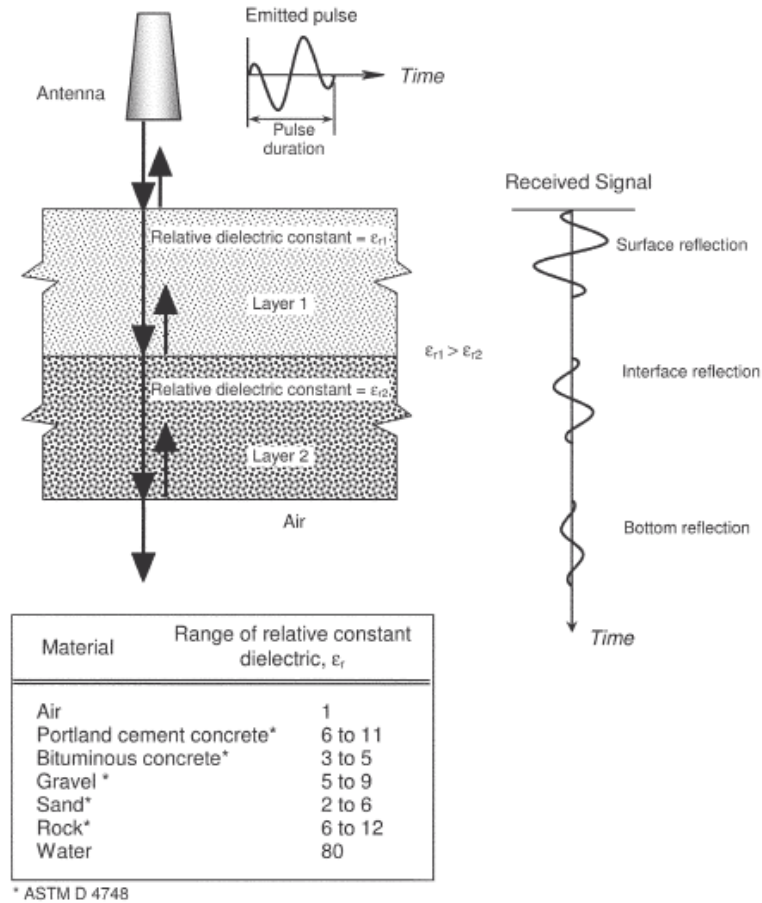


Figure 4: Electromagnetic wave propagation, an A-Scan and relative dielectric constants for multiple materials [1].

Like all devices, GPR has its limitations and disadvantages. The depth that GPR can monitor depends on many factors including: electrical conductivity of the ground, the source signal frequency and source signal power. When the ground conductivity increases (due to an increased concentration of water) the GPR penetration depth decreases. This occurs because the electromagnetic energy emitted from the source antenna is dissipated into heat at a faster rate when the ground is more conductive. As the source signal frequency increases, the resolution increases but, the energy is more easily dissipated and

the penetration depth decreases. Scattering effects also influence the resolution of the GPR image. Improvements in GPR hardware and software can increase resolution and performance. An increased understanding of linear and non-linear scattering effects would make it possible to detect smaller, subsurface phenomena and effects like corrosion, which is believed to behave non-linearly.

2.4.2. Electromagnetic Radiation Scattering Effects

Simplifying the models of electromagnetic wave propagation will make it easier to understand the general phenomena occurring when the waves reflect off of a specific medium. These simplified models provide results of reflected signals in ideal circumstances. Even in a laboratory setting, where it might be possible to control most or certain parameters, it is still unlikely that the results will be exactly like the ideal model.

During the testing of the phased-array system there were certain parameters that we were unable to control. This included noise from the surroundings and the consistency of concrete properties. To enhance the signals from the subsurface objects the noise and concretes reflected signals were subtracted out, essentially leaving only the reflected signal from the subsurface object. When comparing experimental results with the ideal reflected signal there were still major differences between the two. It is possible that these differences can be attributed to scattering effects.

When electromagnetic radiation deviates from a straight trajectory, the radiation undergoes scattering. In our test setup, electromagnetic radiation could be scattered by a number of things. This may include roughness between two different materials, air bubbles within the concrete or other unwanted materials within the concrete. The particle size of

what the electromagnetic radiation is reflected off of and the wavelength (λ) of the signal also dictates the type of scattering that is occurring.

For electromagnetic scattering there are three major types of scattering, Rayleigh, Mie and Geometric (optical) scattering. Rayleigh scattering occurs when electromagnetic radiation is scattered by a small particle relative to the wavelength of the emitted signal. Geometric (optical) scattering occurs when the particle is much larger than the wavelength of the emitted signal, Mie scattering occurs when the particle is approximately the same size as the emitted wavelength. The particle size restrictions that categorize the type of scattering that will occur can be seen in (Table 1), where r is the approximate radius of the particle [14].

Table 1: Electromagnetic Scattering Classification [14]

Type of Electromagnetic Scattering	Classification Limit
Rayleigh	$(r < .1\lambda)$
Mie	$(.1\lambda < r < 2\lambda)$
Geometric (Optical)	$(r > 2\lambda)$

For these models of electromagnetic radiation the particle is assumed to be spherical. Scattering from a spherical object can then be used as a reference because of its symmetry, which can then be compared to scattering from objects with complex shapes. In our tests that object was usually a conductive steel rod, which in 2D has the same geometry as a sphere. These simplifications do not greatly affect the classification limit that a particle is placed under [14].

When scattering is introduced into the electric and magnetic field equations we arrive at Equations (2.16) and (2.17), which represent the total electric field (E^t) and magnetic field (H^t) as the addition of the scattered electric (E^s) and magnetic (H^s) fields with the incident electric (E^i) and magnetic (H^i) fields.

$$E^t = E^i + E^s \quad (2.16)$$

$$H^t = H^i + H^s \quad (2.17)$$

These electric and magnetic fields can be found by using various techniques that include: geometrical optics (GO), physical optics (PO), integral equations (IE) and diffraction theory to name a few [14]. In our laboratory experiments, all three types of scattering would be occurring simultaneously because the concrete slab has imbedded particles of all shapes and sizes. This includes the subsurface object that we want to identify to an air bubble inside the concrete. To accurately model the reflected signal from one of the laboratory experiments all of the scattering models would have to be taken into account. To simplify the model we could ignore all the scattering except for the scattering from the subsurface object, which in the experiments was either a steel bar or rod. Scattering from a bar can be modeled as a flat rectangular plate or a circular cylinder.

These models of the scattering can be derived a number of ways, but they all start by using Maxwell's Equations (2.5-2.9). Vector potentials are a mathematical tool that make it possible to solve for the transverse electromagnetic modes (TEM). (TEM) are either transverse electric (TE) or transverse magnetic (TM) modes. By assuming certain aspects of the geometry of the subsurface object and the type of coordinate system used,

the (TE) and (TM) can be calculated [15]. Different assumptions are made to calculate (TE) and (TM) if the object is in the near or far-field of the antenna. These will be discussed further in Section (2.4.3).

The scattering of an object can be represented by the echo area or the radar cross section (RCS), which is denoted by the Greek letter (σ). In 2D this parameter is referred to as the scattering width (SW), which is the (RCS) per unit length. The (RCS) can either be monostatic, when the transmitter and receiver are in the same location or bistatic when the transmitter and receiver are in two different locations. In our laboratory experiments the transmitting and receiving antennas were in different locations, which means that the (RCS) would be modeled as bistatic. For far-field approximations of the (RCS) where the object of interest was placed at least $(2D^2/\lambda)$ from the source, the (RCS) of a flat rectangular plate can be approximated by Equations (2.18) and (2.19). Where D is the largest dimension of the object and r is the distance to the object [14].

$$\sigma_{2D} = \begin{cases} \lim_{r \rightarrow \infty} \left[2\pi r \frac{S^s}{S^i} \right] \\ \lim_{r \rightarrow \infty} \left[2\pi r \frac{|E^s|^2}{|E^i|^2} \right] \\ \lim_{r \rightarrow \infty} \left[2\pi r \frac{|H^s|^2}{|H^i|^2} \right] \end{cases} \quad (2.18)$$

$$\sigma_{3D} = \begin{cases} \lim_{r \rightarrow \infty} \left[4\pi r^2 \frac{S^s}{S^i} \right] \\ \lim_{r \rightarrow \infty} \left[4\pi r^2 \frac{|E^s|^2}{|E^i|^2} \right] \\ \lim_{r \rightarrow \infty} \left[4\pi r^2 \frac{|H^s|^2}{|H^i|^2} \right] \end{cases} \quad (2.19)$$

These Equations were found by using the incident electric and magnetic fields shown in Equations (2.20) and (2.21) for a uniform plane wave (TE^x) and by using vector potential method to find the components of the scattered electric field (E^s) for a flat rectangular plate. Bessel and Hankel functions were also used to approximate the electric and magnetic field components. Where: β is the phase constant, θ an angle, H_0 is the constant magnitude of the incident magnetic field, $\eta = \sqrt{\mu/\epsilon}$ is the intrinsic impedance of a material [14].

$$E^i = \eta H_0 (\hat{a}_y \cos \theta_i + \hat{a}_z \sin \theta_i) e^{-j\beta(y \sin \theta_i - z \cos \theta_i)} \quad (2.20)$$

$$H^i = \hat{a}_x H_0 e^{-j\beta(y \sin \theta_i - z \cos \theta_i)} \quad (2.21)$$

The equations change for a uniform plane wave (TM^x). The (RCS) can be found for circular cylindrical objects in a similar manner. Like for the flat plate many assumptions must be done to properly model the (RCS). This includes: the angle of the incident wave, the polarization of the waves, the distance of the object relative to the antennas and the size of the object. The final equations will have the same structure as Equations (2.18) and (2.19), but the scattered and incident power densities (S^s, S^i), electric and magnetic fields will change based on the assumptions above. The geometric assumptions for electromagnetic radiation reflecting off of a flat rectangular plate and a circular cylinder are depicted in (Figure 5) and (Figure 6), respectively [14].

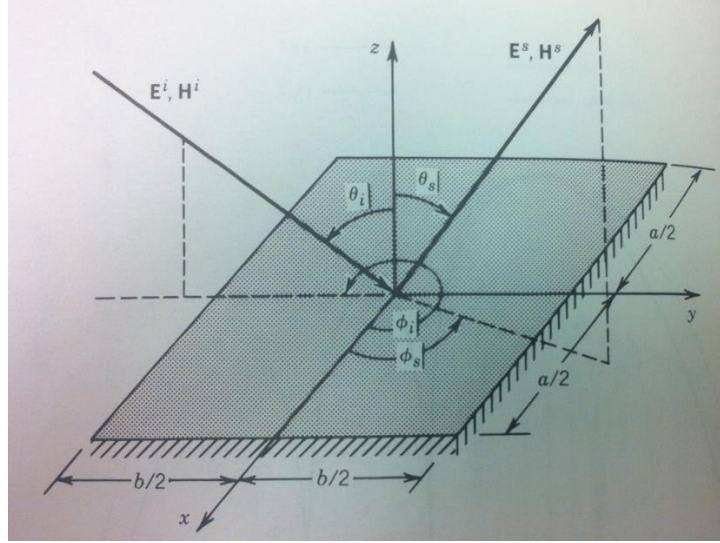


Figure 5: Uniform plane wave scattering off a rectangular plate [14].

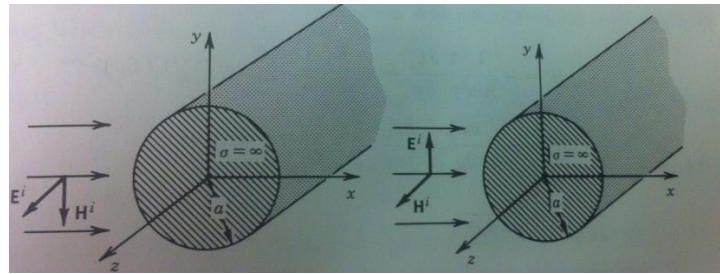


Figure 6: Uniform plane wave scattering off a circular cylinder [14].

2.4.3. Field Regions

The space that surrounds an antenna can be divided into three regions, the reactive near-field, the radiating near-field and the far-field, which can all be seen in (Figure 7). The reactive near-field is the region immediately surrounding the antenna. The outer boundary of this region can be calculated using Equation (2.22), where R is the radial distance from the antenna, D is the largest dimension of the antenna and λ is the wavelength of the emitted signal. The radiating near-field or Fresnel region is the area between the

reactive near-field and the far-field. It is possible that if the maximum dimension of the antenna is very small compared to the emitted wavelength, then this region may not exist. When the antenna is focused towards infinity this region is considered as the Fresnel region. This region is usually bonded by the inequality, shown in Equation (2.23). The far-field region or also known as the Fraunhofer region exists where $(R < 2D^2/\lambda)$. In this region the angular field distribution is basically independent of the distance from the antenna. The approximation above could be inadequate for multibeam reflector antennas [16].

$$R < .62\sqrt{D^3/\lambda} \quad (2.22)$$

$$.62\sqrt{D^3/\lambda} \leq R < 2D^2/\lambda \quad (2.23)$$

$$R < 2D^2/\lambda \quad (2.24)$$

For our experiments λ was approximately .05m and .075m at 4GHz and 6GHz, respectively. The length of the antennas was the largest dimension (D) of the antennas. Using an approximate (D) and the wavelengths at different source frequencies it was possible to calculate the bounds for each region. After calculating the bounds we could then determine the region where the subsurface object is located.

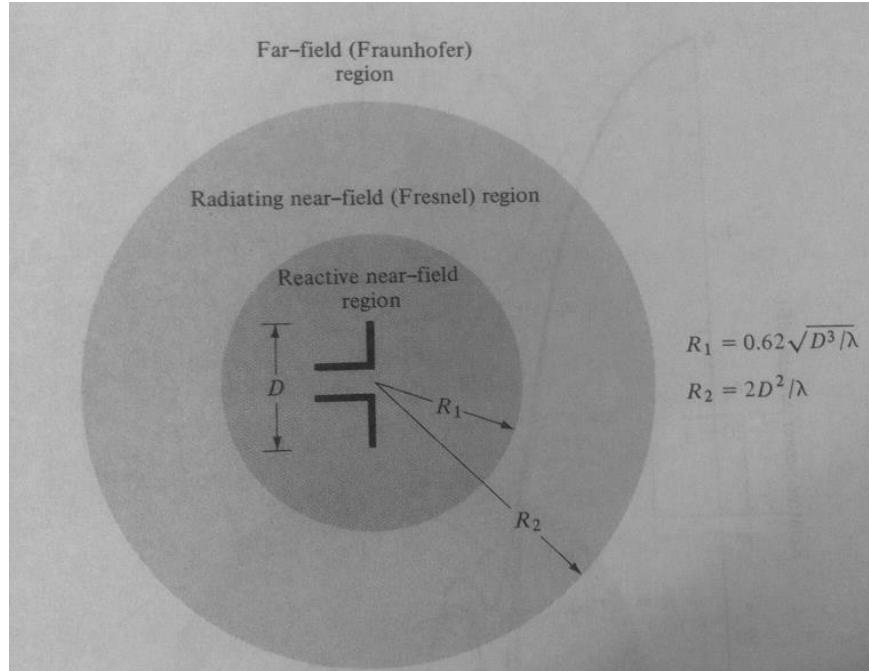


Figure 7: Antenna field regions [16].

2.4.4. Antenna Radiation Pattern

The radiation pattern of an antenna is a mathematical function or graphical representation of the radiation properties of the antenna as a function of space coordinates. Usually the radiation pattern is determined in the far-field (Fraunhofer) region and is represented as a function of directional coordinates. The radiation pattern might describe: the power flux density, radiation intensity, field strength, directivity phase or the polarization of the antenna. The most useful radiation property is the 2D or 3D spatial distribution of the radiated electromagnetic energy from the antenna. The field pattern of an antenna is a plot of the variation of the electric or magnetic field along a constant radius. (Figure 8) illustrates the electromagnetic radiation pattern and field pattern of an antenna.

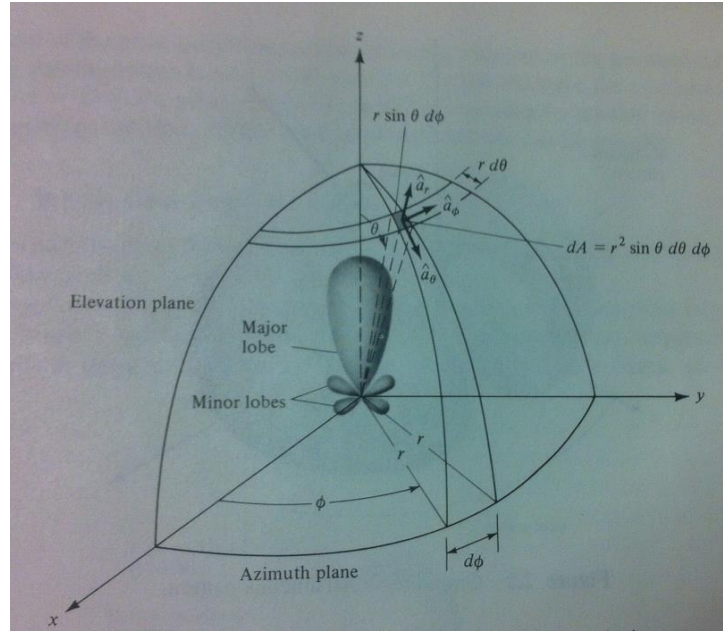


Figure 8: Coordinate system for antenna radiation pattern [16]

Radiation patterns can be categorized as either isotropic, directional or omnidirectional. An isotropic antenna radiates electromagnetic radiation equally in all directions. A directional antenna radiates electromagnetic radiation more effectively in some directions and an omnidirectional antenna radiates electromagnetic radiation in essentially no particular direction. The principal E-plane (electric) and H-plane (magnetic) determine the performance of the antenna for a linearly polarized antenna. The E-plane contains the electric-field vector and the direction of maximum radiation, while the H-plane contains the magnetic-field vector and the direction of maximum radiation. A diagram showing the E- and H-planes of an antenna can be seen in (Figure 9).

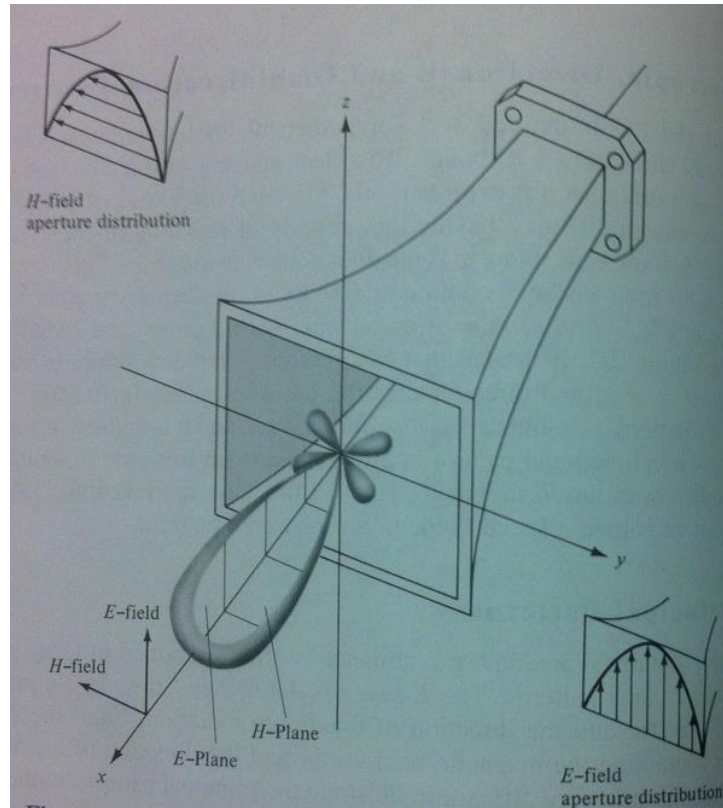


Figure 9: Principal E-Plane and H-Plane patterns [16].

The radiation pattern emitted from an antenna might consist of a number of lobes. A major radiation lobe contains the direction of maximum radiation and a minor lobe can include any lobe except the major lobe and are usually in undesired directions. Split-beam antennas might have one or more major lobes. A side lobe is usually adjacent to the major lobe and a back lobe is a radiated lobe that is approximately 180 degrees relative to the major lobe. Radiation lobes are depicted in (Figure 10). The side lobe ratio is the power density of the minor lobe over the power density of the major lobe. For most radar systems a low side lobe ratio is very important because it minimizes false target indications from the minor lobes. This means that the accuracy, reliability and performance of an antenna can be increased by reducing the size and number of minor lobes [16].

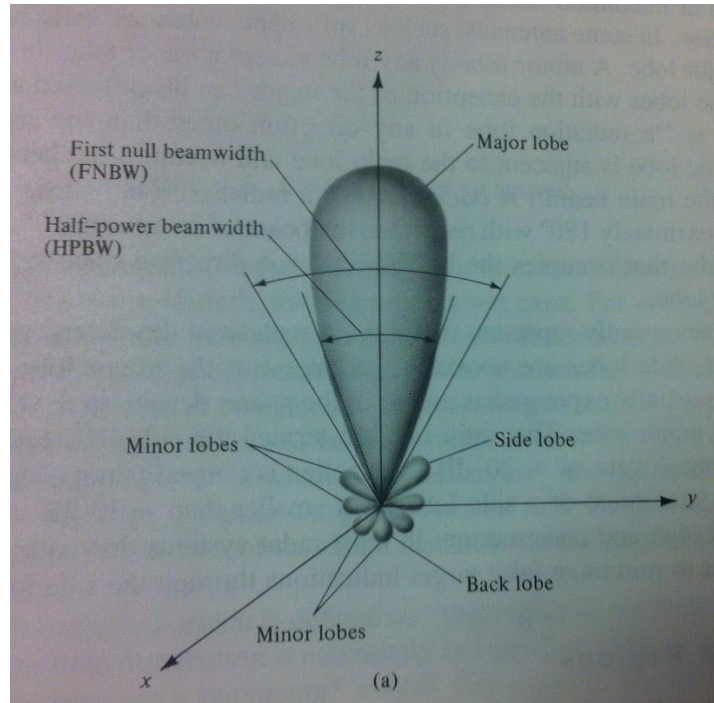


Figure 10: Diagram of radiation lobes [16].

2.5. Phased-Array Radar

Phased-array radar systems have been in use for a long time in far-field applications. They are used in airplanes and boats to detect incoming objects. An array of antennas consisting of two or more antennas, is used in phased-array radar systems. The relative phases of the signals emitted from the source antennas is varied in such a way that the effective radiation pattern of the array as a whole is enhanced in a desired direction and suppressed in an undesired direction. This is done by controlling the phase difference between the antenna elements [3, 21]. This means that the array of antennas can electronically sweep the roadway or bridge deck in fractions of a second making it possible for our system move at a faster rate. The sweep could be done mechanically with a linear

or rotational motor, but sweep time would be dependent on the motors rotational velocity. The system would have to be steady to give a good reading and the mechanism would also have to be made out of materials that do not interfere with electromagnetic radiation. This type of mechanical sweeping system becomes impractical as the sweeping speed increases.

2.5.1. Antenna Array Mechanics

An antenna array can be constructed by assembling a number of antennas in an electrical or geometrical configuration, which can enhance certain radiation characteristics. The antennas in the array do not all have to be the same, but having all of the antennas be the same does make calculating the array characteristics and parameters much easier. The geometrical configuration of the array, the distance between the antennas, the excitation amplitude and phase of an antenna, and the radiation pattern of each antenna will dictate the shape of the radiation pattern of the array [19].

The radiation pattern of an antenna array can be calculated by adding all of the electric fields radiated by all of the antennas after adjusting for their relative phases. The phasing of the radiation depends on the position and the wavevector of an antenna. Far-field approximations of the electric field have the form depicted in Equation (2.25). Where: $e^{jk \cdot r_i}$ represents the phasing term, \mathbf{r}_i is the position vector of the i th array element, $\mathbf{k} = 2\pi(\sin\theta \cos\phi, \sin\theta \sin\phi, \cos\theta)/\lambda$ and the components of the electric field are in spherical coordinates (θ, ϕ) . The arrays electric field equation below allows each element in the array to have a unique radiation pattern for the two orthogonal polarizations [17].

$$\mathbf{E} = \sum_{i=1}^N [E_{\theta i}(\theta, \phi) \hat{\boldsymbol{\theta}} + E_{\phi i}(\theta, \phi) \hat{\boldsymbol{\phi}}] e^{jk \cdot \mathbf{r}_i} \quad (2.25)$$

2.5.2. Theoretical Reflected Signal from a Two-Element Array

The simplest form of an antenna array is one that only incorporates two antenna elements. For the case with no coupling between the antennas the total electromagnetic field is equal to the sum of electromagnetic fields of both antennas. This is shown in Equation (2.26). (Figure 11) shows the geometry of the two-element array used as a model for the phased-array radar system. Equations (2.26)-(2.31) were based from the geometry depicted in (Figure 11) and were used to develop the theoretical reflected signal model for the near-field phased-array radar system [20].

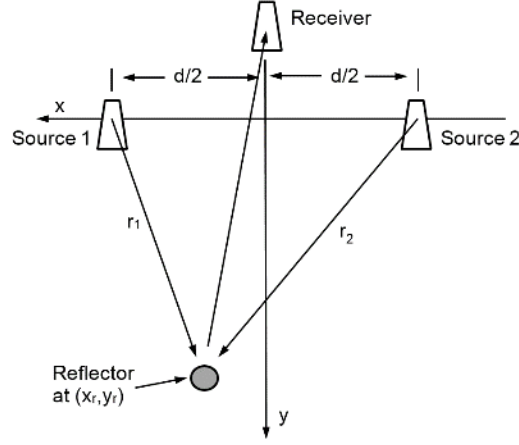


Figure 11: Phased-array setup geometry modeled after a two-element array

$$E(x_r, y_r, t) = E_1(x_r, y_r, t) + E_2(x_r, y_r, t) \quad (2.26)$$

Where the electromagnetic field from the reflector is equal to the sum of the electromagnetic fields of the source antennas.

$$E_{1,2} = A_{1,2} e^{j(2\pi f t - \varphi_{1,2} - \delta_{1,2})} \quad (2.27)$$

Equation (2.27) represents the electromagnetic fields of the source antennas. With $A_{1,2}$ as the amplitude of the signals, f as the frequency, $\varphi_{1,2}$ as the phase angles and $\delta_{1,2}$ as the additional phase angles from the time phase lag. The time phase lags incorporate the source signal directions ($r_{1,2}$). The phase angles from the time phase lag and the source signal directions depicted in Equations (2.28) and (2.29).

$$\delta_{1,2} = \frac{2\pi f r_{1,2}}{c} = \frac{2\pi r_{1,2}}{\lambda} \quad (2.28)$$

$$r_1 = \sqrt{(x_r - \frac{d}{2})^2 + y_r^2}, \quad r_2 = \sqrt{(x_r + \frac{d}{2})^2 + y_r^2} \quad (2.29)$$

By substituting, $\beta_i = \varphi_i + \delta_i$, the reflected electromagnetic field can be modified as Equation (2.30) [20].

$$E = e^{(j2\pi f t)} (A_1 e^{-j\beta_1} + A_2 e^{-j\beta_2}) \quad (2.30)$$

Finally by multiplying by the complex conjugate, turning the exponents into a combination of sines and cosines and by only dealing with real numbers, we arrive at Equation (2.31). Which represents the ideal theoretical reflected signal used to model a simplified reflected signal for the phased-array radar system.

$$E^2 = A_1^2 + A_2^2 + A_1 A_2 (\cos(\beta_1 - \beta_2) + \sin(\beta_1 - \beta_2)) + A_1 A_2 (\cos(\beta_2 - \beta_1) + \sin(\beta_2 - \beta_1)) \quad (2.31)$$

2.5.3. Mutual Coupling in Antenna Arrays

Mutual coupling between the antennas alters the overall radiation of the array. The physical optics (PO) technique, which combines the dyadic Green's function with the

electric field reaction, makes it possible to calculate the mutual impedance between the antennas [17]. The antenna arrays overall performance does not only depend on the performance of one array element, but on how the radiating patterns interact with one another. The amount of coupling between antennas primarily depends on the radiation characteristics of each antenna, the distance between the antennas and the relative orientation of each antenna. Radiated energy from one antenna might reach another due to some non-ideal directional characteristics. Mutual coupling complicates the analysis and the design of the array because it is difficult to model. Mutual coupling effects in an array cannot be generalized. This is due to the fact that many antenna parameters can influence that amount of mutual impedance of an antenna array system. Mutual couplings effect on the performance of the antenna array depends on: the type of antennas being used and its design parameters, the relative position of the antenna elements to one another, the feed points of each antenna and the scan volume of the antenna array. The parameters listed above alter the impedance of each array element, the reflection coefficients and the overall antenna field pattern. All of these will influence the overall performance of the antenna array [18].

2.5.4. Antenna Array Design Considerations

The radiation characteristics of antenna arrays can be controlled by selecting the proper phase or amplitude distribution between the antennas. Phased-array radar systems work on the premise of controlling the phase excitation of the antenna elements. Controlling the amplitude excitation between the antenna elements has been proven to control the beamwidth and the side lobe levels. This control can be done by creating a

smoother tapering effect between the antenna element amplitudes from the center of the array to the edges. A taper that is represented by a binomial distribution would decrease the side lobe level and increase the half-power beamwidth. If the distribution of the antenna amplitudes is uniform then the half-power beamwidth decreases, but the side lobe size increases. The optimal antenna array design would have both a small half-power beamwidth and a low side lobe level [22].

Electromagnetic wave propagation theory, antenna theory and the antenna design criteria listed above will be considered when designing a phased-array radar system to detect deformations, voids, cracks and corrosion in roadways and bridge decks. Results from laboratory experiments will be compared to theoretical electromagnetic radiation models of a two-element antenna array. The model and the theory will be based on far-field approximations, because it is more commonly studied. The far-field theoretical model will be compared to near-field laboratory experiments. The results will validate or invalidate the accuracy of the far-field model. The addition certain near-field approximations might explain differences that might be noted between the model and the experiments.

CHAPTER 3: METHODS

3.1. Phased-Array System Setup

3.1.1. Components used in Phased-Array Radar System

(Figure 12) and (Table 2) show and describe all of the primary components used for the phased-array radar system. For further information on a particular component specifications, datasheets can be found by searching the model numbers of the components which are given in (Table 2).

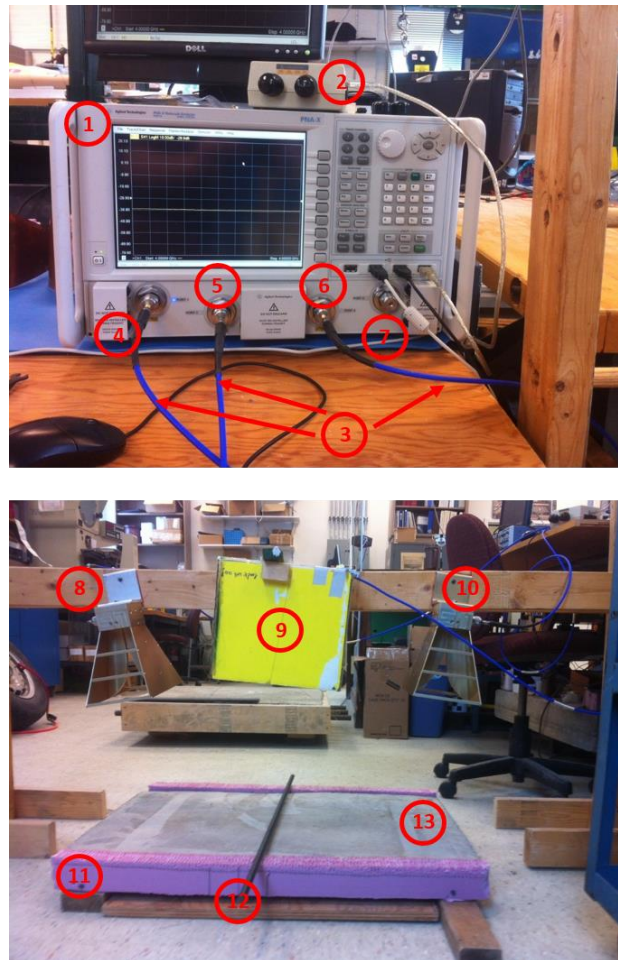


Figure 12: Components used for phased-array system

Table 2: List of Components in Figure 4

Figure 4 Label Number	Description of Object
1	Agilent Technologies PNA-X (N5241A) Network Analyzer with a Frequency range from 10 MHz-13.5 GHz
2	Agilent Technologies N4431-60006 Electronic Calibration Module with a Frequency range from 9 kHz-13.5 GHz
3	Mini-Circuits CBL-6FT-SMSM+ Coaxial Cables
4	Port 1 of Network Analyzer
5	Port 3 of Network Analyzer
6	Port 4 of Network Analyzer
7	Port 2 of Network Analyzer
8	A.H. Systems SAS-571 Double Ridge Guide Horn Antenna with a Frequency range from 700 MHz-18 GHz. Referred to as Source Antenna #1 and connected to Port 3 of Networks Analyzer by the above coaxial cables. Antenna specifications in Appendix E .
9	Handmade GIMA Antenna. Referred to as Receiving Antenna #1 and connected to Port 4 of Networks Analyzer by the above coaxial cables. Antenna specifications in Appendix F [28].
10	A.H. Systems SAS-571 Double Ridge Guide Horn Antenna with a Frequency range from 700 MHz-18 GHz. Referred to as Source Antenna #2 and connected to Port 1 of Networks Analyzer by the above coaxial cables. Antenna specifications in Appendix E .
11	Custom position rig made out of FOAMULAR 250, 2" (5.08cm) thick insulation.
12	Simulated subsurface object. Either a 3" (7.62cm) x 3/8" (.953cm) x 25.5" (65.8cm) steel bar or a 1/4" (.635cm) diameter x 35" (88.9cm) steel rod.
13	Concrete Slab made out of SAKRETE high strength concrete mix and a layer of nylon mesh to strengthen the concrete.

3.1.2. Phased-Array Antenna Setup

(Figure 12) and (Figure 13) shows the setup of the phased-array radar system that emits microwaves into a concrete slab. Two A.H. Systems double ridge horn antennas were used as the source antennas and were mounted 30" (76.2cm) apart with a home-made (GIMA) receiving antenna in between them. The antenna height was varied from being 26" (66.04cm) or 19.5" (49.53cm) above the concrete slab, which depended on the particular test conducted. A.H. Systems horn antennas were used for the experiments because they have been extensively calibrated and the antenna characteristics are known. The antenna characteristics and specifications including the radiation pattern of A.H. Systems antennas can be found in **Appendix E**, while certain antenna characteristics of the GIMA antenna from studies conducted in the past can be seen in **Appendix F**. The horn antennas are considered directional, which means that electromagnetic radiation is focused in a particular direction. To further increase the directionality of the array both antennas were angled toward each other at a 7 degree angle from vertical. Signal directionality into the concrete slab ensures that more electromagnetic energy goes into the concrete slab, increasing the penetration depth and likelihood of detection. A wooden frame was used to support the three antennas, which were hooked up to an Agilent PNA-X Network Analyzer by three Mini-Circuits coaxial cables. For all of the tests, the antennas were plugged into the same ports on the network analyzer. Source antenna #1 and source antenna #2 were plugged into Port 1 and Port 3, respectively. The receiving antenna was plugged into port 4 of the network analyzer. Rigs made out of FOAMULAR 250, 2" (5.08cm) thick

insulation were used to precisely move a steel bar or rod, which acted as our subsurface objects. The rigs made it possible to move the subsurface objects across the concrete slab precisely at: 3" (7.62cm), 1/2" (1.27cm), or 1/4" (.635cm) increments, depending on the test. Insulation was chosen as the rig material because it mostly consists of air, minimizing any interference that the antennas might pick-up from a rig. To test the performance of the phased-array system, we emitted electromagnetic radiation from the two source antennas toward the concrete slab. To electronically steer the radiation the phase angle of the emitted signal from source antenna #2 was varied by utilizing the phase sweep function on the network analyzer. The reflected signal from the subsurface object at each position across the concrete slab was recorded. The amount of position points depended on the certain position rig used in the test.

3.2. Network Analyzer Software Setup

The Agilent PNA-X network analyzer has many functions and capabilities. It has the built-in capability to offset the phase of an array of antennas. For the phased-array radar system we could have built a device that could offset the phase of an antenna array. Without extensive testing the accuracy and reliability of the device would be unknown, which would affect the results acquired by the radar system, making them inaccurate and unreliable. The reliability of a system in series is lower than the reliability of a system in parallel. This can be checked by calculating the reliability of a system in series and in parallel by using Equation (3.1) and (3.2), respectively. Where R_i is the reliability function of component i and $R_s(t)$ is the reliability of the whole system [12, 13].

$$R_s(t) = \prod_{i=1}^n R_i(t) \quad (3.1)$$

$$R_s(t) = 1 - \prod_{i=1}^n (1 - R_i(t)) \quad (3.2)$$

Agilent has tested and proven the accuracy and reliability of the phase sweep feature on the PNA-X network analyzer. The accuracy and reliability of the network analyzer and the time saved by using a programmed feature rather than building and testing a custom device was the reason the PNA-X network analyzer was chosen to emit and receive the signals. Getting familiar with the network analyzer software takes some time. **Appendix C** outlines how to properly setup the network analyzer software to calibrate cables, run a phase sweep and run an S-Parameter send and receive test. For further information on further functions for the network analyzer read Agilent's PNA-X network analyzer *Programming Guide* and *Service Guide*, which correspond to References [4] and [5].

3.3. Laboratory Experiments

The objective of this study was to create a phased-array radar system that could accurately and reliably detect subsurface objects of various shapes and sizes. We conducted multiple tests that varied certain variables to experimentally observe which configuration enhanced the performance of the system. The performance of the system can be determined by observing the magnitude and resolution of the reflected signal. A stronger reflected signal means a greater probability of detection, which correlates to an overall increase in

the accuracy and reliability of the system. The tests conducted in this study made it possible to observe how the electromagnetic energy from the reflected signal changes as we vary: the depth at which the subsurface object is under a concrete slab, the increment size of the position of the subsurface object as it moves across the concrete slab, the frequency of the source signal, the height at which the antennas are over the concrete slab and the orientations of the antennas relative to each other. A diagram of the physical phased-array radar test system can be seen in (Figure 13).

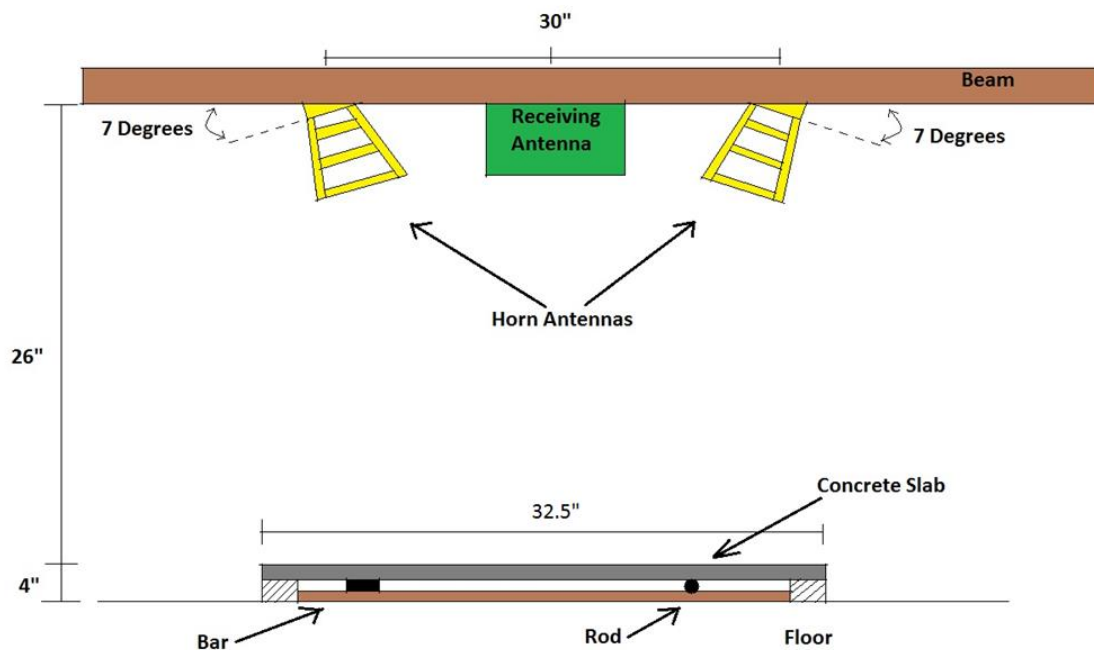


Figure 13: Phased-array system laboratory setup

3.3.1. Different Concrete Slab Configurations

The principles that dictate the penetration depth of regular GPR also apply to phased-array GPR. There is a set limit to the penetration depth at a given frequency through a particular material, which depends on how the electromagnetic energy is dissipated by

the material. Constructive and destructive interference occurs as the phases from the source signals are varied from 0 degrees to 360 degrees. This corresponds to an increase in electromagnetic energy in a certain direction and a decrease in another. At a location where there is constructive interference the electromagnetic energy is greater, which corresponds to an area of increased penetration depth.

As the source signal travels further into the desired material more electromagnetic energy is dissipated into the surrounding material, which includes air. This means that a signal reflected from a subsurface object at a greater depth will have a smaller magnitude than an object that is closer to the surface. The three configurations depicted in (Figure 14) tested how the magnitude of the reflected signal decreased as more concrete is placed over the subsurface object.

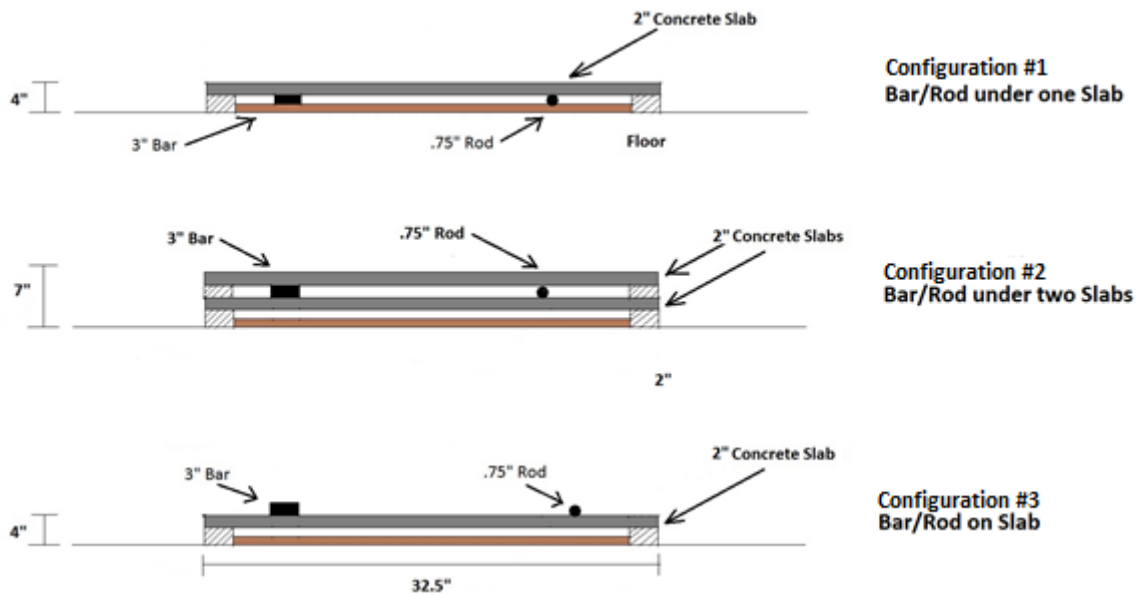


Figure 14: Concrete slab configurations

The concrete slabs used in all the test had dimensions of 32.5" (82.55cm) x 21" (53.34cm) x 2" (5.08cm). They were made many years ago from a SAKRETE high strength concrete mix with a layer of nylon mesh to reinforce the concrete slab. Before being used for these tests the slabs withstood years of abuse from the harsh exterior climate of Burlington Vermont, which cycle from 95 degrees Fahrenheit in the summers to -30 degrees Fahrenheit in the winter. The concrete slabs show signs of degradation and cracking that were mentioned in Chapter 2.

For all of the slab configurations a steel bar or rod was used as the subsurface object, which moved across the concrete slab at certain increment sizes ranging from 3" (7.62cm) to ¼" (.635cm). Custom position rigs, shown in (Figures 15-17) keep the steel bar or rod in place as the reflected signal was recorded.

3.3.2. Position Increment Step Size

When the phased-array system is mounted or implemented onto a moving vehicle the entire systems will be moving. The size limitations of the lab and the scale of the antenna support structure made moving the antennas over the concrete difficult to create repeatable tests. That was the reason why we decided to keep the antennas stationary and move the subsurface object across the concrete slab. The position rigs with constant increment sizes made experiments easy, accurate and repeatable.

The position rigs, which are shown in (Figure 15-17) allowed us to test the resolution of the phased-array radar system, while holding the steel bar or rod securely in place. For this study the resolution can be defined as the smallest increment size between amplitude peaks of the reflected signal. The position rig shown in (Figure 15) was a piece

of particle board with markings at 3" (7.62cm) intervals. A total of eight positions spanned across the concrete slab covered a distance of 24" (60.96cm). The rigs shown in (Figure 16-17) were made out of FOAMULAR 250, 2" (5.08cm) thick insulation. This type of material was used because of its material properties that were similar to air. FOAMULAR 250 insulation is comprised of polystyrene and air, which have a dielectric constant of 2.6 and 1, respectively. The low dielectric constant means that signals from the antennas will not be greatly affected by this material and the signal will behave as if it were traveling through air, minimizing interference produced from the rig. This material was also rigid and was easily pliable. The position rig shown in (Figure 16) had 21 notches with an increment size of $\frac{1}{2}$ " (1.27cm), which covered approximately 10" (25.4cm) of the concrete slab. When experiments were conducted using this position rig, the rig was placed in the middle of the concrete slab, beneath the receiving antenna. The position rig shown in (Figure 17) had 125 notches with an increment size of $\frac{1}{4}$ " (.635cm), which covered approximately 31" (78.74cm) of the concrete slab.

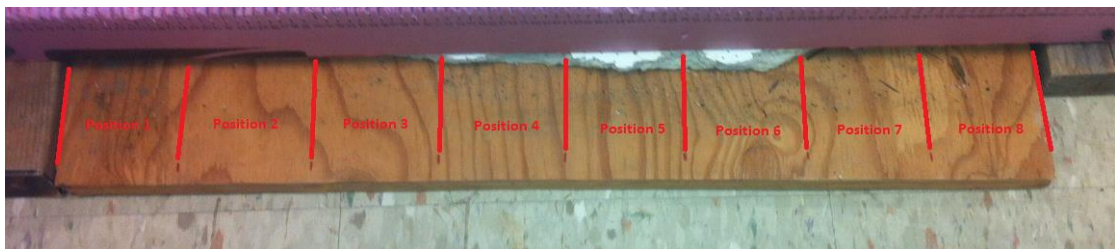


Figure 15: Position setting rig with 3" (7.62cm) increment size



Figure 16: Position setting rig with $\frac{1}{2}$ " (1.27cm) increment size



Figure 17: Position setting rig with $\frac{1}{4}$ " (.635cm) increment size

3.3.3. Varying Source Frequencies

Varying the source signals made it possible to investigate which frequency and power level gave the best readings. Multiple experiments were done with source frequencies varying from 2GHz to 8GHz. Emitting signals with higher frequencies decreases penetration depth, but enhances resolution and it might possible that at these frequencies the air-coupled phased-array radar system might be able to detect non-linear

scattering. Corrosion scattering is believed to act non-linearly and if the frequency is high enough, our system might be able to detect harmonics from the corrosion. The main goal of these tests was to see if the resolution of the subsurface object gets any better as the frequency of the source signals is increased.

3.3.4. Varying Antenna Height

The majority of commercial GPR is ground-coupled. Having the antennas emit electromagnetic energy at the surface of the desired material increases the strength of the reflected signal, eliminating the possibility of the energy from a signal dissipating as it travels through air. Ground-coupling the phased-array GPR system would increase: the directionality of the source antennas, the penetration depth and the strength of the reflected signal, but it will likely cause a decrease in scanning time and an increase in maintenance. If the antennas were ground-coupled they would have to be placed on sliding plates, which would frequently have to be replaced due to the friction between the roadway and the plates. Vibrations from hitting small imperfections at highway speeds on the roadway could cause major damage to the antenna system. Vibrational damage to the antenna system can be averted by having the antennas suspended in air by a system of shocks and vibrational dampers.

By having the phased-array system air-coupled we know that some of the source signals electromagnetic energy will be dissipated into the air. Previous test conducted on the GIMA antenna concluded that the attenuation of electromagnetic energy through air was approximately 6.56dB/m (2dB/ft) or 4.53mW/m. This value was found by utilizing equations found in Reference [25] and conducting tests with two GIMA antennas that were

placed face to face with each other and varying the distance between them. These tests were conducted by UVM colleagues Anbu Venkatachalam and Zhang Yu.

The tests varying the antenna height were constructed to obtain the optimal antenna height based on the strength of the reflected signal with the least amount of dissipated electromagnetic energy. Increasing the strength of the reflected signal also increases the likelihood that a subsurface is detected. By testing the phased-array GPR system at multiple heights at different source frequencies and power, we would be able to find the optimal configuration to maximize the strength of the reflected signal. We tested two different heights, 26" (66.04cm) and 19.5" (49.53cm). The height was measured from the surface of the concrete slab to the bottom of the beam that supports the antennas, which is depicted in (Figure 13).

3.3.5. Changing Antenna Orientations

We tested three different antenna configurations, which can be seen in (Figures 18-20). In the figures the antennas are represented by the black outlined rectangles. The black triangles within the rectangles represent the fins or ridges that emit the signal and the red dashed circles represent the approximate antenna lobe shape. For an accurate representation of the antenna lobes, the antennas shapes and dimensions must be imported into some sort of electromagnetic radiation modeling software like HFSS. The simulated lode shape of the A.H. Systems horn antennas and the GIMA antenna can be found in **Appendix E** and **Appendix F**, respectively. For consistency the antennas were spaced in increments of 15" (38.1cm) with the two source antennas 30" (76.2cm) apart from each other and the receiving antenna between them. From Section 2.4.4 and 2.5 we are aware

that the shape of the radiation pattern and the size and shape of side lobes influences the overall performance of the phased-array system. Without knowing the exact properties and dimensions of the radiation pattern, we decided to test the overall performance of the array by changing the antenna orientations. Changes in the antenna orientation allowed us to see which configuration was more effected by mutual coupling and changes in the feed point locations.

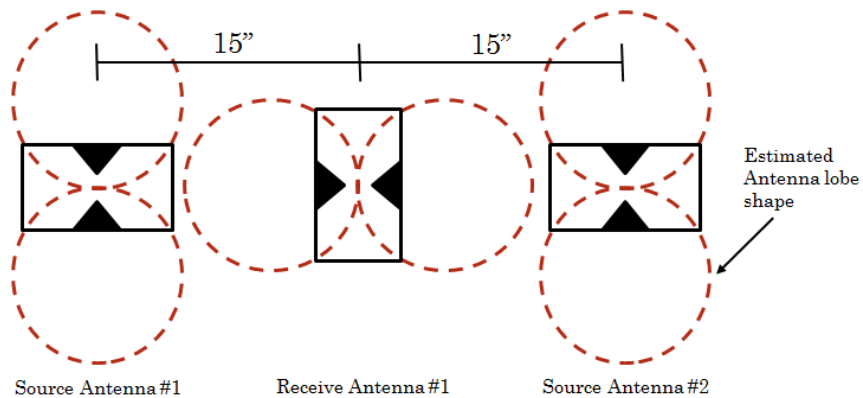


Figure 18: Antenna Configuration #1

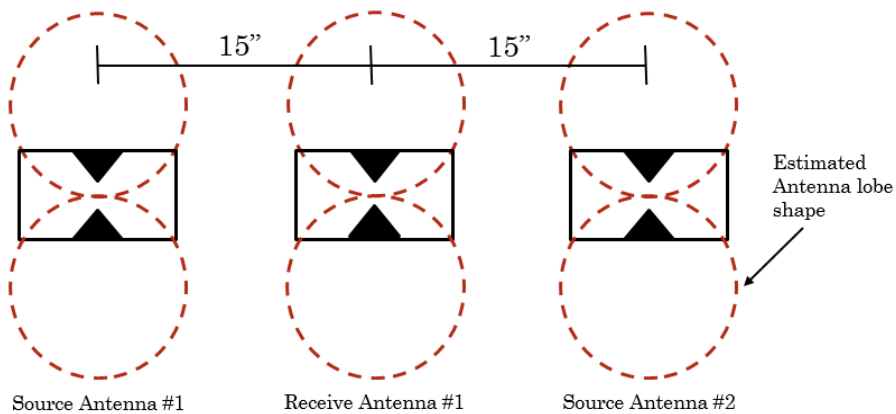


Figure 19: Antenna Configuration #2

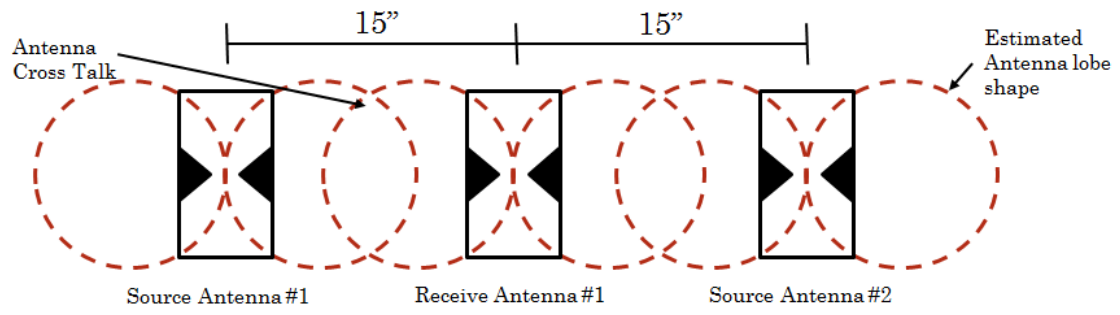


Figure 20: Antenna Configuration #3

CHAPTER 4: RESULTS AND DISCUSSION

4.1. Varying Concrete Slab Configurations

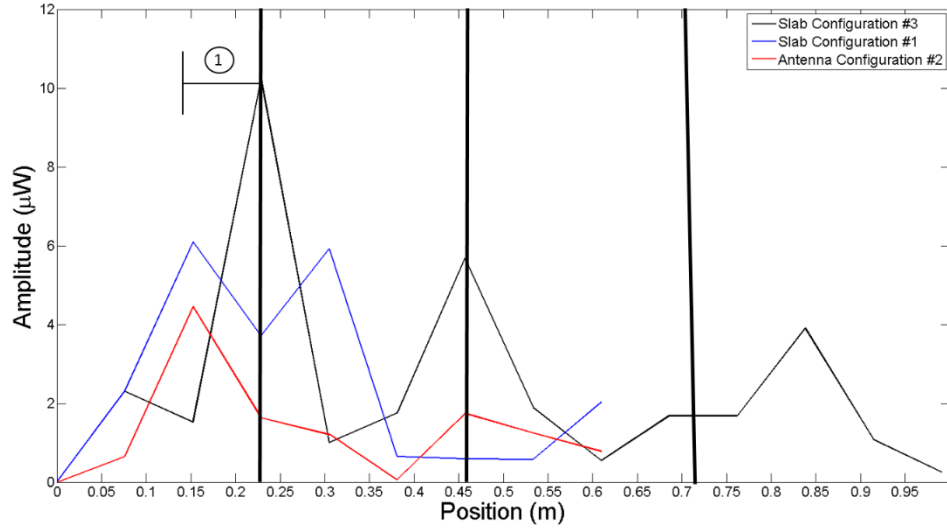


Figure 21: Maximum amplitude reflected signals when the slab configurations were varied. For all slab configurations this occurred at a phase offset of 180 degrees. The vertical black lines represent the locations of the antennas. Two different position rigs were used and location 1 shows the 3” (7.62cm) shift between the two.

The data gathered to produce (Figure 21) came from Tests 3, 4a and 5a. The test parameters are shown in (Table 3) and (Table 4). Looking at (Table 3), we notice that for these two tests the only test parameter that changed was the concrete slab configuration as the metal bar moved across the concrete slab. (Table 3) and (Table 4) are in **Appendix A** and **Appendix B**, respectively.

We notice a decrease in the amplitude of the reflected signal as the subsurface object moves across the concrete slab for configuration #3. It is evident that the major peaks occur under the source and receiving antennas, represented by the solid black vertical lines in (Figure 21). The third peak does not seem to occur directly under source antenna #2.

This result could be attributed to poor resolution at an increment size of 3'' (7.62cm) or from a unique interaction between the side lobes of the GIMA receiving antenna and source antenna #2. The decrease in amplitude as the bar moves across the concrete slab could also be due to a power balance issue between source antenna #1 and #2.

From the first test, we suspected that some of the components used in the phased-array system may have been faulty. We suspected the Mini-Circuits coaxial cables and one of the A.H. Systems horn antennas. It was brought to our attention that one of the antennas was damaged before the start of the experiments. It was unclear if it was damaged during transport or if it was damaged when it was loaned out to another university. There was noticeable damage on the antenna ridge that emits electromagnetic radiation and outer surfaces of other components, which could alter the radiation field pattern of the antenna. We suspected that the system was not working correctly when we noticed a lack of symmetry in the reflected signal under source antenna #1 and #2. That was the reason why we saw a decrease in peak amplitude as the subsurface object moves towards source antenna #2, which can clearly be seen in (Figure 21) for all slab configurations.

These initial experiments that examined the strength of the reflected signal as the depth of the subsurface was varied, were all conducted using antenna orientation #1. The test parameters can be verified in (Table 3). In this particular configuration, the radiation pattern of the GIMA antenna was thought to radiating a larger area of the concrete slab, while the two horn antennas are oriented in a manner where their radiation area was thought to be smaller. In this configuration there was less interaction between the radiation patterns of the antennas, which contributed to a weaker reflected signal. The interaction of

the radiation patterns can be visualized better by superimposing the diagram of the antenna orientation in (Figure 18) and the simulated radiation patterns of the antennas in **Appendix E** and **Appendix F**. It is possible that the magnitude of a side lobe on source antenna #2 was increased when it was damaged. The interaction between the side lobe and the radiation pattern of the receiving antenna could explain the decrease in signal strength under source antenna #2. Recalibrating the antenna and determining its new radiation pattern would prove this assumption. The assumption could also be verified if the exact same test was conducted with a new antenna. (Figure D.16) in **Appendix D** depicts a phase sweep test with a new source antenna #2. The test parameters used to produce (Figure D.16) were not the same as the ones for Tests 3, 4a and 5a, but we notice an increase in the symmetry of the reflected signal when the signal under source antenna #1 and #2 are compared. This gives further evidence that damage to the antenna was effecting the amplitude of the reflected signal under source antenna #2.

Before we had the resources to purchase a new A.H. Systems double ridge horn antenna, we decided to solve the power balance issue by increasing the power to port 3 of the network analyzer. Several tests were conducted which concluded that a 7dB power difference between port 1 and 3 leveled the amplitude of the reflected signal under the source antennas. The increase in power made symmetry under the source antennas noticeable. The variance in port power throughout multiple tests is cataloged in (Table 4).

(Figure 21) shows that the amplitude of the reflected signal, which represents the amount of electromagnetic energy that is reflected back from the subsurface object, decreases as the depth of object under the slab increases. This agrees with the logic that

electromagnetic energy becomes more dissipated or scattered as the signal travels further into a material. The penetration depth of the array depends on the amount of dissipated and scattered electromagnetic radiation.

The dissipation of electromagnetic energy or the attenuation of the phased-array system through the concrete slab was unknown. Tests conducted by my colleagues Anbu and Yu concluded that for the GIMA receiving antenna the attenuation of electromagnetic energy through air was approximately 6.56dB/m (2dB/ft) or 4.53mW/m [25].

Scattering effects decrease the amount of electromagnetic radiation received by the GIMA antenna. Referring back to Section 2.4, the amount of radiation scattered is dependent on the size of the subsurface object. The size of the object dictates which approximation can be used to calculate the extent of the scattering.

Results from (Figure 21) demonstrated that slab configuration #3 produced a reflected signal with the greatest amplitude, meaning that less electromagnetic radiation was dissipated or scattered. This was due to the fact that the signal did not have to travel through the concrete slab since the object was placed on top of the slab. This configuration eliminates complexities that arise when electromagnetic radiation has to travel through another media. The simplicity of this configuration allows us to better observe how the interactions between the antennas effect the performance of the array. This was the reason that future tests were conducted using slab configuration #3.

4.2. Varying Increment Size

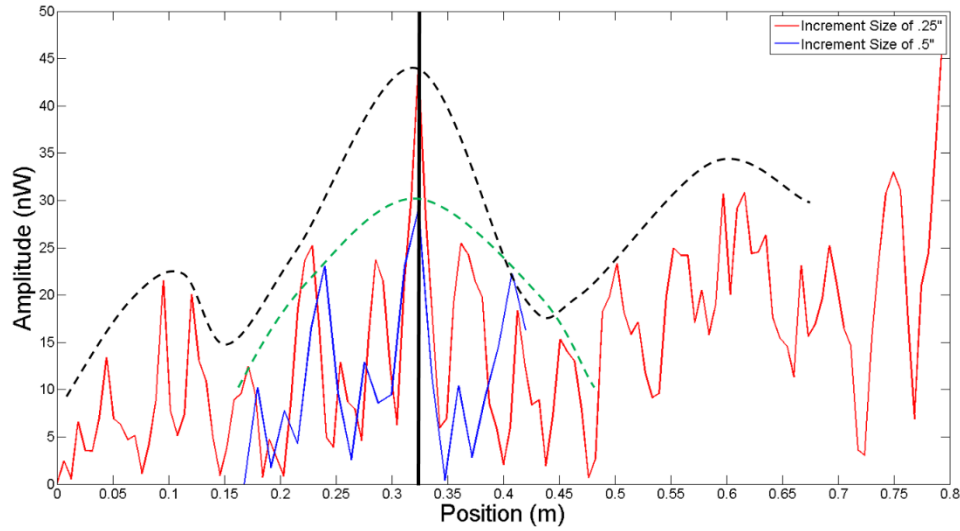


Figure 22: Maximum amplitude reflected signals when the increment size was varied. For 0.25” (0.635cm) increment size the phase offset was at 315 degrees and for .5” (1.27cm) increment size the phase offset was at 135 degrees. The vertical black line represents the location of the receiving antenna and the black and green dashed lines represent the approximate signal envelopes.

4.2.1. Comparison between Different Increment Sizes

The data gathered to produce (Figure 22) came from Tests 10 and 13. The test parameters are shown in (Table 3) and (Table 4). Looking at (Table 3), we notice that for these two tests the only test parameter that changed was the increment size of the metal rod moving across the concrete slab. (Table 3) and (Table 4) are found in **Appendix A** and **Appendix B**, respectively.

The number of data points varied between the two tests. Test 10 consisted of 21 data points and only spanned a 10.5” (26.67cm) center section of the concrete slab, while Test 13 had 125 data points and spanned the entire concrete slab. In (Figure 22), the location under the receiving antenna is represented by the solid black vertical line at

0.3238m. The reflected signal at 0.5" (1.27cm) increment size is represented by the solid blue line, while the signal at 0.25" (.635cm) increment size is depicted by the solid red line. The dashed lines correspond to the approximate envelopes of the reflected signals, with the green line representing an increment size of .5" (1.27cm) and the black line representing an increment size of 0.25" (.635cm).

We noticed that the approximate envelope for the increment size of 0.25" (0.635cm) has three pronounced peaks. The major peak was under the receiver antenna and smaller peaks under the source antennas. A similar trend was observed in the envelope for the signal at 0.5" (1.27cm) increment size. In the figure, the large peak was clearly under the receiving antenna, but since the position rig for Test 10 only covered the middle section of the concrete slab it was not possible to see the smaller peaks under the source antennas. The approximate envelope of the reflected signal at 0.5" (1.27cm) increment size under the receiving antenna was also smaller and more gradual than the one at 0.25" (0.635cm) increment size.

The apparent shape of reflected signal envelope was caused by the interactions between the antennas radiation patterns. The radiation characteristics of antenna arrays can be optimized by selecting the proper phase or amplitude distributions between the antennas, which control the beamwidth and the shape of the side lobes. The type of distribution that describes the radiation pattern of the phased-array governs the efficiency of the system. A radiation pattern represented by a binomial distribution would have a low side lobe level and a large half-power beamwidth. While a radiation pattern represented by uniform distribution would have a large side lobe level and a low half-power beamwidth. The

reflected signal from the array reaches its optimal levels when a smooth tapering effect between the antennas radiation pattern is observed from the center of the array to the edges. For this to occur, the distribution that represents the combined radiation pattern of the array must be somewhere between a binomial and uniform distribution. The ideal distribution would have both a low side lobe level and half-power beamwidth [22]. Currently, there are no simulated models of the interactions between the radiation patterns of the antennas. The magnitude of the reflected signal and the envelope are indirect indicators of the interaction of the radiation patterns. From the results gathered in (Figure 22), the envelopes of the reflected signals for the two different increment sizes seem to be represented by some sort of binomial distribution. The evidence for this assumption is shown by the large sharp peak under the receiving antenna. For this antenna configuration it can be concluded that an increment size of 0.5” (1.27cm) represents a more optimal array configuration due to the smoother tapering of the envelope, even if the amplitude of the signal is less.

The frequency (f) of the source signals for both of these tests were at a 4GHz. Using Equation (4.1), the wavelength (λ) of the source signals was calculated to be 0.07495m. Where the speed of light (c) is equal to 299,792,458m/s.

$$\lambda = \frac{c}{f} \quad (4.1)$$

Under ideal circumstances with correct scattering assumptions the reflected signal from the interaction of two source signals at 4GHz would look roughly like a sign wave, with the period of the wave equal to λ or .07495m. Noise from the surroundings, antenna coupling or crosstalk, the interaction of the radiation patterns from the antennas and scattering effects would all contribute to distort the appearance of the reflected signal.

At an increment size of 0.5" (1.27cm) there seemed to be a greater difference in amplitude between the large primary peaks and the smaller secondary peaks. This difference is not as pronounced for the test at 0.25" (0.635cm) increment size. For our experiments λ was approximately 0.075m and 0.05m at 4GHz and 6GHz, respectively. The measured distance between the large major peak and the smaller secondary peak for the signal at 0.5" (1.27cm) increment size was 0.048m. The distance to the next primary peak was 0.084m. This was close to being $\lambda/2$ and λ at 4GHz. The measured distance between the large major peak and the next peak which happened to be the secondary peak for the signal at 0.25" (.635cm) increment size was 0.0381m. The distance to the next primary peak was .0889m. We again notice that the distance was close to being $\lambda/2$ and λ at 4GHz. From these results it was uncertain which antenna parameters were contributing to the deviations of the peak distances from $\lambda/2$ and λ . The increase in amplitude of the secondary peak as the increment size was decreased could be attributed to radiation effects that occur in the near-field.

The field of operation of the antennas was calculated by using Equations (2.22-2.24) from Section 2.4.3. The length of the antennas was the largest dimension (D) of the antennas, which was approximately .2m for both the home-made GIMA antenna and the A.H. Systems horn antennas. Using the approximate (D) and the wavelengths at different source frequencies it was possible to calculate the bounds for each region. At 4GHz the reactive near-field region ended 0.25m from the antenna and the far-field region began 1.6m from the antenna. At 6GHz the reactive near-field region ended 0.202m from the antenna and the far-field region began 1.07m from the antenna. Looking at (Table 3), which

lists all of the phased-array tests that were conducted, we noticed that the antennas were either 19.5” (49.53cm) or 26” (66.04cm) from the subsurface object. The longest distance that the electromagnetic radiation must travel, which was represented by a vector from source antenna #2 to the first position of the subsurface object at an antenna height of 26” (66.04cm) was approximately 36” (91.44cm). This concludes that the subsurface object was located in the radiating region or Fresnel region of the antennas even when the frequency of the signal was at 6GHz.

4.2.2. Comparison with Theoretical Reflective Model

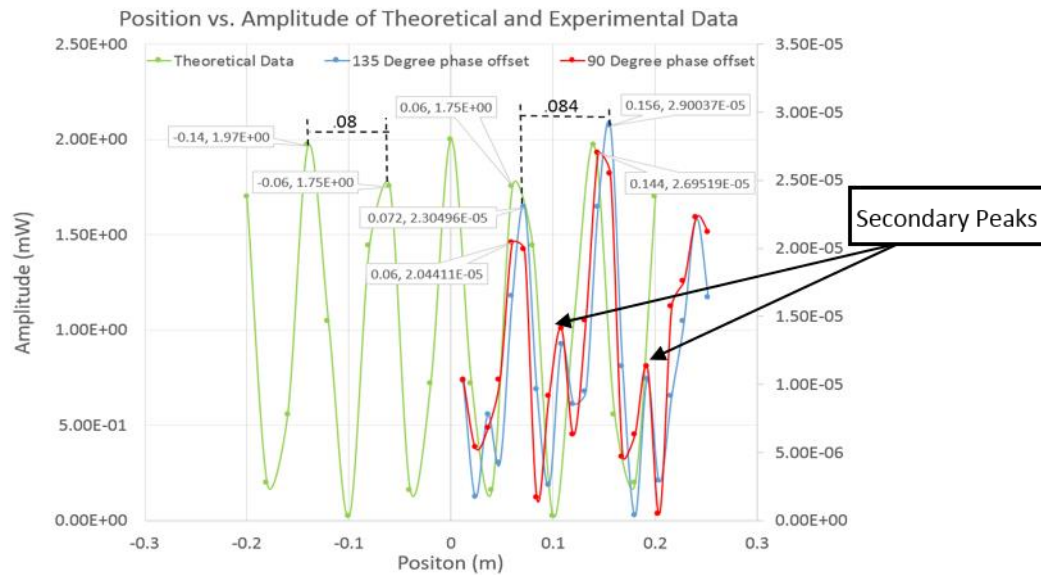


Figure 23: Theoretical reflective signal compared to the reflected signals acquired during Test 10 at an increment size of .5” (1.27cm).

When initially proposing assumptions and approximations it was logical to begin with the simplest case and increase the complexity in small increments to better observe the changes to the model. The theoretical reflective model for our phased-array radar system assumed a far-field approximation, geometric scattering and no mutual coupling.

These assumptions produced the mathematical model of the reflected signal described in Equation (2.31) which was based on the geometry of the phased-array system depicted in (Figure 11). When the simplistic theoretical reflective model was compared to the experimental test at 0.5" (1.27cm) increment size certain differences and similarities arose, which can be seen in (Figure 23). In the figure the solid green represents the theoretical reflective model, while the solid blue and red lines represent the experimental data at two different phase offsets, which were acquired from Test 10 at an increment size of 0.5" (1.27cm). For the experimental data to better fit the theoretical model, previous assumptions made to construct the model would have to be changed. A more accurate and complex model could be created by incorporating mutual coupling, Rayleigh or Mie scattering approximations and near-field approximations.

(Figure 23) clearly shows the absence of secondary peaks in the theoretical reflective model. Incorporating near-field or Fresnel approximations into the mathematical model might introduce secondary peaks to the model and explain the peaks that arise in the experiments. The simple mathematical model used in (Figure 23), accurately predicts the locations and distances between the primary peaks. The peak distance for the theoretical reflective model was 0.08m while the primary peak distance for the experimental reflective signal was 0.084m. The 0.004m (5%) difference in the peak-to-peak distance was reasonably accurate for a very simplistic model of the reflected signal.

4.3. Varying Antenna Height

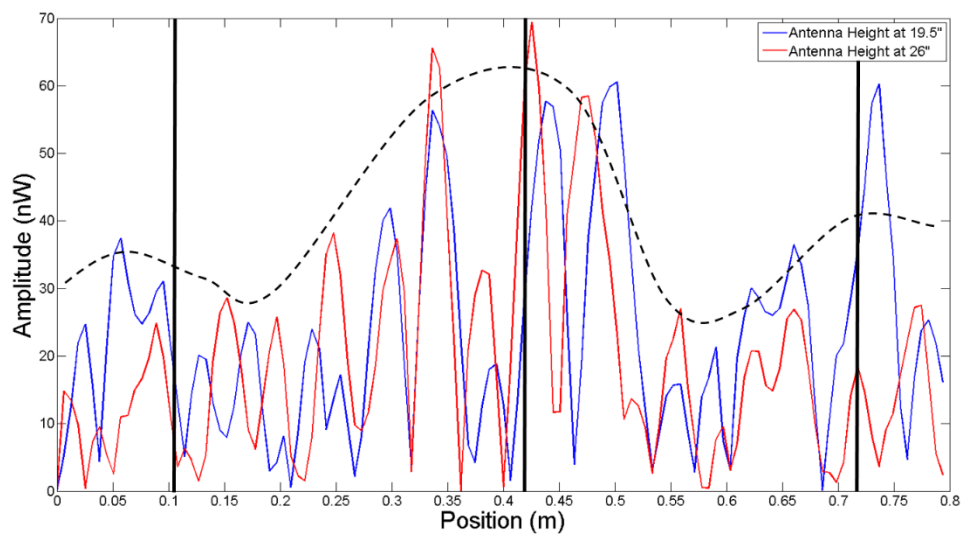


Figure 24: Maximum amplitude reflected signals when the antenna height was varied. At 19.5" (49.53 cm) the phase offset was at 315 degrees and at 26" (66.04cm) the phase offset was at 225 degrees. Vertical black lines represent the locations of the antennas and the black dashed line represents the approximate signal envelope.

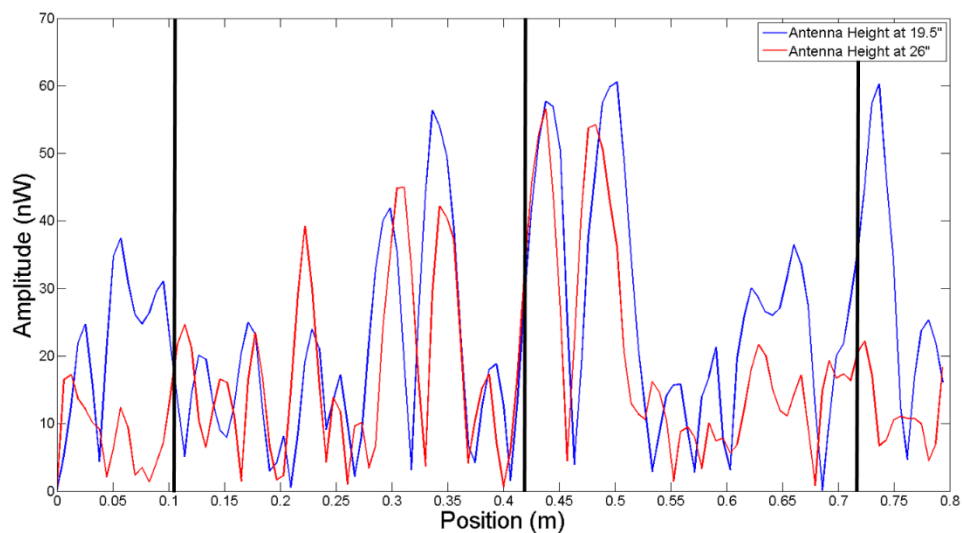


Figure 25: Reflected signals at 315 degree phase offset when the antenna height was varied. Vertical black lines represent the locations of the antennas.

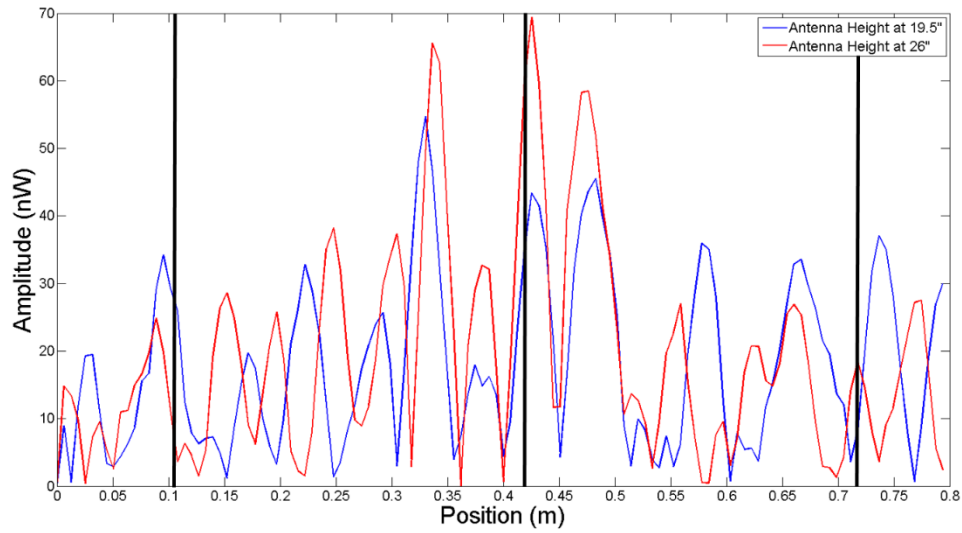


Figure 26: Reflected signals at 225 degree phase offset when the antenna height was varied. Vertical black lines represent the locations of the antennas.

The data gathered to produce (Figures 24-26) came from Tests 25 and 28. The test parameters are shown in (Table 3) and (Table 4). Looking at (Table 3), we notice that for these two tests the only test parameter changed was the height of the antennas. (Table 3) and (Table 4) are found in **Appendix A** and **Appendix B**, respectively.

For (Figure 24-26), the vertical black lines represent the locations of the antennas and in (Figure 24) the black dashed line represents the approximate envelope of the reflected signals. In (Figure 24), we noticed that the amplitudes were similar in both situations. We noticed that the amplitude was higher when the subsurface object was under the receiving antenna at an antenna height of 26" (66.04cm). This seemed counterintuitive because the reflective signal would increase as the height of the antennas decreased. This is due to the fact that less electromagnetic energy would be dissipated by the surroundings since the electromagnetic radiation travels a shorter distance. The reflective signal detected

by the receiving antenna is composed of multiple signals interacting with each other, creating constructive and destructive interference due to differences in the phase angles of the signals. The results shown in the figures depict the superposition of the two source signals interacting at different phase offsets, the mutual coupling from the two source antennas with the receiving antenna and noise signals from the environment. Constructive and destructive interference between all of these signals might explain why the strength of the reflected signal was larger when the subsurface object was under the receiving antenna at an antenna height of 26" (66.04cm) and less when the antenna is 19.5" (49.53cm) above the object.

Strong mutual coupling signals and other strange radiation pattern interactions are most likely caused by large minor or side lobes. The number and size of these minor or side lobes depends on the antenna characteristics and these effects could be magnified or altered depending on the array geometry and state of the antennas. This includes damage sustained by the antennas. Smaller side lobe size decreases the probability of a false detection due to the decrease of electromagnetic radiation in an undesired direction. Reducing the size and number of minor or side lobes increases the accuracy, reliability and performance of an antenna or antenna array. If the lobe dimensions of the antennas and the radiation lobe interactions between the antennas are known, the phenomenon could be accurately explained [16].

At the locations under the source antennas, represented by the two outer black vertical lines, the amplitude of the reflective signal increased by approximately 10nW to 20nW, depending on the phase offset of the reflected signal as the antennas were lowered

to 19.5" (49.53cm). The same phenomenon occurred in both (Figure 25) and (Figure 26) which compared the reflected signals at different antenna heights at a 315 degree phase offset and a 225 degree phase offset, respectively.

A more intuitive phenomenon occurred under the source antennas. The amplitude of the reflected signal increased as the antenna height was decreased. This can be explained by the fact that more electromagnetic energy is dissipated as the distance that the electromagnetic radiation travels increases. The rate at which electromagnetic energy dissipates also depends on the particular media the electromagnetic radiation travels through. During these test the distance that the signals had to travel through varied by approximately 6" (15.24cm). The signals emitted from the antennas traveled the distance between the antennas and the subsurface object twice. This increased the distance traveled through air between the tests to 12" (30.48cm). Using the approximate attenuation of the GIMA antenna which was 2dB/ft (4.53mW/m), approximately 1.6mW of electromagnetic energy would be dissipated into the air as the signal traveled this distance. Due to the complexity of the radiation pattern of the phased-array, this approximation for the dissipation rate is likely not accurate for an array. From this rough approximation of the dissipation rate, we can conclude that the difference in signal strength under the source antenna was attributed to a decrease in electromagnetic energy dissipation in air and concrete, as the distance between the antennas and the concrete slab were decreased.

4.4. Varying Source Frequency

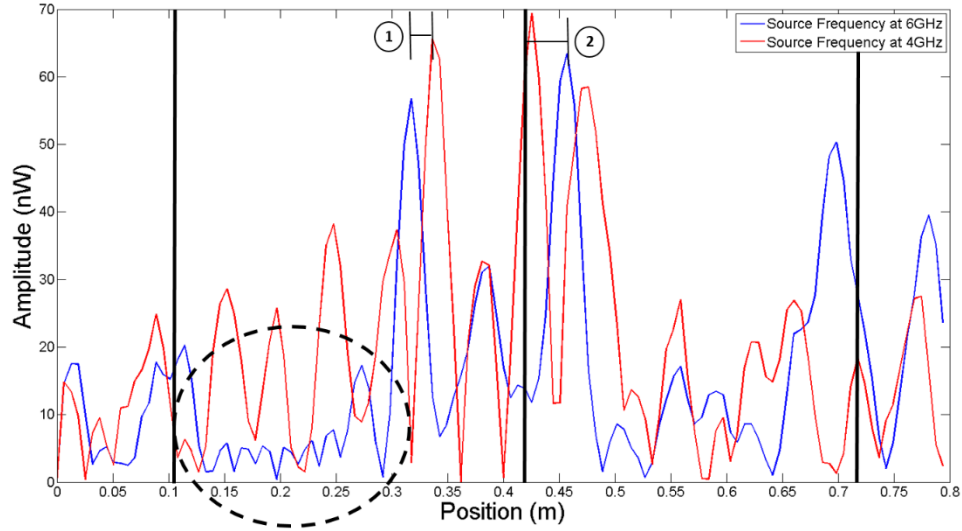


Figure 27: Maximum amplitudes of the reflected signals when the source frequency was varied. At 4GHz the phase offset was at 225 degrees and at 6GHz the phase offset was at 180 degrees. Vertical black lines represent the locations of the antennas and the black dashed oval shows an area of increased resolution. Locations 1 and 2 are shifts between the signals near the receiving antenna.

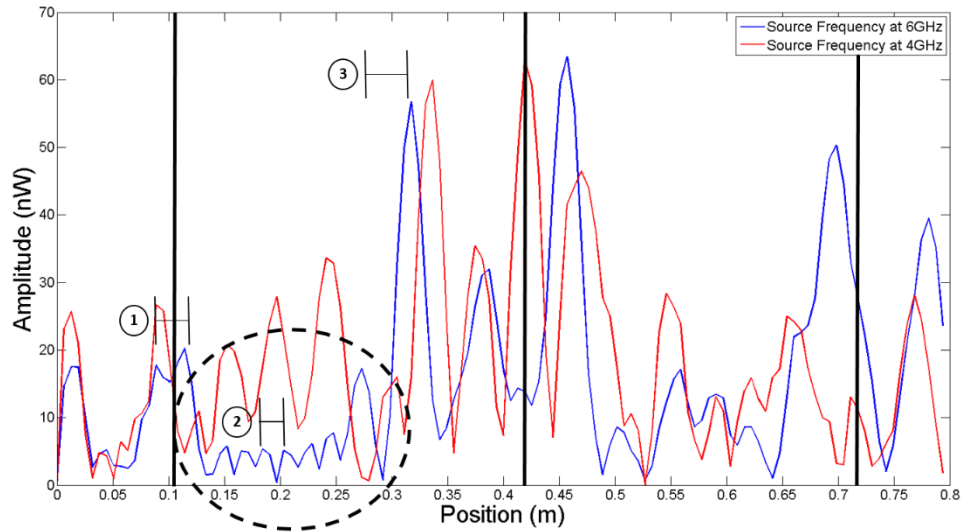


Figure 28: Reflected signals at 180 degree phase offset when the source frequency was varied. Vertical black lines represent the locations of the antennas and the black dashed oval shows an area of increased resolution. Locations 1, 2 and 3 are peak-to-peak distances of the reflected signal at 6GHz.

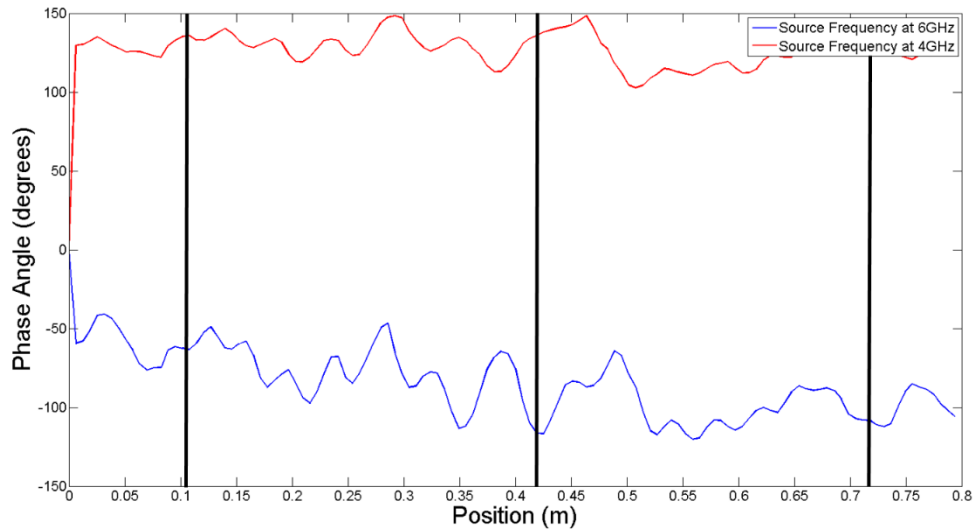


Figure 29: Phase angles of reflected signals at 180 degrees phase offset when the source frequencies were varied. Vertical black lines represent the locations of the antennas.

The data gathered to produce (Figures 27-29) came from Tests 27, 28 and 30. The test parameters are shown in (Table 3) and (Table 4). Looking at (Table 3), we notice that for Tests 27 and 28 the only test parameter that changed was the source frequency. Test 30 was conducted at a 6GHz source frequency with a new A.H. Systems horn antenna as source antenna #2. (Table 3) and (Table 4) are in **Appendix A** and **Appendix B**, respectively.

For (Figures 27-29), the vertical black lines represent the locations of the antennas and the black dashed oval shows an area of increased signal resolution and small amplitude. In (Figure 27), we noticed that the maximum amplitudes of the reflected signals at different source frequencies were almost the same, 69.4nW at 4GHz and 63.49nW at 6GHz. Again,

we noticed the same trend that the amplitude of the reflected signal was greater under the antennas. At a source frequency of 6GHz the difference in amplitude of the return signal under an antenna versus between the antennas was much greater. This observation was observed within the dashed oval in (Figure 27) and (Figure 28). Within the black dashed oval the reflected signal at a source frequency of 6GHz, had a greater amount of peaks at a steady amplitude between 5nW and 6nW. The peaks correspond to a position of the subsurface object where the source signal phase angles added and amplified the reflected signal from the object, while the valleys correspond to locations where the source signals canceled each other. In (Figure 27), it was observed that at 6GHz there were seven peaks between the suspected positions of the source antenna and the receiving antenna, while at 4GHz there were only five peaks. The higher number of peaks even if much smaller in amplitude, mean an increase in the phased-array systems resolution. From radiation lobe simulations of the handmade GIMA antenna and the lobe configurations of the A.H. Systems horn antennas (**Appendix E** and **Appendix F**), we noticed that the lobes change size and shape as the frequency of the antennas were changed. This change in lobe dimension was most likely contributing to why we observed an increased number of uniform looking peaks between the antennas at 6GHz [24, 26]. The decrease in amplitude of these peaks could most likely be attributed to the same power balance issue that was encountered when testing different slab configurations, Section 4.1. Tests 27 and 28 were conducted using antenna orientation # 3, which was believed to increase the overall radiation pattern area of the array and the interactions of the radiation patterns between the antennas. Damage to source antenna #2 altered the radiation pattern of the antenna by most

likely increasing the size of a minor or side lobe. An increase in a minor or side lobe in an undesired direction would indeed cause a change in the antennas radiation pattern, which would directly affect the amplitude and phase of the return signal.

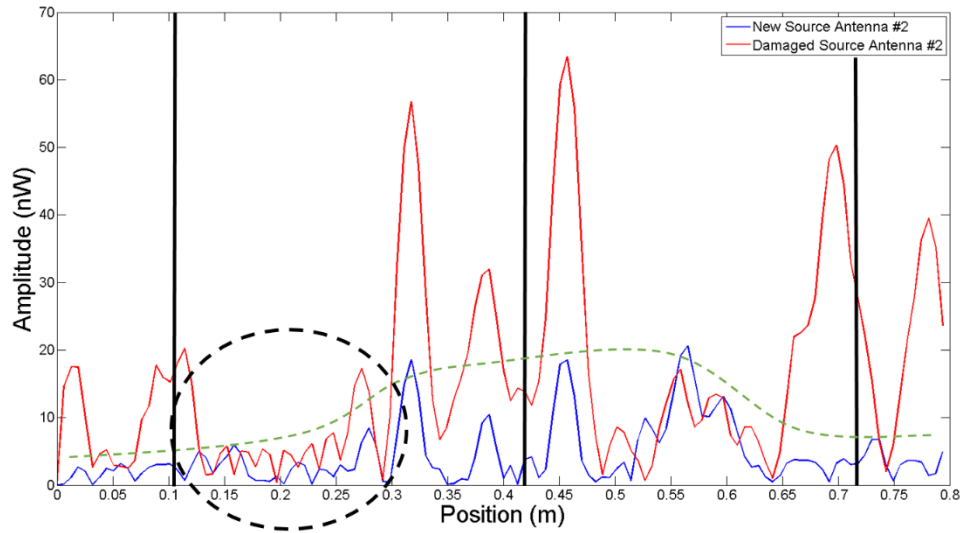


Figure 30: Reflected signals at 180 degree phase offset, at a 6GHz source frequency, when source antenna #2 was changed. Vertical black lines represent the locations of the antennas and the black dashed oval shows an area of increased resolution. The green dashed line represents the approximate envelope of the reflected signal with a new source antenna #2.

When comparing the reflected signals shown in (Figure 30) with the only parameter being varied was the replacement of antenna #2, we noticed an improvement in signal. Within the dashed oval both signals had seven peaks. Replacing the antenna showed the same amount of resolution within the highlighted area, but the peaks were not as uniform. It did however, decrease the amplitudes of the reflected signal under all of the antennas and balanced the power emitted from the source antennas. Symmetry of the reflected signal across the concrete slab was more evident when the antenna was replaced. The signal with the new antenna was not as uniform in the area between source antenna #1 and the receiving

antenna, but across the whole concrete slab the signal was more uniform with less amplitude variations under the antennas. The smoother tapering of the reflected signal with the new antenna, which is shown in (Figure 30) by the green dashed line, informs us that the accuracy, reliability and performance of the array has increased.

By using Equation (4.1) we calculated the wavelength (λ) at 6GHz to be approximately .05m. Looking at (Figure 27), we first noticed that the major peaks that represented the strongest reflected signals under the antennas were slightly shifted. The large peaks at 6GHz were on the outside of the large peaks at 4GHz. The shift at location 1 on (Figure 27) was 0.019m while the shift at location 2 was 0.0381m. This corresponds to approximately $\lambda/2$ at 6GHz and 4GHz. There is a .0191m difference between the two shifts, if that number is divided by 2 the answer becomes 0.00955m. This distance could correspond to a displacement of the phased-array setup between tests. If that distance is added to location 1 and subtracted from location 2, the peak-to-peak distances become 0.02855m which is close to $\lambda/2$ at 6GHz.

We also noticed that at 6GHz the peak-to-peak distance varied as the subsurface object moved across the concrete slab. Under the source antennas the peak-to-peak was approximately .0254m (location 1). Within the black dashed oval the peak-to-peak distance decreased to .019m (location 2). Near the receiving antenna the peak-to-peak increased to 0.0444m, (location 3) which can be seen in (Figure 28).

The shift between the reflected signals when the source frequency is varied, seen in (Figure 27), was due to the change in the antennas radiation pattern when frequency of the signal was varied. When the dimensions of the radiation pattern of the antennas were

altered the interactions between them changed causing deviations in the amplitude and phase angles of the reflected signals. The interactions between the electromagnetic radiation patterns of the antennas could also explain the variance in peak-to-peak distance across the concrete slab.

(Figure 29) shows us the phase angles of the reflected signals as the position of the subsurface object changes. The variation between the phase angles at different source frequencies seem to be minimal, which means that the reflected signals must be stable. At 4GHz the variation in phase angles was 45.6 degrees and at 6GHz the variation in phase angles was 79.45 degrees. The variation between the two frequencies was 33.85 degrees. This shows that as the frequency of the antennas increases the variance between the phase angles also increases. Again it might be the adding and subtracting of multiple signals that is causing the variance in the phase angles. We also noticed that the plots of the phase angles at the different frequencies were shifted in the y direction. This makes sense because as the frequency from the antennas increases the period and the wavelength of the signal decreases, which means that it takes more waves to travel the same distance. This means that signals would arrive at the receiving antenna at a different phase.

4.5. Varying Antenna Orientation

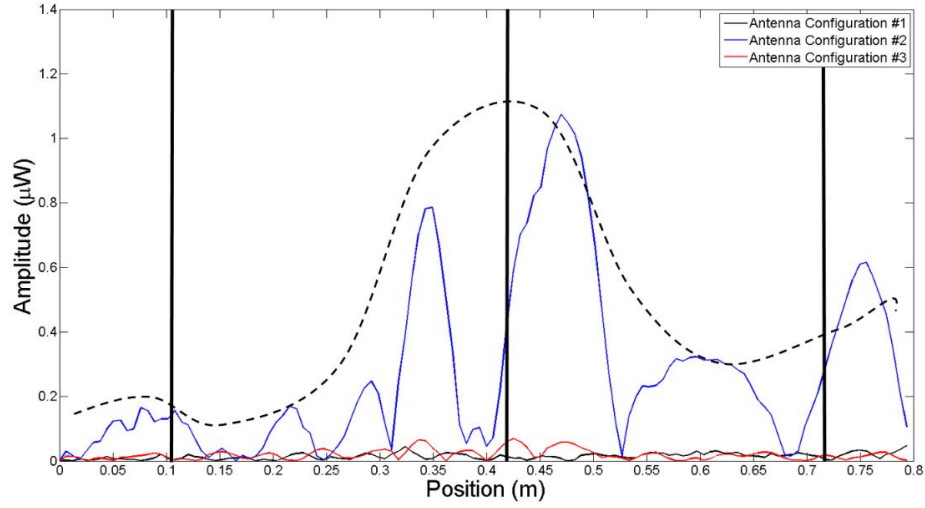


Figure 31: Maximum amplitude reflected signals, when the antenna orientations were varied. For configuration #1 the phase offset was 315 degrees, for configuration #2 the phase offset was 180 degrees and for configuration #3 the phase offset was 225 degrees. Vertical black lines represent the locations of the antennas and the black dashed line shows the approximate shape of the reflected signal envelope for configuration #2.

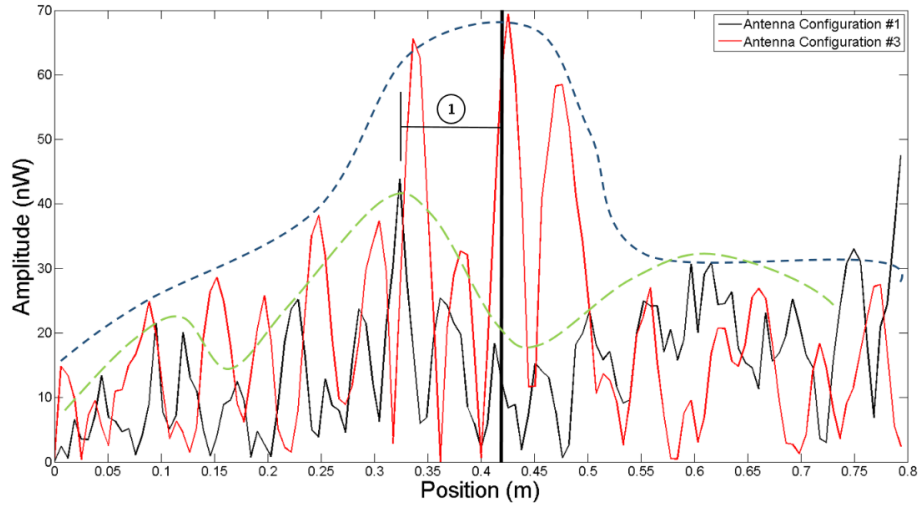


Figure 32: Maximum amplitude reflected signals of configuration #1 and configuration #3. For configuration #1 the phase offset was 315 degrees and for configuration #3 the phase offset was 225 degrees. The center vertical black line represents the location of the receiving antenna. Location 1 shows a shift of .0903m between the two tests. The blue dashed line shows the approximate shape of the reflected signal envelope for configuration #2 and the green dashed line shows the approximate shape of the reflected signal envelope for configuration #1.

The data gathered to produce (Figures 32 and 33) came from Tests 13, 20 and 28. The test parameters are shown in (Table 3) and (Table 4). Looking at (Table 3), we notice that for these three tests the only test parameter that changed was the orientation of the antennas. (Table 3) and (Table 4) are in **Appendix A** and **Appendix B**, respectively.

(Figure 31) shows the reflected signals at maximum amplitude of the three different antenna configurations that were tested. From the figure, it was clear that configuration #2 had the greatest return signal under the receiving antenna, with an amplitude of $1.074\mu\text{W}$. Configuration #1 had an amplitude of 43.86nW and configuration #3 had an amplitude of 69.4nW . We noticed that for configuration #2 that there were two significantly large peaks. One can be seen right under the receiver antenna and another to the left of the large peak. We also noticed that the three peaks to the left of the large peak taper off in an exponential trend from under the source antenna. To the right of the large peak we only see two peaks with the larger of the two being under the source antenna. The asymmetry of the reflected signal occurred from a power balance issue between the source antennas, caused by damage sustained to source antenna #2 which altered the antennas radiation pattern. This was the same phenomenon that occurred in (Figure 21). Further details on the proposed explanation of the result can be found in Section 4.1.

The apparent shape of reflected signal envelope is caused by the interactions between the antennas radiation patterns. The radiation characteristics of antenna arrays can be optimized by selecting the proper phase or amplitude distribution between the antennas, which control the beamwidth and the shape of the side lobes. The type of distribution that describes the radiation pattern of the phased-array governs the efficiency of the system. A

radiation pattern represented by binomial distribution would have a low side lobe levels and a large half-power beamwidth. While a radiation pattern represented by uniform distribution would have a large side lobe levels and a low half-power beamwidth. The reflected signal from the array reaches its optimal levels when a smooth tapering effect between the antennas radiation pattern is observed from the center of the array to the edges. For this to occur the distribution that represents the combined radiation pattern of the array must be somewhere between a binomial and uniform distribution, which would correspond to having both a low side lobe levels and half-power beamwidth [22]. Currently there are no simulated models of the interactions between the radiation patterns of the antennas. The magnitude of the reflected signal and the envelope are indirect indicators of the interaction of the radiation patterns. From the results gathered in (Figure 22) the envelopes of the reflected signal for the two different increment sizes seem to be represented by some sort of binomial distribution. This is due to the large sharp peak under the receiving antenna. For this antenna configuration it can be concluded that an increment size of 0.5" (1.27cm) represents a more optimal array configuration due to the smoother tapering of the envelope, even if the amplitude of the signal is less.

Because the reflected signal from configuration #2 was two orders of magnitude higher than the other configurations it was difficult to see if any particular trends occur. Trends or observations in configurations #1 and #3 can be more easily seen in (Figure 32). Even though the amplitude of the reflected signals were smaller in these two antenna configurations it was clear that more interesting phenomenons were occurring. In (Figure 32), we noticed that the envelopes of the two reflected signals were similar, but shifted.

The shift occurred because the two test were conducted months apart and the antenna position over the concrete slab had changed. The shift was 0.0903m or 3.56in. For both reflected signals the large peaks occurred under the receiver antenna. We noticed that the amplitude was the greatest under the receiver antenna and that it increased and decreased at a faster rate as the subsurface object moved between the receiving and source antennas. The amplitude then increased as the object moved under the source antennas. We also observed an increase in the number of peaks between antennas, with configuration #1 had six major peaks on both sides of the large peak, while configuration #3 had six peaks on the left side of the large peak and four on the right side. An increased number of peaks meant that the system was able to detect the subsurface object clearer at more locations across the concrete slab. This was an increase in the systems resolution.

The increased resolution of the array system was attributed to an optimal interaction between the radiation lodes of the antennas. The distribution that describes the overall radiation pattern of the antenna array governs the performance of the system. The energy from the reflected signal was an indirect measure of the radiation pattern distribution of the array and the same trends should be observed. The apparent distribution for configuration #2 can be approximated by the envelope of the reflected signal, which was represented by the black dashed line in (Figure 31). The envelope for configuration #2 had a shape similar to a binomial distribution, which would mean that the system would have low side lobe levels and a large half-power bandwidth. The asymmetry that occurs under source antenna #2 concludes that the side lode levels were higher on that side of the array system. Less peaks were observed in this antenna configuration, which can be attributed to less

interaction between the radiation patterns of the receiving antenna and the source antennas. Looking at **Appendix F**, we noticed that the radiation pattern was larger in the y-direction than in the x-direction. In this configuration, the larger radiation direction of the A.H. Systems source antennas was interacting with the smaller radiation direction of the GIMA receiving antenna. Less interaction between the antennas lowers the probability of detection and decreases the overall performance of the system. In (Figure 32), the envelopes of the reflected signal for configuration #1 and #3 are represented by the green and blue dashed lines. For these configurations the peaks under the receiving antenna were not as pronounced as in configuration #2. The distributions that describe these signals still had the familiar binomial shape, but the signals had a smoother tapering and in the case of configuration #1, the addition of peaks under the source antennas. The smoother tapering correlates to an increase in the phased-arrays accuracy, reliability and performance [22].

4.6. Antenna Coupling

The directionality, the antenna lobe dimensions and how all the signals interact with each other dictates the amplitude and phase angle of the return signal. If the electromagnetic radiation lobes are represented as straight lines that travel directly to the object and are reflected to the receiving antenna, we would see one of two things. Depending on the position of the object on the concrete slab and the phase offset and angle of the source signals, the reflected signal would be represented as a modified sine wave with uniform peaks and valleys. The peaks and valleys are the result of constructive and destructive interference, where the peaks would have two times the amplitude of the source signal and the valleys would have zero amplitude. The model of the reflected signal would

appear less like a sine wave as the model becomes more complex. The signal becomes more complex when electromagnetic radiation is modeled as three dimensional lobes that radiate out of the antennas with different shapes and sizes. The peaks of the reflected signal would vary in amplitude as the position of the object changes. The signal gets more distorted when antenna coupling or cross talk is introduced. Coupling occurs when the source and receiving antennas are near each other and side lobes from the source antennas interact directly with the receiving antenna. Identifying and subtracting out the coupling would amplify the reflected signal from the subsurface object. The interactions of all these signals are shown in (Figure 33).

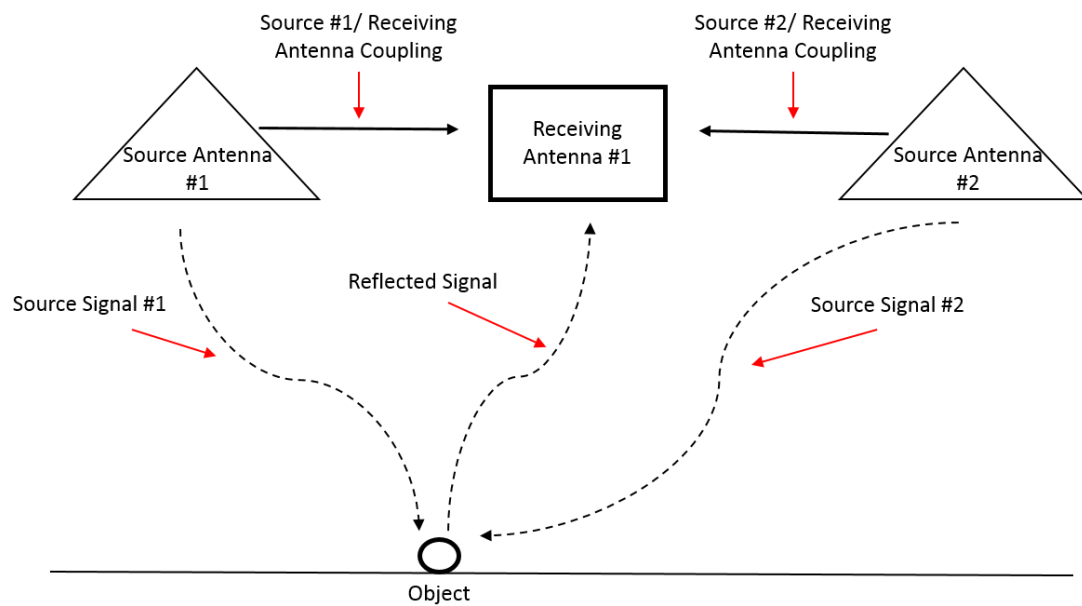


Figure 33: Diagram of multiple signals that the receiving antenna might see

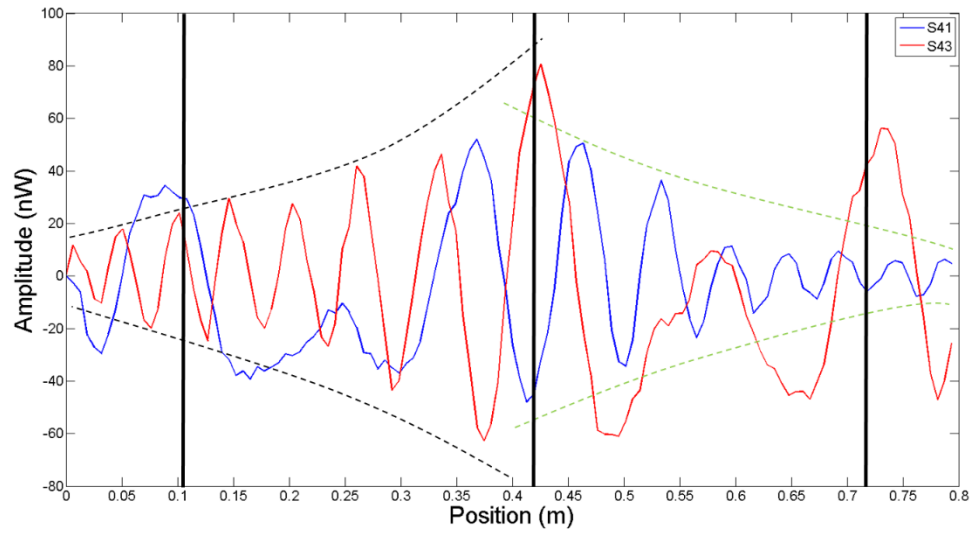


Figure 34: Comparisons of S41 and S43 tests

The results of an S41 and an S43 test are observed in (Figure 34). From Sections 3.1.2 and 3.2.3, we remember that source antenna #1 was connected to Port 1 on the Network Analyzer, source antenna #2 was connected to Port 3 on the Network Analyzer and the receiving antenna was connected to Port 4 on the Network Analyzer. (Figure 34) was constructed using data gathered from Test 29. Referring back to (Figure 13) we see that the two source antennas were located at two different sides of the concrete slab.

The solid blue and red lines on the plot correspond to the reflected signals of an S41 and an S43 test, respectively. The vertical solid black lines represent where the antennas were located across the concrete slab. During the S41 test, the distance that the emitted signal and the reflected signal had to travel was less at position 1 of the position rig then at position 125. Inversely, during the S43 test, the distance that the emitted signal and the reflected signal had to travel was less at position 125 of the position rig then at

position 1. At position 1 for an S41 test and at position 125 for an S43 test more electromagnetic energy reached the receiving antenna because it was less likely to be dissipated by the surroundings, which resulted in an increase in the reflected signal strength. This result was observed in (Figure 34). Only looking at the reflected signal from the S41 test it was evident that the amplitude of the signal was lower when the object was at the end of the concrete slab (.8m), which corresponded to position 125, than when the object was at the start of the concrete slab at position 1. This was inversely true for the S43 test. The observed tapering or envelopes of the reflected signal strength was represented by the green and black dashed lines for the S41 and S43 tests, respectively. The amplitude of the signal was the largest right under the receiving antenna, which again was attributed to the interaction between the antenna radiation patterns.

Referring to (Figure 34), the S41 test produced destructive interference and the S43 test produced constructive interference at the location right beneath the GIMA receiving antenna. This observation informed us that the emitted signals from the source antennas were 180 degrees out of phase. Looking back at (Figure 12), the cable connectors on the two source antennas were both pointing away from each other. Each connector was connected to one ridge of the antenna, the other was connected to ground. Electromagnetic radiation is first emitted from the ridge that the connector is connected to, referred to as the emitting plane. The reason for the 180 degree phase shift between the two tests is because the emitting planes for these tests were opposite from each other. Turning one of the source antennas 180 degrees would position the cable connectors in the same direction and have

the emitting planes in the same orientation. This would put the S41 and the S43 reflected signals in phase.

The oscillations observed in the S41 and S43 tests arose from constructive and destructive interference from a secondary signal. For an ideal S41 send and receive test, the only signal that the receiver would detect would be the reflected signal from the subsurface object. With no other signal interfering with the reflected signal, the S41 test would produce a reflected signal that appears like the envelopes pictured in (Figure 34). No oscillations should occur.

Mutual coupling, or a secondary signal emitted from minor or side lobes of the source antennas was most likely interfering with the reflected signal and causing the oscillations observed in (Figure 34). The extent of the mutual coupling for the S41 and S43 tests were found by emitting the signals into the far-field and observing a change in the signal when a reflective object was slowly moved into the range of the array system. This test (Test 33) was conducted outside of our lab and the antennas were beamed upwards toward the sky. The setup for this test was similar to the one pictured in (Figure 13) with the only difference being that the structural beam holding the antennas was rotated 180 degrees. The phased-array system detected the reflective object at a distance of 7ft (2.14m). When the object was further than 7ft (2.14m) or was absent, the signal obtained by the receiving antenna was purely due to mutual coupling between the antennas. It is possible that the receiving antenna might have detected some small external signal from the environment, but the magnitude of that signal would be small compared to the magnitude of the coupling signal. The extent of the mutual coupling for an S43 test was observed in

(Figure 35). Slight differences were observed between the results from the S41 and S43 tests. From the figure, we ascertained that a coupling signal exists, which is represented by the solid blue line in (Figure 35). The signals from the coupling and when a reflective object was 7ft (2.14m) away are superimposed on top of each other up until 4GHz. That corresponds to the area of operation for the phased-array system. The minimal variation between the signals, which can be seen within the black dashed oval, informs us that 7ft (2.14m) was the range at which the antennas used in the phased-array radar system can detect a reflective object. When the reflective object was lowered to 4ft (1.22m), a clear increase in the amplitude of the reflected signal was detected. The difference between the mutual coupling signal and the signal when the object was at 4ft (1.22m) was approximately 10dBm or 10mW, which corresponds to the magnitude of the reflected signal. By knowing the extent of the mutual coupling between the antennas it would be possible to create mathematical models of the reflected signal and subtract out the coupling to enhance the signal from the reflective object.

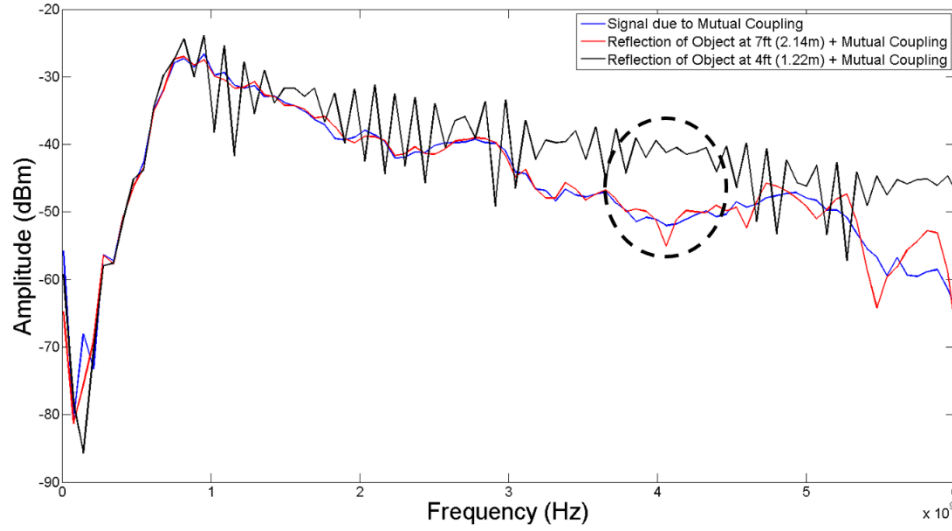


Figure 35: Comparisons of an S43 test to identify the extent of mutual coupling between the source and receiving antennas throughout a range of frequencies. Solid blue line represents the signal due to mutual coupling, the solid red line represents a signal with mutual coupling and a reflected signal from an object 7ft (2.14m) away and the solid black line represents a signal with mutual coupling and a reflected signal from an object 4ft (1.22m) away.

Mutual coupling can be decreased by increasing the distance between the antennas, shielding the source antenna or decreasing the side lobes of the antennas by altering some of the antenna parameters. Because mutual coupling exists in the phased-array radar system, it is possible that differences between the theoretical reflected model and the laboratory experiments could be explained by adding coupling terms to the theoretical model. This would mean that the model based on Equation (2.22) would have four terms instead of two. An equation which included mutual coupling terms from both source antenna #1 and #2 would resemble Equation (4.2).

$$E = e^{(j2\pi ft)}(A_1 e^{-j\beta_1} + A_2 e^{-j\beta_2} + A_3 e^{-j\beta_3} + A_4 e^{-j\beta_4}) \quad (4.2)$$

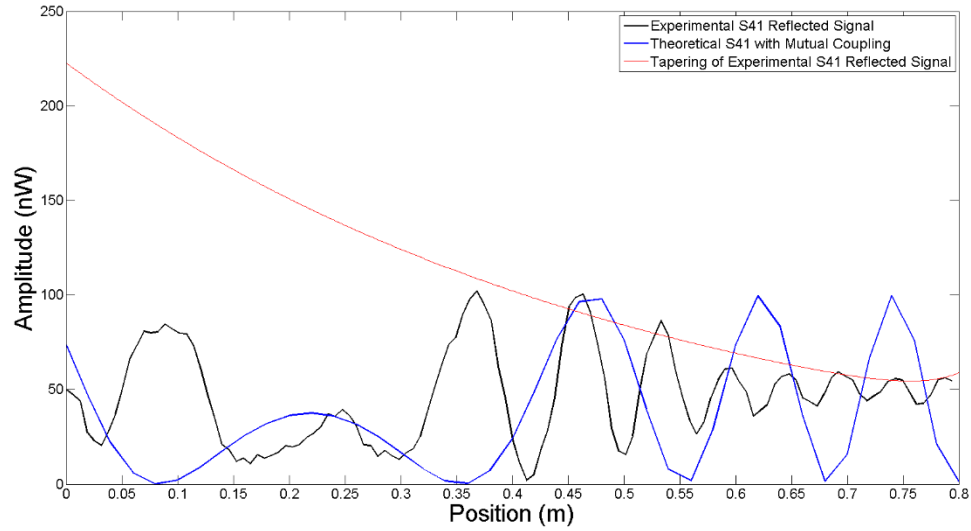


Figure 36: Comparison of an experimental S41 test (solid black line) with a theoretical mathematical model representing an S41 test with coupling (solid blue line). The solid red line represents the tapering of the experimental data as the reflective object moves beyond the radiation pattern of the antennas.

Understanding how mutual coupling affects a reflected signal would eventually lead to increasing the performance of the phased-array radar system. (Figure 36) depicts the comparison between experimental data of a reflected signal from an S41 test and a theoretical mathematical representation of a reflected signal from an S41 test with mutual coupling. To create the mathematical representation of the reflected signal, Equations (2.29) and (2.31) were modified. In this model the second electromagnetic field equation pertained to a side lobe emanating from source antenna #1 and not a signal from source antenna #2. The source signal direction r_2 became equal to $d/2$ to represent a side lobe emanating from source antenna #1 at a phase angle of 180 degrees traveling directly into the receiving antenna.

From (Figure 36) can be ascertained that the theoretical representation of the S41 reflected signal with mutual coupling roughly follows the same trend outlined by the experimental data. What is clearly observed is that the model does not incorporate the tapering effect that occurs in the experimental data as the reflective object moves beyond the radiation pattern of the antennas. The tapering effect of the experimental data was found to be exponential with a .88 coefficient of determination. For simplicity the theoretical model was based on far-field approximations. The tapering observed in the experimental data could be modeled by incorporating near-field (Fresnal) approximations [27].

Mutual coupling between the antennas alters the overall radiation of the array. The physical optics (PO) technique, which combines the dyadic Green's function with the electric field reaction, makes it possible to calculate the mutual impedance between the antennas [17]. The antenna arrays overall performance does not only depend on the performance of one array element, but on how the radiating patterns interact with one another. The amount of coupling between antennas primarily depends on the radiation characteristics of each antenna, the distance between the antennas and the relative orientation of each antenna. Radiated energy from one antenna might reach another due to some non-ideal directional characteristics of the antenna. Mutual coupling complicates the analysis and the design of the array because it is difficult to model. Mutual coupling effects in an array cannot be generalized. This is due to the fact that many antenna parameters can influence that amount of mutual coupling within a system. The mutual coupling effect on the performance of the antenna array depends on: the type of antennas being used and its design parameters, the relative position of the antenna elements to one another, the feed

points of each antenna and the scan volume of the antenna array. The parameters listed above alter the impedance of each array element, the reflection coefficients and the overall antenna field pattern. All of these parameters will influence the overall performance of the antenna array [18].

CONCLUSION

This study outlined the theory and methodology required to begin determining the performance, accuracy and reliability of a near-field, air-coupled, phased-array radar system. Changes in the reflected signals were observed and recorded when certain array parameters were varied such as the: slab configurations, increment size, antenna height, source frequencies and antenna orientation. The results from numerous tests gave us an understanding of how variations to certain parameters influenced the performance of the phased-array radar system in the near-field. The accuracy, reliability and performance of the phased-array system as a whole can be further increased by optimizing certain antenna parameters and understanding the interactions that occur between signals.

Throughout the tests conducted in Chapter 4 many interesting phenomenons occurred as certain test parameters were varied. From the results we can only speculate the meaning of the variations that occurred. Further studies would have to be conducted to completely understand all of the phenomenons that were observed during these experiments.

The shape of the arrays radiation pattern could only be indirectly observed by creating an envelope of the reflected signals. The distribution fit to the radiation pattern dictates the overall performance of the system. Different envelope shapes were observed when certain test parameters were changed. When the increment size was varied, it was observed that smoother tapering occurred at an increment size of 0.5" (1.27cm) using antenna configuration #1. The same reflected signal also showed a smooth taper when the antenna orientations were varied, but the signal using configuration #3 was slightly

smoother. The envelopes were only a rough indication of the systems performance under certain tests. The most efficient method to optimize the performance of the phased-array radar system would be to mathematically model the radiation pattern of the array using electromagnetic wave or antenna modeling software like ANSYS HFSS. The software would simulate the interactions between the major, minor and side lobes of the antennas. From the lobe interactions, it would then be possible to fit a distribution to the radiation pattern of the array and accurately determine the performance of the system. The optimal performance of the system could be found by changing certain antenna parameters within the model, altering the dimensions of the radiation pattern and fitting a distribution to the radiation pattern.

The software could accurately determine the reason for the power balance issues that occurred in the slab configuration tests, but was also evident throughout all of the tests by the asymmetry of the reflected signal under source antenna #1 and #2. If all of the antenna parameters are known for the A.H. Systems double ridge horn antennas and for the home-made GIMA antenna, an ideal representation of the arrays radiation pattern could be determined. The lobe configurations of one of the A.H. Systems antennas could be altered to simulate the damage that it sustained. Comparing this model to the experimental data would definitively determine if the damage sustained by the antenna was causing the asymmetry, the amplitude decrease between the antennas when the source frequencies were varied, or the amplitude increase under the receiving antenna when the height of antennas was increased to 26" (66.04cm).

The addition of near-field (Fresnel) approximations and accurately calculating the attenuation of the phased-array system through air and other media could validate certain observations that occurred. A better understanding of the complexities that occur in the near-field and the implementation of the near-field electromagnetic radiation interaction formulas could explain the increase of secondary peaks as the increment size of the subsurface object is decreased. The penetration depth of the phased-array system could be determined by accurately calculating the attenuation of the system. The penetration depth range could then be optimized by altering certain array parameters.

Increasing the strength of the electromagnetic signal from the subsurface object ultimately ensures an increase in the array systems performance. The accuracy and reliability of the system is dependent on separating out the specific reflective signal from a subsurface object from multiple signals that the receiving antenna might receive. Signals that interfere with the reflected signal might include: mutual coupling or cross talk from minor or side lobes, scattered radiation and noise from the surroundings.

There are certain unwanted signals that can be controlled or minimized, like the amount of mutual coupling. Coupling can be minimized by increasing the distance between the antennas and decreasing the size of minor and side lobes. Conducting further experimental tests isolating the extent of mutual coupling between the antennas could yield enough information to create an accurate mathematical representation of the coupling. If an accurate model of the coupling could be achieved it would then be possible to subtract the coupling signal from the signal received from the receiving antenna, leaving only the reflected signal and noise from the environment.

Noise from the surroundings can be difficult to predict and separate from a reflected signal. During these tests conducted at the University of Vermont, noise from the surroundings could be due to electromagnetic waves emitted from equipment at Fletcher Allen Hospital, UVM Wi-Fi, cellphones and signals from other electronic equipment within the lab. During the experimental tests, unwanted background noise was decreased by recording the reflected signal of the concrete slab and subtracting it from the reflected signal with the subsurface object. This was a simple way to enhance the signal from the subsurface object. In the future, subtracting of background noise would have to be conducted using other forms of data processing because noise cannot be approximated by a constant. Utilizing certain filters and noise reduction techniques during data processing could properly isolate and enhance the reflected signal of subsurface objects. To properly estimate the performance, accuracy and reliability of the air-coupled near-field phased-array radar system the probability of detection (POD) must be performed on the system.

The (POD) is the probability of detecting an object exceeding a threshold derived from a signal-to-noise ratio, which is unique to each radar system. Noise can be modeled as Rayleigh or Gaussian depending on the particular circumstance. When plotting the reflected signal of a radar system against white noise, a Gaussian distribution is used to simulate the noise. The threshold can be determined from the allowable signal-to-noise ratio and the (POD) can then be determined by the area under the curve that exceeds the threshold.

To calculate the (POD) hypothesis testing is used with the option of two possible true statements. One possibility is that the null hypothesis (H_0) holds true, meaning that the

measurement is only a result of interference or noise. The second possibility is the alternative hypothesis (H_1) is true, which states that the measurement is a combination of interference and reflections from the desired object. The test will determine which hypothesis best fits the data. Probability density functions (pdf's) of the two hypotheses, Equations (5.1) and (5.2), would be used to find the POD, which can be seen in Equation (5.3). Where x is a vector of sample data [23].

$$p_x(x|H_o) = \text{The pdf of } x \text{ when the object is not present} \quad (5.1)$$

$$p_x(x|H_1) = \text{The pdf of } x \text{ when the object is present} \quad (5.2)$$

$$\text{POD: } P_d = \int p_x(x|H_1)dx \quad (5.3)$$

Calculating the (POD) of the phased-array radar system would give us a better understanding of the systems performance. Results from calculating the (POD) of the system when certain parameter are changed could validate the results gathered from certain experimental tests.

Once a better understanding of the electromagnetic wave interactions for the air-coupled near-field phased-array radar system is achieved, the next step would be to see if the system can detect other subsurface phenomenons. This may include: changes in the concretes dielectric properties (which may include increased levels of moisture or aggressive agents), small cracks, delaminations or even the corrosion. Corrosion might be detectable by determining if the reflected signal is non-linear. It is believed that corrosion scatters electromagnetic radiation non-linearly and detecting harmonics within a reflected

signal might signify the presence of corrosion. In the near future when the performance, accuracy and reliability of the phased-array system is proven for the detection of delamination, voids, cracks, corrosion and subsurface objects this system could be incorporated into GPR unit to monitor bridge decks and roadways.

REFERENCES

- [1] Hughes, Mark E., and Carl R. Bischof. "Corrosion of Steel in Concrete." *Concrete Repair Manual*. 4th ed. Vol. 1. [Farmington Hills, MI]: American Concrete Institute, 2013. 387-578. Print.
- [2] Broomfield, John P. "Corrosion of Steel on Concrete." *Corrosion of Steel in Concrete: Understanding, Investigation, and Repair*. London: E & FN Spon, 1997. Print.
- [3] Nickel, Ulrich. "Fundamentals of Signal Processing for Phased Array Radar." *Advanced Radar Signal and Data Processing Le Traitement Avancé Du Signal Et Des Données Radar*. Neuilly-sur-Seine Cedex, France: North Atlantic Treaty Organization, Research and Technology Organization, 2006. 1-21. Print.
- [4] *Agilent PNA Series Network Analyzer Printed Version of PNA Help User's and Programming Guide*. N.p.: Agilent Technologies, 15 May 2013. PDF.
- [5] *Service Guide N5241A (10 MHz–13.5 GHz) and N5242A (10 MHz–26.5 GHz) Agilent Technologies 2-Port and 4-Port PNA-X Microwave Network Analyzers*. N.p.: Agilent Technologies, Apr. 2009. PDF.
- [6] *2011 Report Card for Vermont's Infrastructure*. N.p.: American Society of Civil Engineers, 2011. PDF.
- [7] *Vermont Agency of Transportation Program Development – Structures Section 2013 Annual Report*. N.p.: Vermont Agency of Transportation, 2013. PDF.
- [8] "History of Ground Penetrating Radar Technology." *Ingenieurbüro Obonic*. Ingenieurbüro Obonic, 2008. Web. 20 Mar. 2014.
- [9] Huston, Dryver, Peter Fuhr, Ken Maser, and William Weedon. *NONDESTRUCTIVE TESTING OF REINFORCED CONCRETE BRIDGES USING RADAR IMAGING TECHNIQUES*. N.p.: n.p., 1 July 2002. PDF
- [10] Adam, Christopher S. *Ground Penetrating Radar for Non-Destructive Evaluation of Concrete Bridge Decks*. Thesis. University of Vermont, 1997. Burlington: University of Vermont, 1997. Print.
- [11] Balanis, Constantine A. "Time-Varying and Time-Harmonic Electromagnetic Fields." *Advanced Engineering Electromagnetics*. New York: Wiley, 1989. 1-41. Print.
- [12] Hernandez, Eric M. "Reliability of Components in Series." CE-395 Safety and Reliability of Engineering Systems. University of Vermont, Burlington. 21 Mar. 2014. Lecture
- [13] Hernandez, Eric M. "Reliability of Components in Parallel." CE-395 Safety and Reliability of Engineering Systems. University of Vermont, Burlington. 21 Mar. 2014. Lecture
- [14] Balanis, Constantine A. "Scattering." *Advanced Engineering Electromagnetics*. New York: Wiley, 1989. 570-669. Print.
- [15] Balanis, Constantine A. "Auxiliary Vector Potentials, Construction of Solutions, and Radiation Scattering Equations." *Advanced Engineering Electromagnetics*. New York: Wiley, 1989. 254-309. Print.

- [16] Balanis, Constantine A. "Fundamental Parameters of Antennas." *Antenna Theory: Analysis and Design*. New York: Wiley, 1997. 28-115. Print.
- [17] Diaz, Leo, and Thomas A. Milligan. "Arrays and Small Antenna Elements." *Antenna Engineering Using Physical Optics: Practical CAD Techniques and Software*. Boston: Artech House, 1996. 53-103. Print.
- [18] Balanis, Constantine A. "Mutual Coupling in Arrays." *Antenna Theory: Analysis and Design*. New York: Wiley, 1997. 422-440. Print.
- [20] Balanis, Constantine A. "Two-Element Arrays." *Antenna Theory: Analysis and Design*. New York: Wiley, 1997. 250-257. Print.
- [21] Balanis, Constantine A. "Phased (Scanning) Arrays." *Antenna Theory: Analysis and Design*. New York: Wiley, 1997. 266-271. Print.
- [22] Balanis, Constantine A. "Design Considerations." *Antenna Theory: Analysis and Design*. New York: Wiley, 1997. 321-324. Print.
- [23] Scheer, Jim, and J. L. Kurtz. "Detection Fundamentals." *Coherent Radar Performance Estimation*. Boston: Artech House, 1993. 295-346. Print.
- [24] "A.H. Systems - Double Ridge Guide Horn Antenna." *A.H. Systems - Double Ridge Guide Horn Antenna*. A.H. Systems, Inc, n.d. Web. 03 Apr. 2014
- [25] Leucci, Giovanni. "Ground Penetrating Radar: The Electromagnetic Signal Attenuation and Maximum Penetration Depth." *Scholarly Research Exchange* 2008 (2008): 1-7. Print.
- [26] Ahmed, Amr. *Design and Optimization of UWB Antenna for Air Coupled GPR Applications*. Thesis. University of Vermont, 2014. Burlington: University of Vermont, 2014. Print.
- [27] Balanis, Constantine A. "Radiating Near-Field (Fresnal) Region." *Antenna Theory: Analysis and Design*. New York: Wiley, 1997. 149-150. Print.
- [28] Hu, Jing Qiong. *Good Impedance Match Antenna (GIMA) Design and Its Applications for Ground Penetrating Radar in Concrete Structures NDE Applications*. Thesis. University of Vermont, 2000. Burlington: University of Vermont, 2000. Print.

APPENDIX A: TABLE OF EXPERIMENTS

Table 3: List Tests

Test Number	Subsurface Object	Slab Configuration	Increment Size	Source Frequency	Antenna Configuration	Antenna Height
1	Bar	#3 (On Eccosorb)	3" (7.62cm)	2GHz	#1	19.5" (49.53cm)
2	Bar	#3 (On Eccosorb)	3" (7.62cm)	3GHz	#1	19.5" (49.53cm)
3	Bar	#3 (On Eccosorb)	3" (7.62cm)	4GHz	#1	19.5" (49.53cm)
4a	Bar	#1	3" (7.62cm)	4GHz	#1	26" (66.04cm)
4b	Rod	#1	3" (7.62cm)	4GHz	#1	26" (66.04cm)
5a	Bar	#2	3" (7.62cm)	4GHz	#1	26" (66.04cm)
5b	Rod	#2	3" (7.62cm)	4GHz	#1	26" (66.04cm)
6 ¹	Bar	#2	3" (7.62cm)	4GHz	#1	26" (66.04cm)
7	Bar	#2	3" (7.62cm)	4GHz	#1	26" (66.04cm)
8	Bar	#2	3" (7.62cm)	4GHz	#1	26" (66.04cm)
9	Bar	#2	3" (7.62cm)	4GHz	#1	26" (66.04cm)
10	Rod	#3	.5" (1.27cm)	4GHz	#1	26" (66.04cm)
11	Rod	#3	.5" (1.27cm)	4GHz	#1	26" (66.04cm)
12	Rod	#3	.5" (1.27cm)	6GHz	#1	26" (66.04cm)
13	Rod	#3	.25" (.635cm)	4GHz	#1	26" (66.04cm)
14	Rod	#3	.25" (.635cm)	6GHz	#1	26" (66.04cm)

15	Rod	#3	.25" (.635cm)	4GHz	#1	26" (66.04cm)
16	Eccosorb/ Metal Sheet	#3	N/A	4GHz	#1	26" (66.04cm)
17	Eccosorb/ Metal Sheet	#3	N/A	6GHz	#1	26" (66.04cm)
18	Eccosorb/ Metal Sheet	#3	N/A	8GHz	#1	26" (66.04cm)
19 ²	Eccosorb/ Metal Sheet	#3	N/A	4GHz, 6GHz, 8GHz	#1	26" (66.04cm)
20	Rod	#3	.25" (.635cm)	4GHz	#2	26" (66.04cm)
21	Rod	#3	.25" (.635cm)	6GHz	#2	26" (66.04cm)
22	Rod	#3	.25" (.635cm)	4GHz	#2	19.5" (49.53cm)
23	Rod	#3	.25" (.635cm)	6GHz	#2	19.5" (49.53cm)
24	Rod	#3	.25" (.635cm)	4GHz	#3	19.5" (49.53cm)
25	Rod	#3	.25" (.635cm)	4GHz	#3	19.5" (49.53cm)
26 ²	Rod	#3	.25" (.635cm)	4GHz	#3	19.5" (49.53cm)
27	Rod	#3	.25" (.635cm)	6GHz	#3	19.5" (49.53cm)
28	Rod	#3	.25" (.635cm)	4GHz	#3	26" (66.04cm)
29 ²	Rod	#3	.25" (.635cm)	4GHz	#3	19.5" (49.53cm)
30 ^o	Rod	#3	.25" (.635cm)	6GHz	#3	19.5" (49.53cm)
31 ^{o,2,3}	Concrete Slab/Metal Sheet	#3	N/A	4GHz, 6GHz, Frequency Sweep	#3	19.5" (49.53cm), 55.5" (140.97cm)
32 ^{o,3}	Rod	#3	.25" (.635cm)	6GHz	#3	19.5" (49.53cm)

33°, ²	Metal Sheet	N/A	N/A	4GHz, 6GHz, Frequency Sweep	#3	Into air, 4ft (1.22m), 7ft (2.14m)
-------------------	-------------	-----	-----	-----------------------------------	----	--

[°] - New A.H. Systems double ridge horn antenna (SAS-571)

¹ - Test has same parameters as Test 5a only that Port 1 and Port 3 are switch to see if ports are causing power balance.

² - S41 and S43 tests

³ - Cable connectors are all in the same direction. In all other test the cable connectors were facing away from the receiving antenna.

APPENDIX B: TABLE OF PORT POWERS

Table 4: List of Port Power for Each Test

Test Numbers	Power to Port 1	Power to Port 3	Power to Port 4
1-6	7dB	7dB	7dB
7	0dB	7dB	7dB
8-24	-2dB	5dB	-5dB
25	-2dB	-2dB	-5dB
26	-2dB	-5dB	-2dB
27, 28, 30, 32	-2dB	-2dB	-5dB
29, 31, 33	-5dB	-5dB	-5dB

Power to ports changed to accommodate an apparent amplitude difference in the reflected signals under the source antennas.

APPENDIX C: INSTRUCTIONS FOR NETWORK ANALYZER SOFTWARE SETUP

Appendix.C.1: Cable Calibration

The Mini-Circuits coaxial cables used in the phased-array radar system were calibrated by using Agilent's own electronic calibration module. Both these components can be seen in (Figure 12) and further information can be found in (Table 2). After opening the Agilent Network Analyzer software on the Agilent PNA-X Network Analyzer the following steps were taken to properly calibrate the coaxial cables.

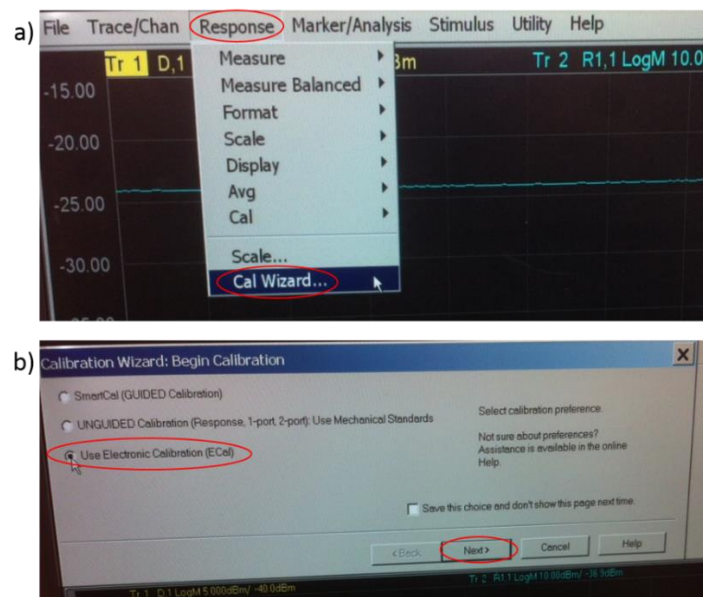


Figure C.1: Calibrating cables with electronic calibration module. (a) Finding the Cal Wizard and (b) choosing the ECal option.

(Figure C.1) shows how to use the network analyzer software to select the proper method to calibrate the cables. The options that need to be clicked on are displayed on the figure as red outlined ovals. (Figure C.1a) illustrates the proper way to arrive to the

calibration wizard window. First click on the **Response** tap which is located on the top toolbar that is located on the top of the screen. Scroll down and click on the **Cal Wizard** option. The calibration wizard window will immediately pop up, which will display the possible calibrating options. Following the red ovals in (Figure C.1b) we check off the **ECal** option and click **Next**. The software will then proceed to calibrate the cables the user might need to follow some further instructions on preceding windows. The cables can be calibrated using the other options that are presented on the calibration wizard. If the user prefers he or she may use the other methods of calibration. Using the ECal method is the easiest and quickest way to calibrate the cables.

Depending on the type of electronic calibrating module, it is possible to calibrate multiple cables at once. Once all the cables are calibrated, the following step is to assign the calibrated cables to the desired network analyzer channels. Traces are particular measured data points that can be displayed on the screen. A single channel can display many traces, but all traces that are assigned to that channel share the same channel settings. For our test we want all of the calibrated cables to be assigned to one channel. (Figure C.2) shows how to check if all of the calibrated cables are assigned to the same channel. This can be verified in the calibration selection window. To arrive at the calibration selection window click on the **Response** tap again, scroll down to the **Cal** option and then over to the **Manage Cals** option to lastly click on the **Cal Sec...** option. This will open the calibration selection window. To the left of the red arrow in (Figure C.2b) and below where it says Cal Type/Ports we can see that all of the calibrations are assigned to the same channel. [4].

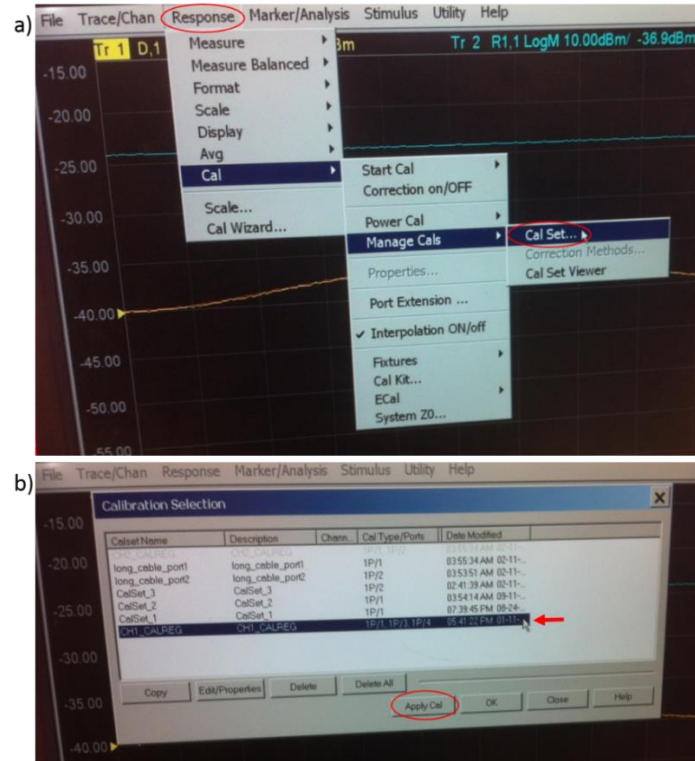


Figure C.2: Making sure calibrated cables are under the right channel

Appendix.C.2: Assigning Antenna Power

Following the instructions that are displayed in (Figure C.3) it is possible to assign the amount of power to each of the ports on the network analyzer. (Figure C.3a) outlines the necessary steps to arrive at the power and attenuators window. On the top toolbar or the home screen click on the tab that says **Stimulus**, scroll down to **Power** and then select **Power and Attenuators....** Immediately after selecting this option the power and attenuators window will appear, which is shown in (Figure C.3b). The table on the window makes it possible for the user to change the state, port power, source attenuation and the leveling modes of each port on the network analyzer. In the phased-array system experiments we only varied the port power. The ports used in the experiments are

numbered 1-3 in (Figure C.3b). For most of the experiments we left port 4 at the default setting of -5dBm and changed port 1 to -2dBm. The power given to each port for different experiments is listed in (Table 4). We varied the power on port 3 from -2dBm to 5dBm because some initial plots showed an amplitude different in the reflected signal when the subsurface object was under source antenna #1 and then under source antenna #2. We attribute this variance in amplitude as a power balance issue possible due to inconsistencies in the cables or antennas or even in the network analyzer. Most likely from the cables or antennas because one of the A.H. Systems horn antennas was damaged during transportation. When manual calibrations were done on the Mini-Circuits cables using HP 85033D 3.5mm calibration kit we noticed that there were some inconsistencies when the calibration data was compared with calibration data directly from Mini-Circuits. Agilent's service guide was used to properly conduct these calibration tests with the HP calibration kit [4, 5].

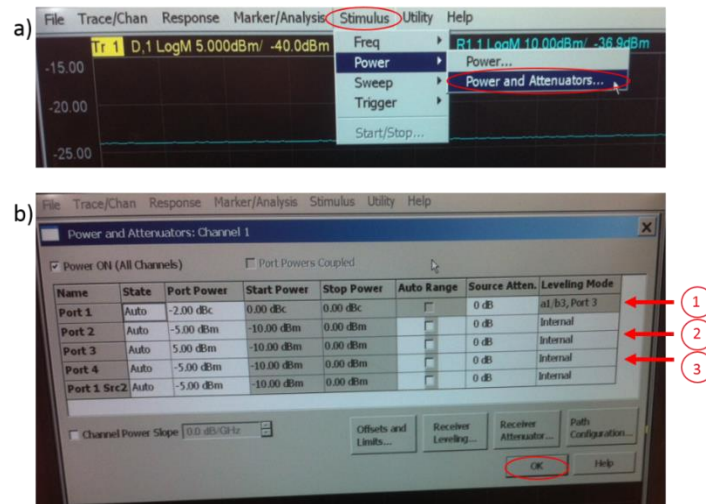


Figure C.3: Assigning power to network analyzer ports

Appendix.C.3: Phase Sweep Function

The Agilent PNA-X Network Analyzer has the ability to sweep the phase of one or more sources relative to another source. This feature on the network analyzer allows us to electronically direct the electromagnetic radiation emitted from the source antennas in the desired direction to continuously sweep the concrete slab for subsurface objects. The mechanics of the phase sweep that is incorporated in all phased-array system is explained further in Section 2.5. Some preliminary steps must first be completed before initiating the phase sweep feature on the network analyzer.

First we must create a new trace to view and record data from a phase sweep test. This can be done by following the steps outlined in (Figure C.4) by the solid red ovals and arrows. (Figure C.4a) shows how to open a new trace in the Agilent network analyzer software. This is done by clicking on the **Trace/Chan** tab on the toolbar on the top of the home screen. The new trace window shown in (Figure C.4b) is accessed by then scrolling down the **Trace** and then over to **New Trace**. On the new trace window click on the **Receivers** tab to setup the source and receiver ports on the network analyzer. Letters A-D corresponds to ports 1-4 being receiver ports, while R1-R4 corresponds to ports 1-4 being source ports. For our phased-array system we have a receiving antenna connected to port 4 of the network analyzer and source antennas connected to ports 1 and 3. This configuration can be programmed into the network analyzer software by activating numerators D, R1 and R3, which are highlighted in (Figure C.4b) as numbers 1-3 next to the red arrows.

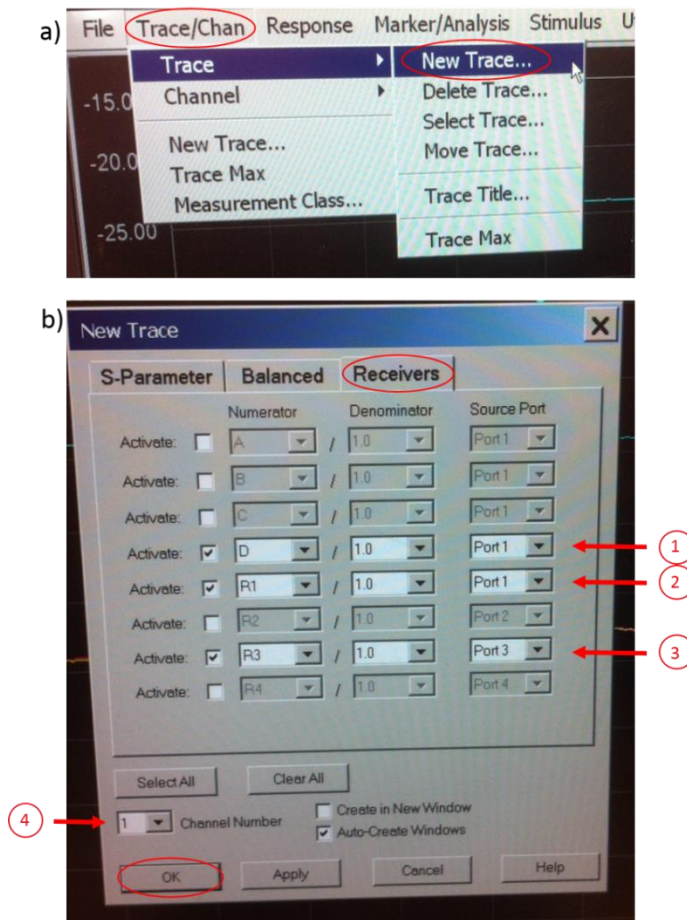


Figure C.4: (a) Creating new trace and (b) activating receivers

Now that the software knows the antenna configuration the next step is to enter in all the phase sweep parameters. These steps are outlined in (Figure C.5). To open the sweep type window (Figure C.5b) the **Stimulus** tab on the top toolbar must first be found. After opening the **Stimulus** tab navigate down to **Sweep** and then over to **Sweep Type...**, which is all outlines in (Figure C.5a). To activate the phase sweep feature on the network analyzer under sweep type the phase sweep option, highlighted by the solid red arrow in (Figure C.5b), must be checked. The next step is to set the sweep properties. For the test done in this report we set the starting phase angle as 0 degrees and the stopping phase angle as 360

degrees. The frequency was either set as 4GHz or 6GHz depending on the test. To apply the phase sweep properties click on **Apply** and then **OK**.

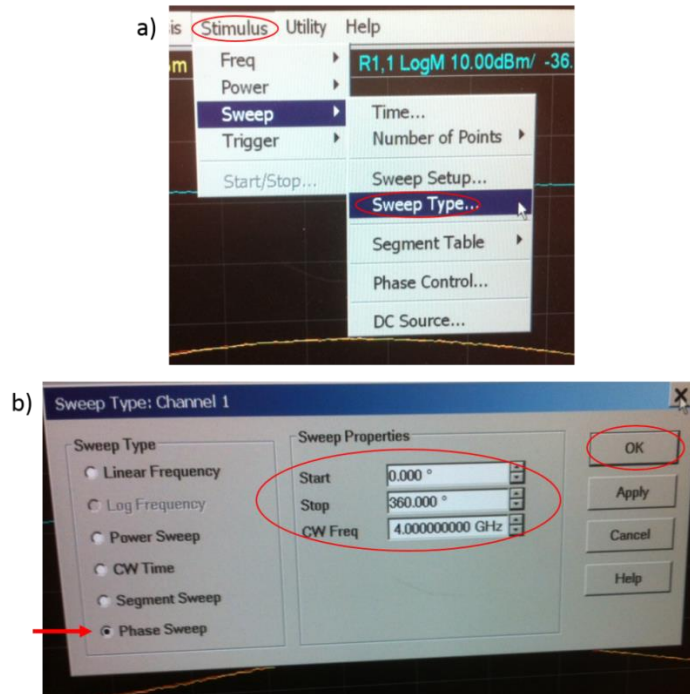


Figure C.5: (a) Selecting the correct sweep type and (b) applying the correct phase sweep parameters

The phase sweep properties and parameter can be modified further or checked by accessing the phase control or the phase control setup windows. To access the phase control window again click on the **Stimulus** tab and scroll down to **Sweep**, but this time navigate and click on the **Phase Control** option. These steps are outlined below in (Figure C.6a). The phase control window, depicted in (Figure C.6b), will then appear on the screen and the phase sweep properties that were entered above can be checked and altered if necessary. In the figure the ports used in the experiments are highlighted by the numbers 1-3. Notice that under the phase control column that port 3 or source antenna #2 is designated as the

reference port or antenna, while the phase of port 1 or source antenna #1 is varied. Under the phase control column for port 1 **a1/b3** means that port 1 is referred to as the controlled source, where the phase angle is varied, and that port 3 is referred to the reference source. Clicking on the **Phase Control Setup** button bounded by the solid red rectangle in (Figure C.6b) on the lower left of the phase control window it is possible to further alter or check the phase sweep parameters.

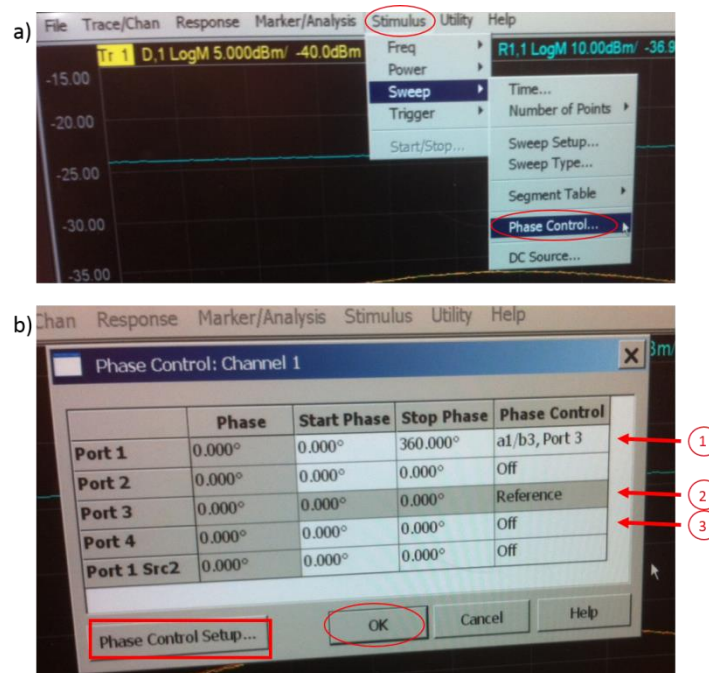


Figure C.6: Making sure all phase sweep parameter are correct. (a) Opening the phase control window. (b) The phase control window.

In the **Phase Control Setup** window the phase control configurations can be changed for each port. To the right of the solid red arrow in (Figure C.7) the particular port of interest can be selected. The reference port and the controlled source/reference source can be altered by selecting other options that appear next to **Referenced to** and **Control Parameter**. These two options highlighted in (Figure C.7) as the solid red ovals. If

necessary other properties like the tolerance and the maximum number of iterations can also be changed in this window. Once all the essential parameters are checked, clicking on **OK** on the phase control setup window will activate all of the selected phase sweep properties.

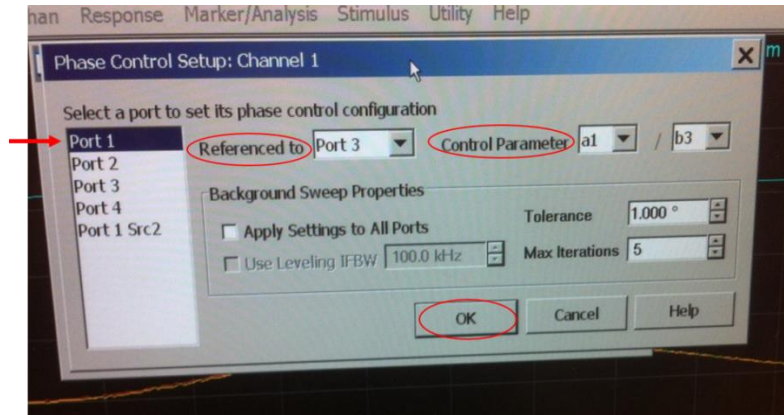


Figure C.7: Checking the phase control parameters

Now that all of the phase sweep parameters have been chosen and checked it is possible to run the phased-array experiments. To run the experiments we must yet again click on the **Stimulus** tab on the toolbar at the top of the home screen and select the **Trigger** option. To run a test for an infinite amount of time click on **Continuous**, to single test (which is govern by parameters selected in **Sweep Time**) click on **Single** and to stop a continuous test click on **Hold**. Any of these options that are shown in (Figure C.8a) can be used to run a phased sweep test on the network analyzer. The raw data from the test can be saved as a .csv file by clicking on **File** and selecting the **Save Data As...** option, which is shown in (Figure C.8b).

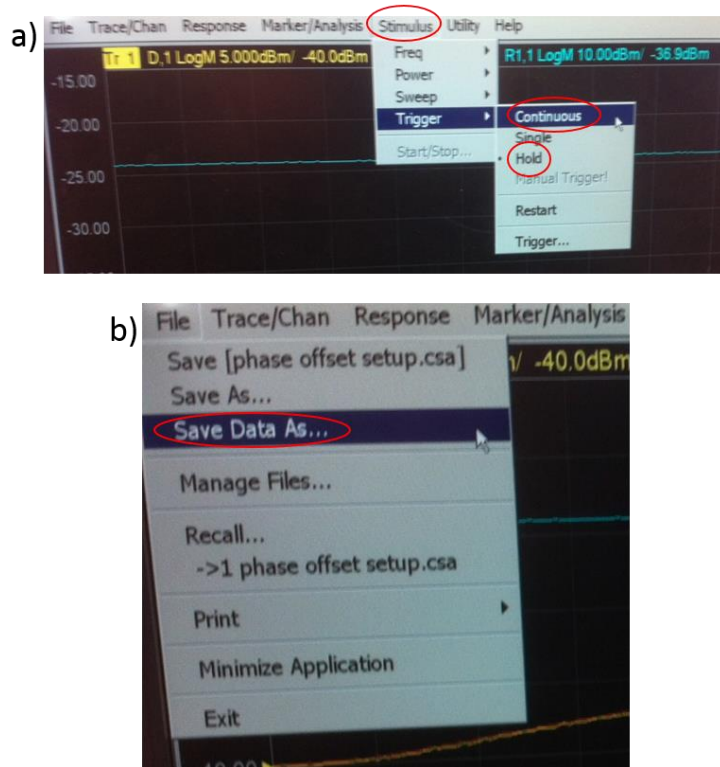


Figure C.8: (a) Running phase sweep function. (b) Saving the data.

Appendix.C.4: S41 and S43 Network Analyzer Software Setup

A simple send and receive test needed to be done on the network analyzer to discover the extent of antenna coupling between the source antennas and the receiver antenna. To enhance the coupling of the antennas a simpler antenna configuration needed to be used that involved less signals. That is the reason why an S41 and an S43 test were chosen to measure the extent of the antenna coupling. Most of the same parameters from the phased-array experiments were used in the S41 and S43 tests. The only differences are that only two antennas are used for each experiment and that the phase angle is fixed at 0 degrees.

The S41 test used port 4 for as the receiver port and port 1 as the source port, while the S43 test used port 4 as the receiver port and port 3 as the source port. It is much simpler to run these types of scatter parameter (S-parameter) tests. These types of tests are designed to determine the scattering effects of electromagnetic radiation using both a source and receiving antenna. Calibrating the cables and assigning power to the antennas is done in the same manner as outlined in Appendix.C.1 and Appendix.C.2, respectfully. The differences in the setup lie when selecting the type of trace that will be used and when selecting the test parameters.

To create a new trace for the S41 and S43 tests starts in the same way as previously outlined in Appendix.C.3. Click on the **Trace/Chan** tab on the toolbar at the top of the home screen. Then scroll over to **Trace** and then to **New Trace**, which is depicted in (Figure C.9a). Select the **S-Parameter** tab of the new trace window. Within this tab check off the S41 option or S43 option depending on the type of test being performed. These options are represented as numbers 1 and 2 in (Figure C.9b). Number 3 on the figure gives you options on which channel to conduct the tests. These test properties are activated in the software after clicking on **Apply** and then **OK**.

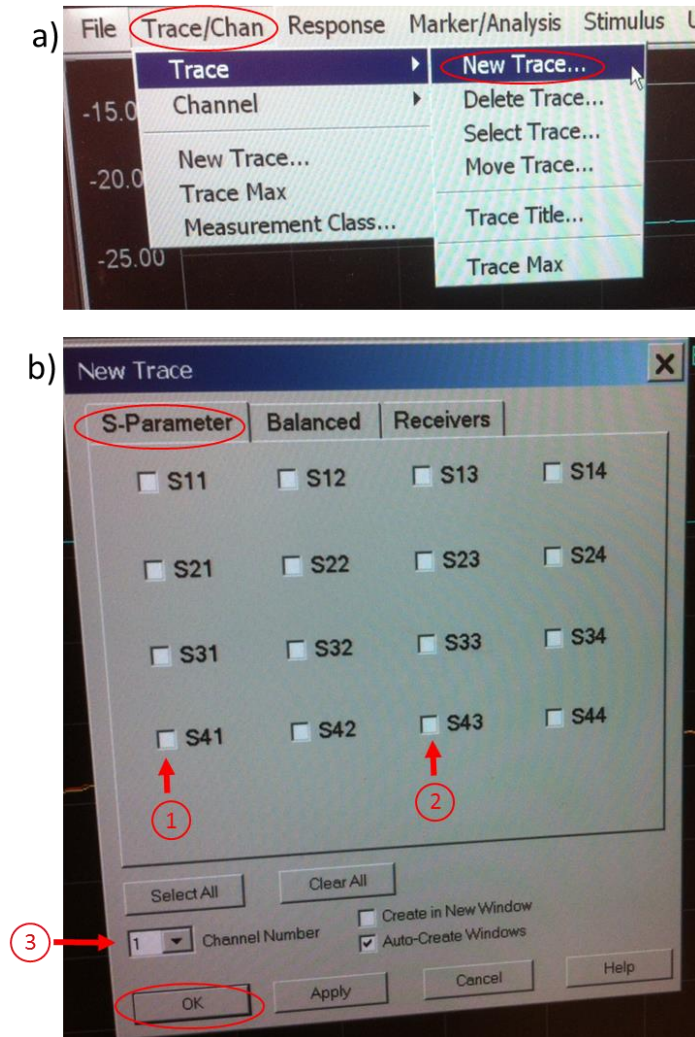


Figure C.9: (a) Creating new trace. (b) Selecting the correct S-Parameters

The network analyzer software now knows the antenna configuration needed to conduct either an S41 or an S43 test. The next step is to enter the sweep properties. These steps are outlined in (Figure C.10). To open the sweep type window (Figure C.10b) the **Stimulus** tab on the top toolbar must first be found. After opening the **Stimulus** tab navigate down to **Sweep** and then over to **Sweep Type...**, which is outlined in (Figure C.10a). For these tests we want to set the sweep type to linear frequency, which is

highlighted by the solid red arrow in (Figure C.10b), must be checked. The next step is to set the sweep properties, but for these S-parameter tests we do not want to vary any parameters. For this test we need to set the starting and stopping frequency to either 4GHz or 6GHz, so as to conduct the tests at a single frequency. The number of data points can also be increased or decreased within this window. To apply these properties click on **Apply** and then **OK**. Any further information on the software used and further understanding of the test parameters can be found in the Agilent Service Guide and PNA Help User's and Programming Guide. [4, 5].

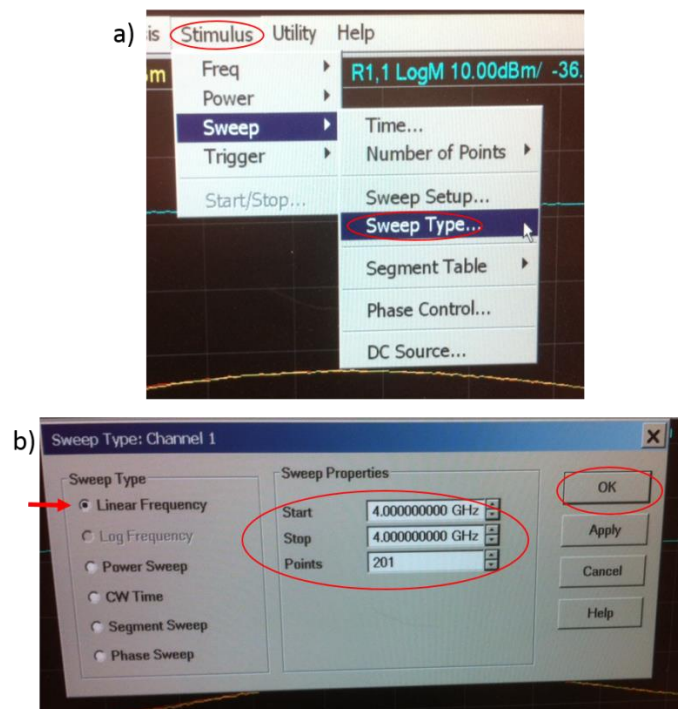


Figure C.10: (a) Selecting the correct sweep type. (b) Applying the correct frequency sweep parameters.

APPENDIX D: PHASED-ARRAY PLOTS FROM MULTIPLE TESTS AT DIFFERENT PHASE OFFSETS

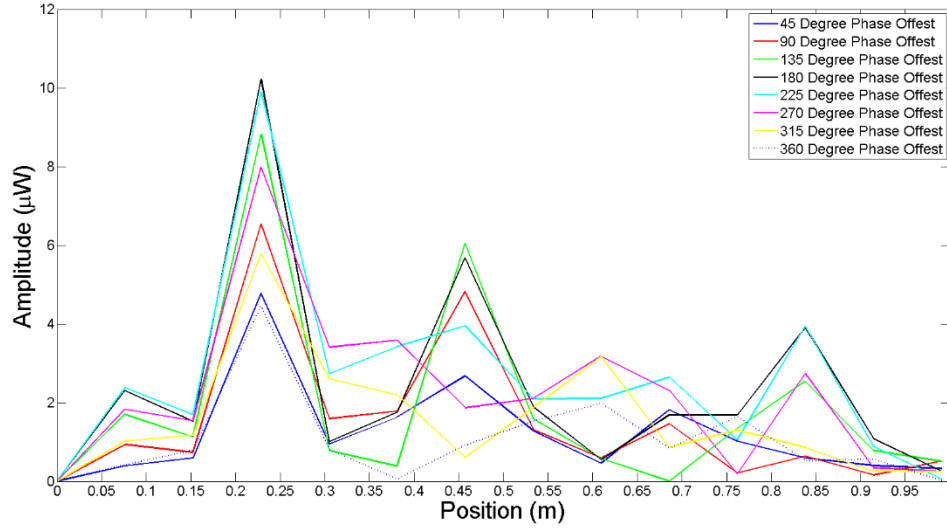


Figure D.1: Test 3 Plotting Phase Offsets Every 45 Degrees

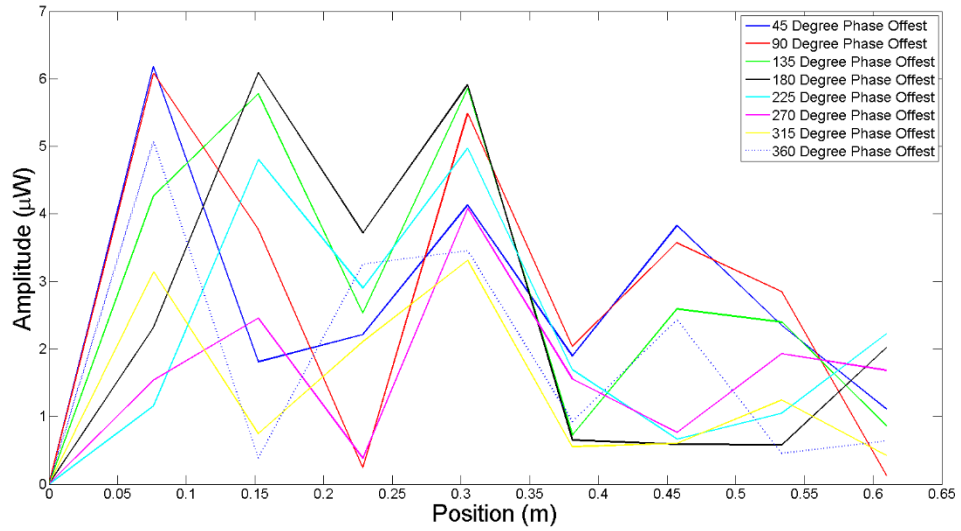


Figure D.2: Test 4a Plotting Phase Offsets Every 45 Degrees

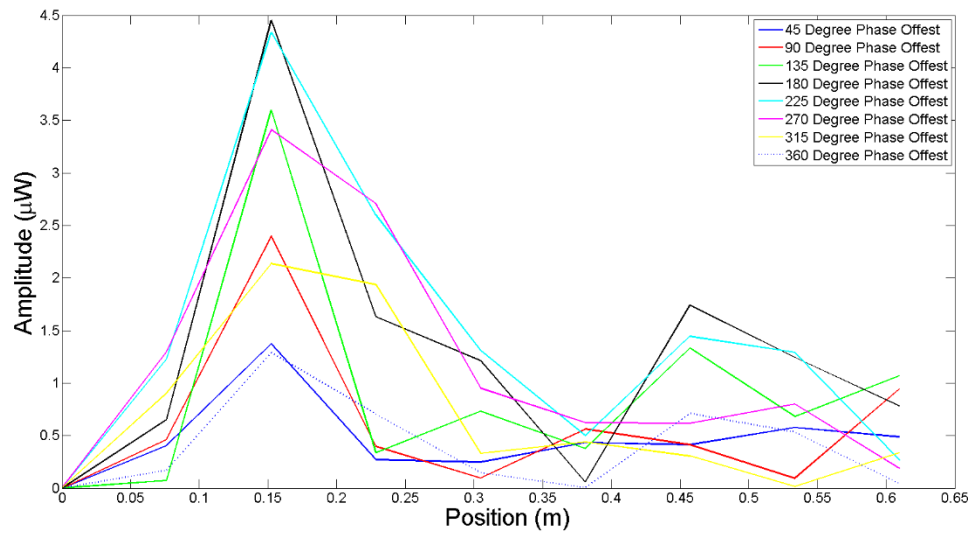


Figure D.3: Test 5a Plotting Phase Offsets Every 45 Degrees

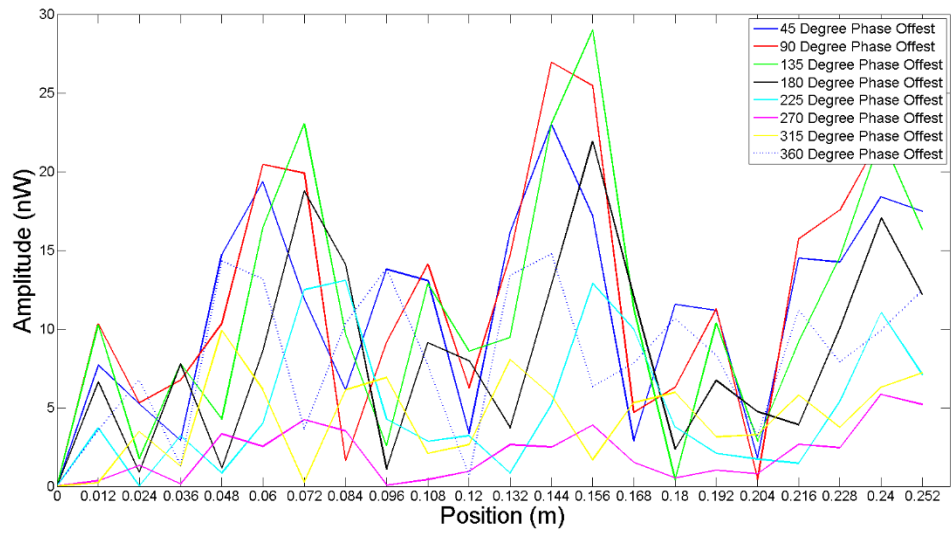


Figure D.4: Test 10 Plotting Phase Offsets Every 45 Degrees

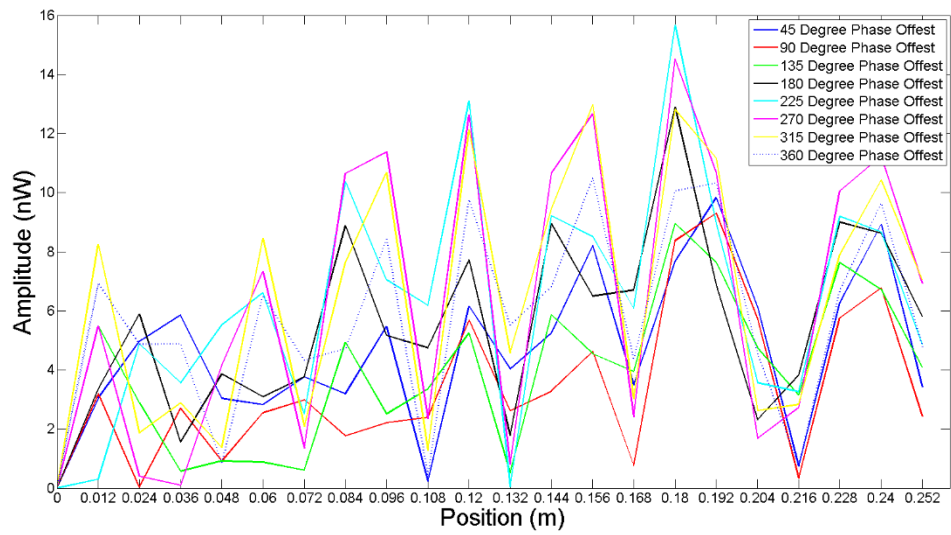


Figure D.5: Test 12 Plotting Phase Offsets Every 45 Degrees

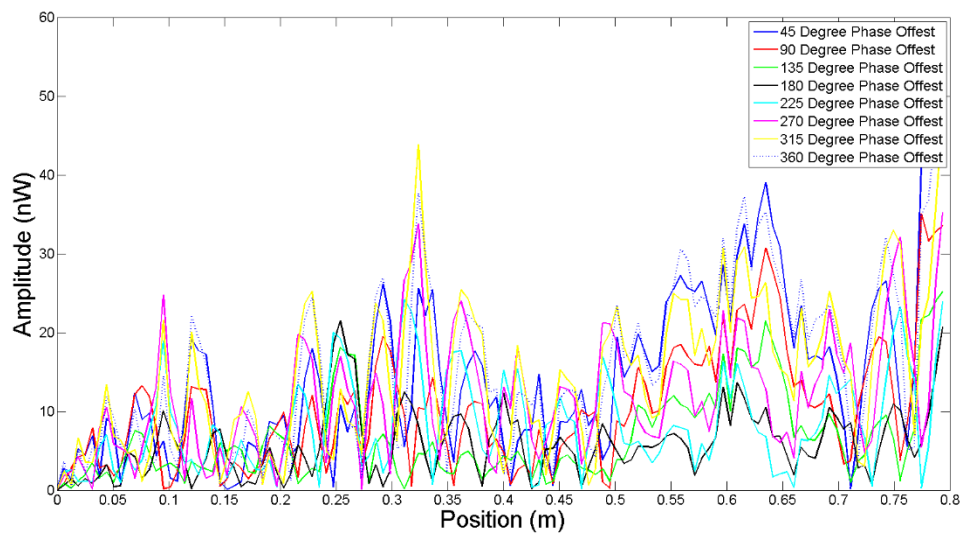


Figure D.6: Test 13 Plotting Phase Offsets Every 45 Degrees

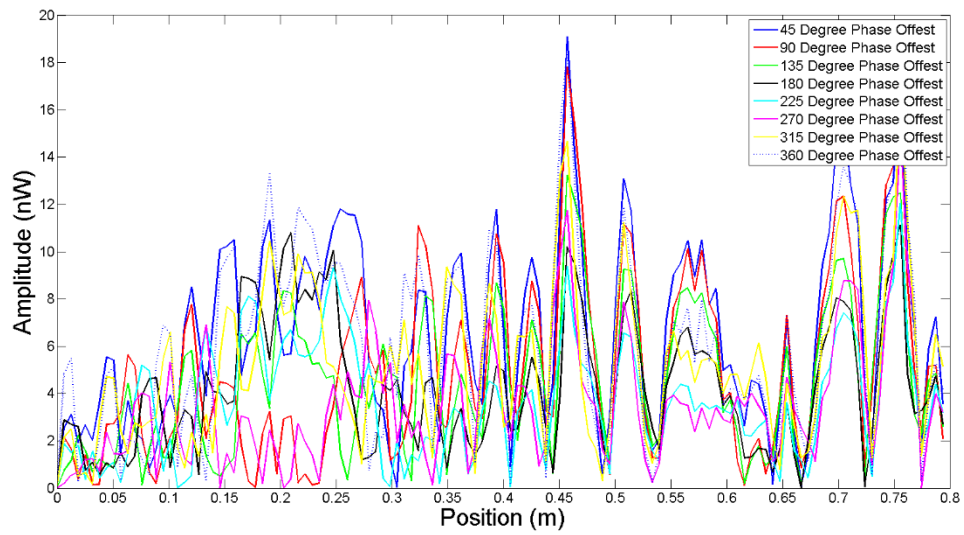


Figure D.7: Test 14 Plotting Phase Offsets Every 45 Degrees

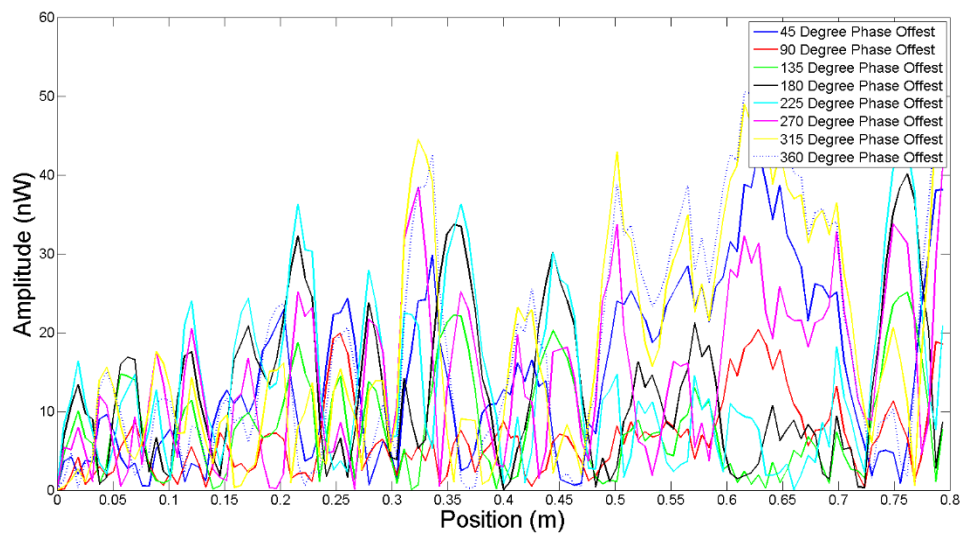


Figure D.8: Test 15 Plotting Phase Offsets Every 45 Degrees (Retest of Test 13)

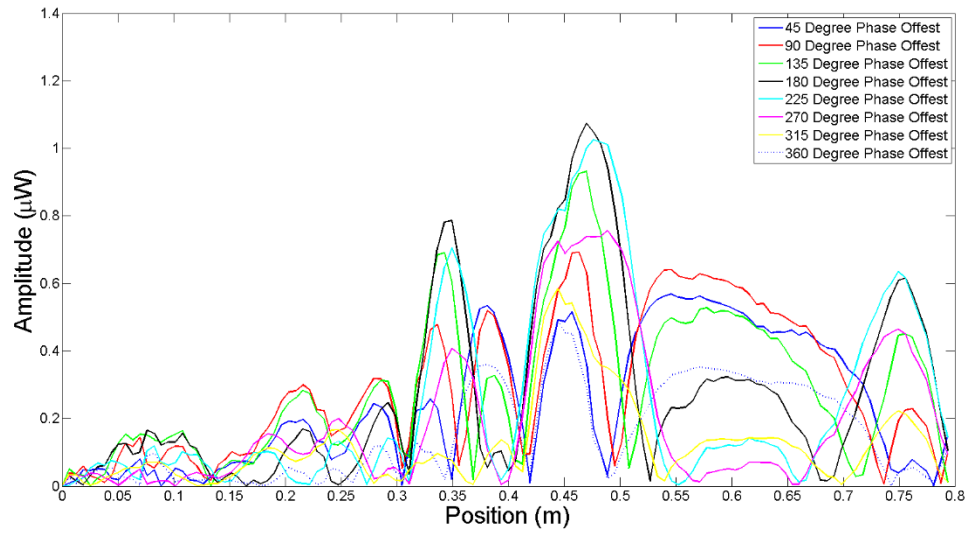


Figure D.9: Test 20 Plotting Phase Offsets Every 45 Degrees

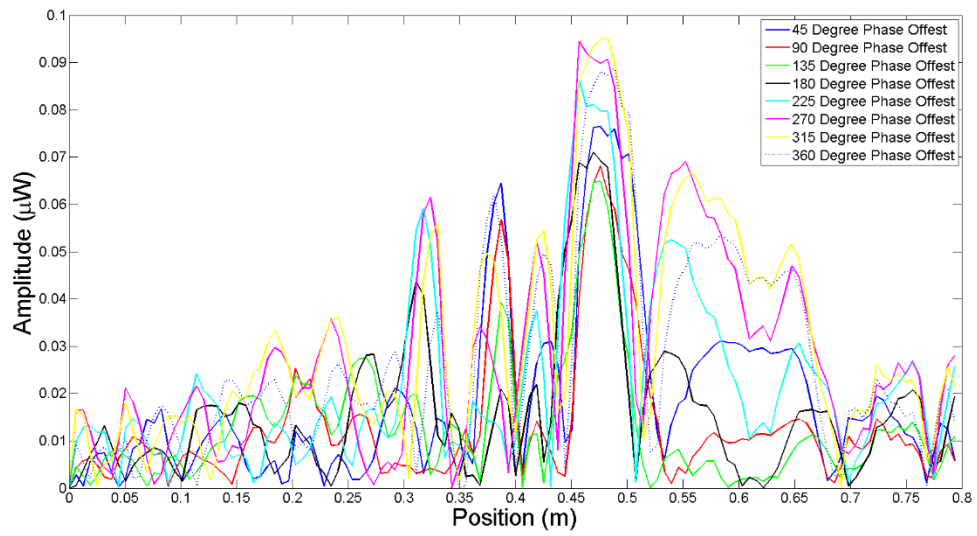


Figure D.10: Test 21 Plotting Phase Offsets Every 45 Degrees

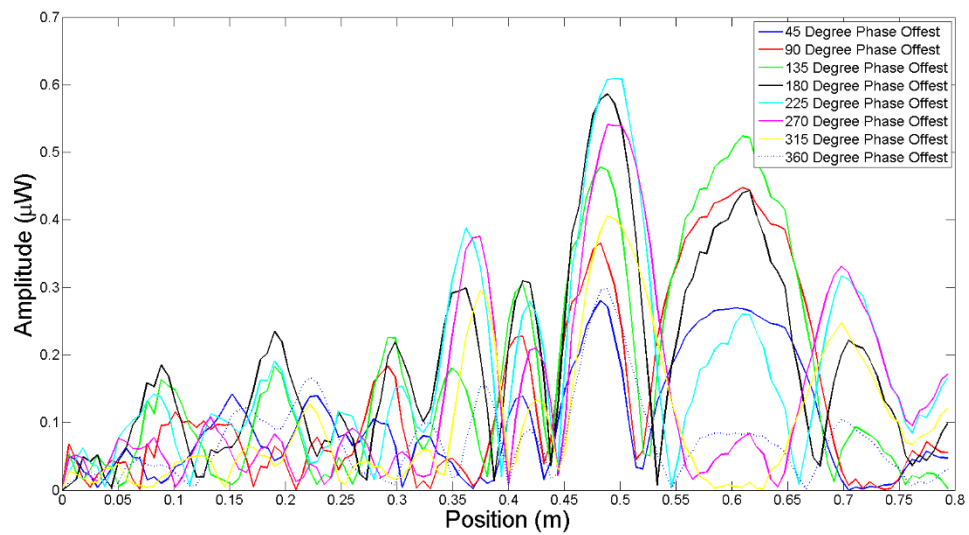


Figure D.11: Test 22 Plotting Phase Offsets Every 45 Degrees

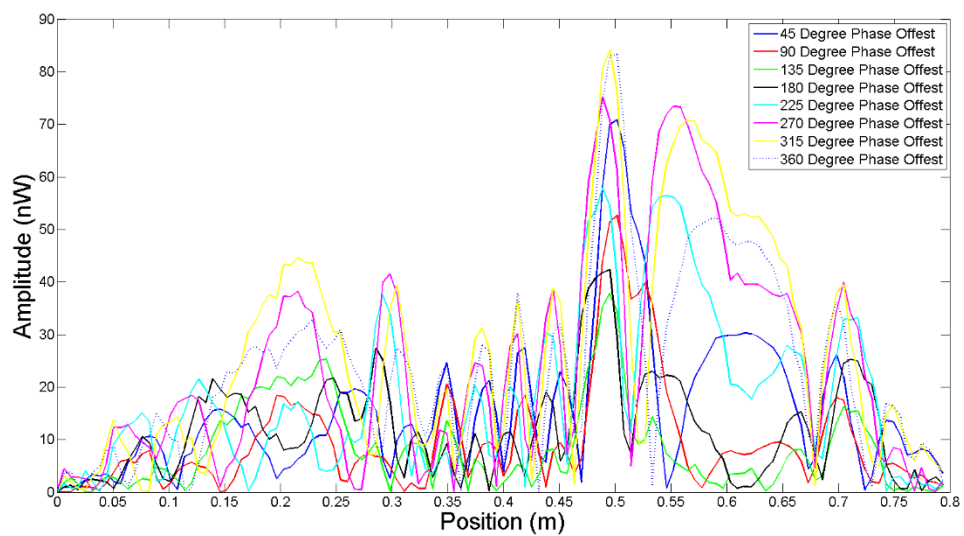


Figure D.12: Test 23 Plotting Phase Offsets Every 45 Degrees

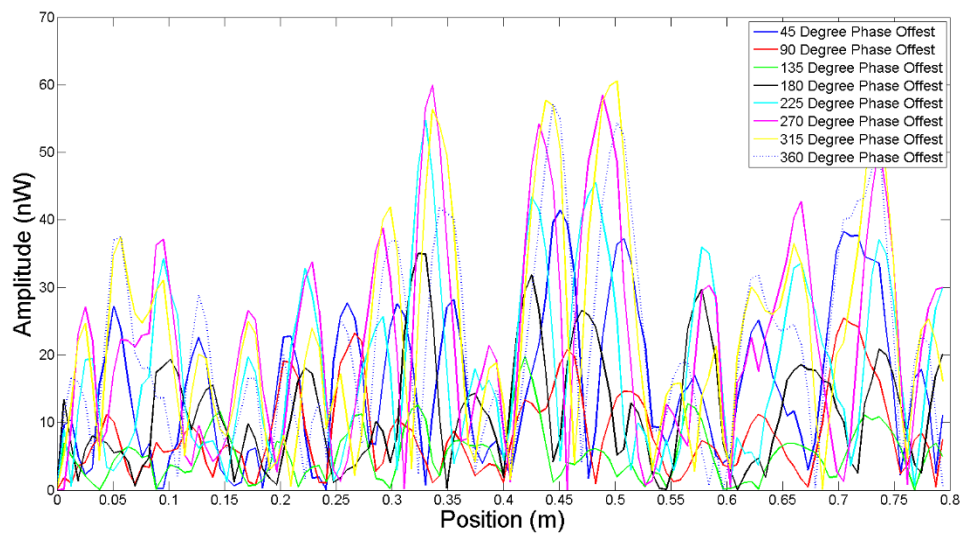


Figure D.13: Test 25 Plotting Phase Offsets Every 45 Degrees

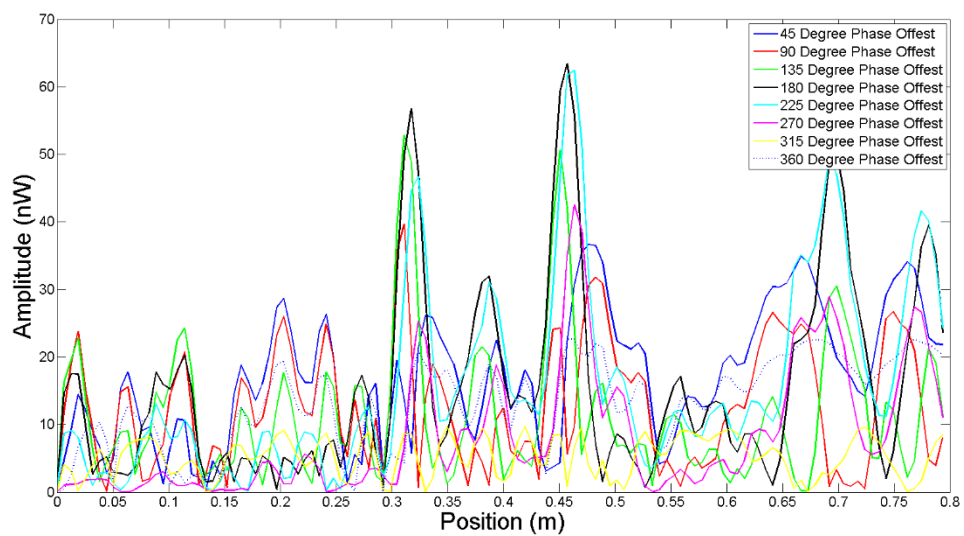


Figure D.14: Test 27 Plotting Phase Offsets Every 45 Degrees

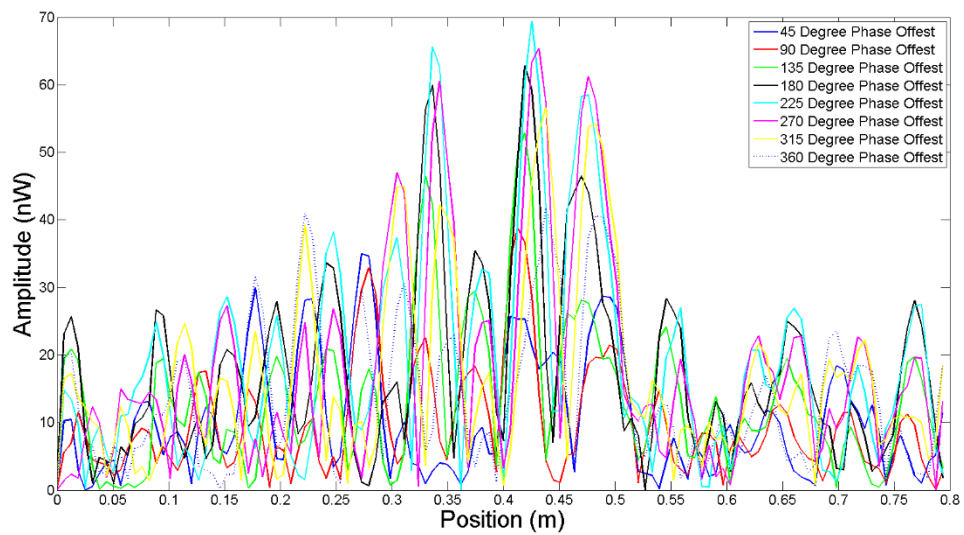


Figure D.15: Test 28 Plotting Phase Offsets Every 45 Degrees

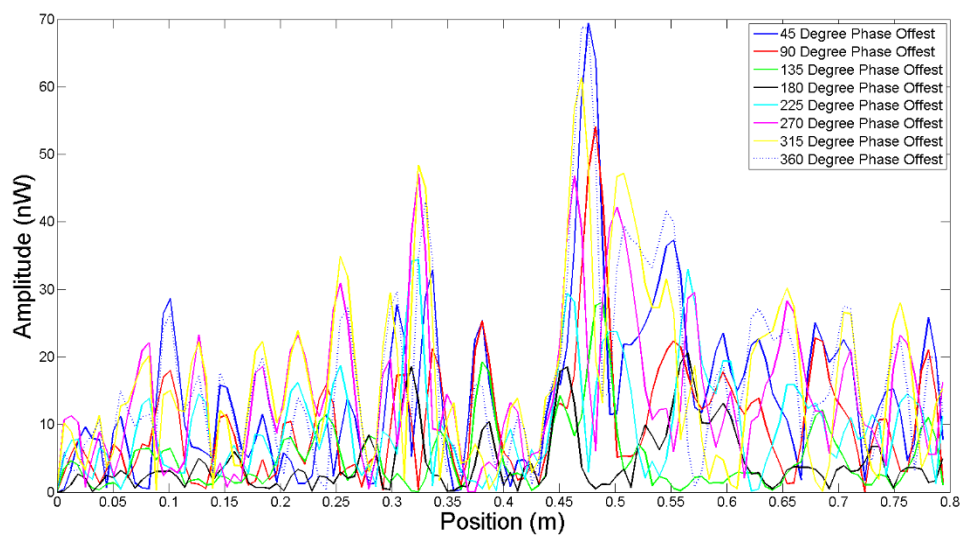


Figure D.16: Test 30 Plotting Phase Offsets Every 45 Degrees

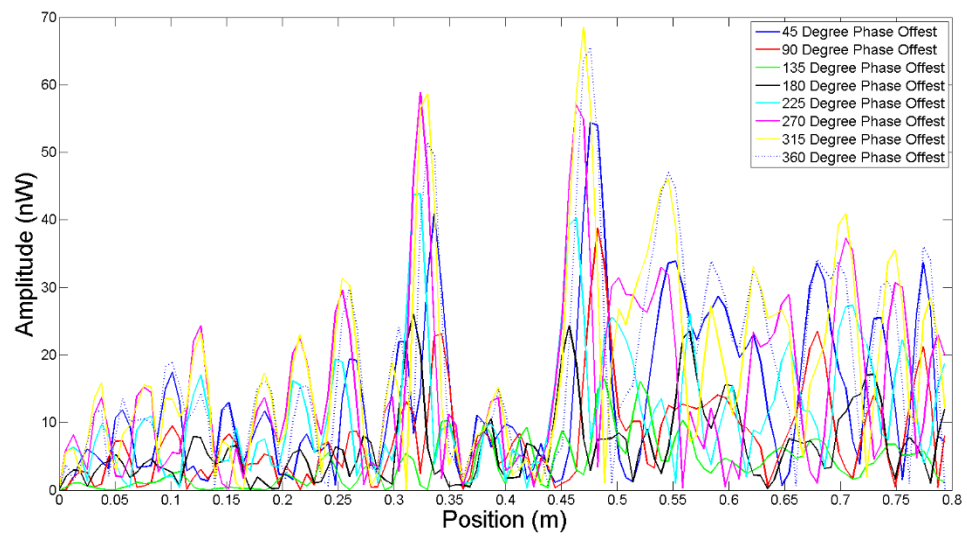


Figure D.17: Test 32 Plotting Phase Offsets Every 45 Degrees

APPENDIX E: A.H. SYSTEMS DOUBLE RIDGE HORN ANTENNA SPECIFICATIONS



A.H. Systems, Inc.

9710 Cozycroft Ave.
Chatsworth, CA 91311



Tel: (818) 998-0223



sales@AHSystems.com

Fax: (818) 998-6892

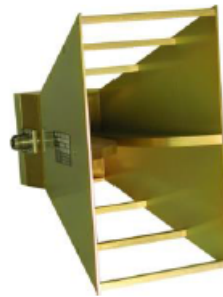


www.AHSystems.com

SAS-571

Double Ridge Guide Horn Antenna
700 MHz – 18 GHz

High gain, low VSWR, input handling capability up to 300 watts CW, and rugged design make this horn antenna excellent for both immunity and emissions testing.



Frequency Range: 700 MHz - 18 GHz

Antenna Factor: 22 to 44 dB

Gain (dBi): 1.4 to 15 dBi

Maximum Continuous Power: 300 Watts

Max Radiated Field: 200 V/m

Pattern Type: directional

3dB Beamwidth (E-Field): 48°

3dB Beamwidth (H-Field): 30°

Impedance: 50 Ω

VSWR: 1.6:1 (3.5:1 max)

Connector: N-Type, female

Mounting Base: 1/4 - 20 Thread, female

Features

- Broad Frequency Range of 700 MHz to 18 GHz
- Linearly Polarized High Gain, Low VSWR
- Individually Calibrated
- Three year Warranty

The SAS-571 Double Ridge Guide Horn Antenna is lightweight, compact and has been manufactured for maximum gain, low VSWR and broadband response. The double ridge guide horn antenna was initially designed for surveillance where a high gain broadband response was required. The original design was to have a 30-degree beamwidth, which is ideal for EMI measurements and compliance testing.

Recommended Accessories

- PAM-0118 (Preamplifier)
- SAC-18G-3 (3 Meter Low Loss Cable)
- SAC-18G-0.5 (0.5 Meter Low Loss Cable)



A.H. Systems, Inc.
9710 Cozycroft Ave.
Chatsworth, CA 91311



Tel: (818) 998-0223

◆ sales@AHSystems.com

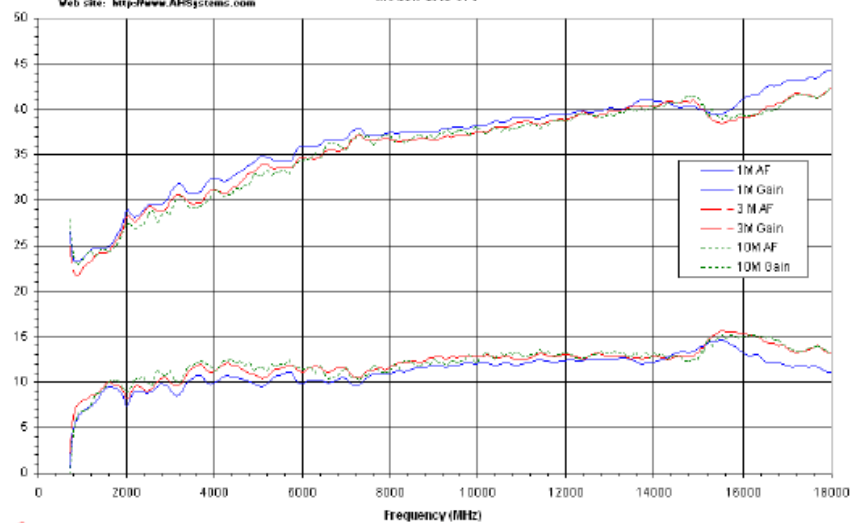
Fax: (818) 998-6892

◆ www.AHSystems.com



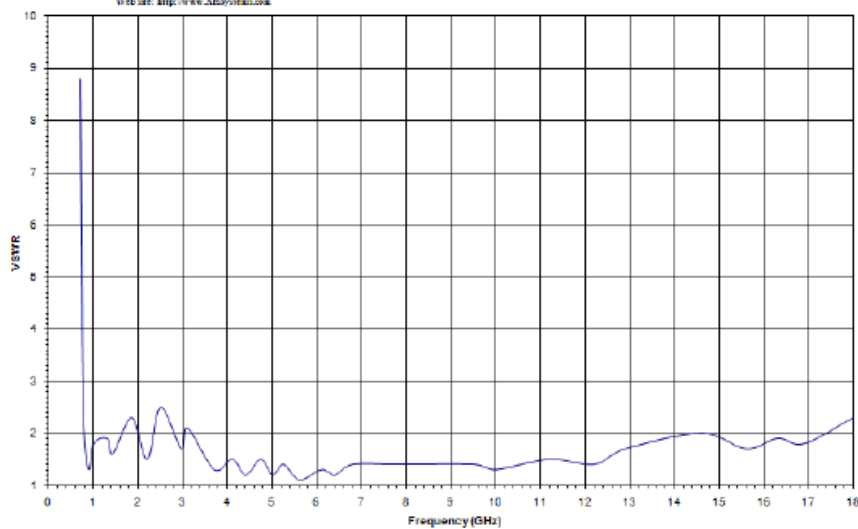
A.H. Systems Inc.
9710 Cozycroft Ave. Chatsworth, CA 91311
Phone: (818) 998-0223 Fax: (818) 998-6892
E-mail: sales@AHSystems.com
Web site: <http://www.AHSystems.com>

**Double Ridge Guide
Horn Antenna
Model: SAS-571**



A.H. Systems Inc.
9710 Cozycroft Ave. Chatsworth, CA 91311
Phone: (818) 998-0223 Fax: (818) 998-6892
E-mail: info@AHSystems.com
Web site: <http://www.AHSystems.com>

**VSWR
Double Ridge Guide Horn Antenna
Model SAS-571**





A.H. Systems, Inc.
9710 Cozycroft Ave.
Chatsworth, CA 91311



Tel: (818) 998-0223

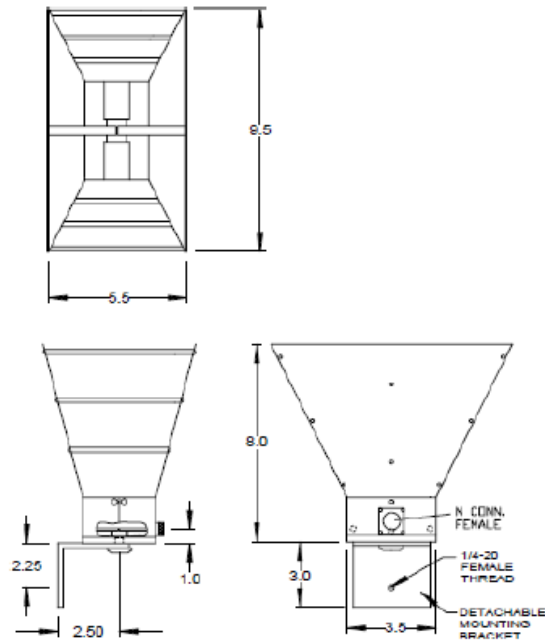


sales@AHSystems.com

Fax: (818) 998-6892



www.AHSystems.com



Physical Dimensions:

Length: 11.0 in. (27.9 cm)

Width: 5.6 in. (14.2 cm)

Height: 9.6 in. (24.4 cm)

Weight: 3.5 lb.'s (1.59 kg)

Aperture: 5.5" x 9.6" (13.9cm x 24.4cm)

Horn antenna specifications [24].



A.H. Systems Inc.
9710 Cozycroft Ave. Chatsworth, CA 91311
Phone (818) 998-0223 Fax (818) 998-6892
E-mail: sales@A.H.Systems.com
Web site: <http://www.AHSystems.com>

Radiation Pattern
Horizontal Polarization
Model: SAS-571

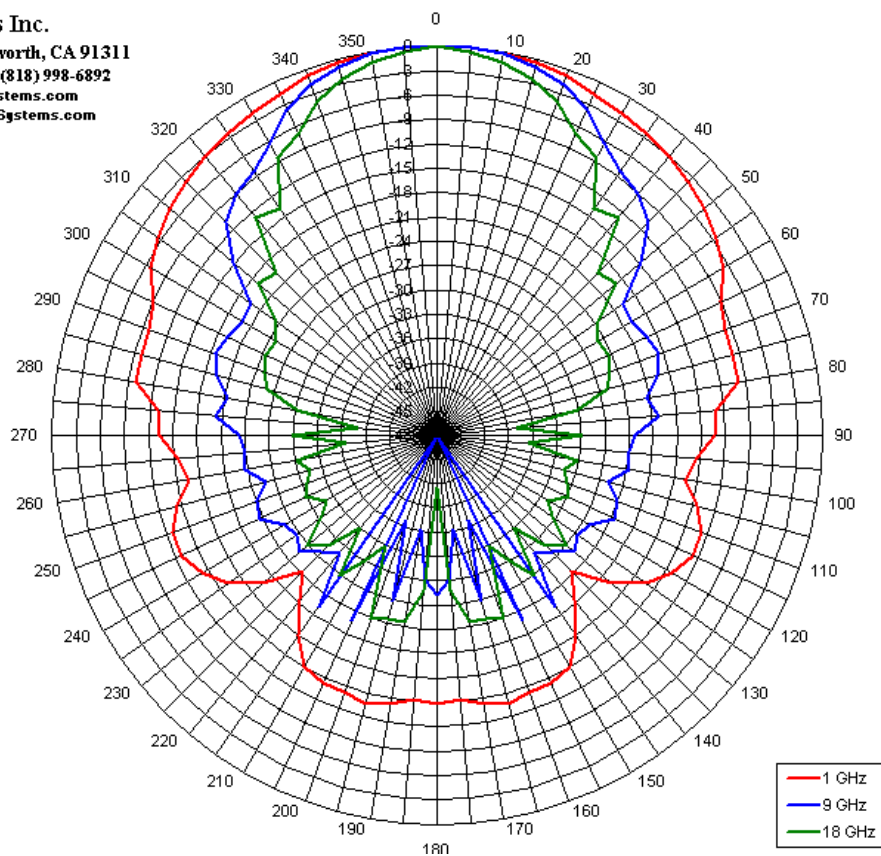
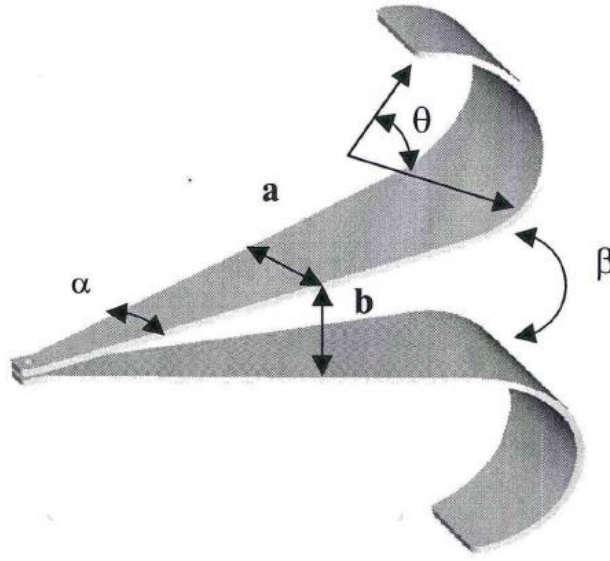


Figure E.1: A.H. Systems double ridge horn antenna radiation pattern [24].

APPENDIX F: HOME-MADE GIMA ANTENNA SPECIFICATIONS



GIMA-6	$\alpha = 12.95\text{deg.}$, $\beta = 5.52\text{deg.}$, $a_1 = 2\text{mm}$, $a_2 = 120\text{mm}$, $b_1 = 12\text{mm}$, $b_2 = 120\text{mm}$, $L_1 = 300\text{mm}$, $L_2 = 60\text{mm}$, $L_3 = 120\text{mm}$, $R = 45.86\text{mm}$, $\theta = 150\text{deg.}$	Length of the straight section is half wavelength of the lowest frequency.
--------	--	--

Figure F.1: GIMA antenna design with critical dimensions [28]

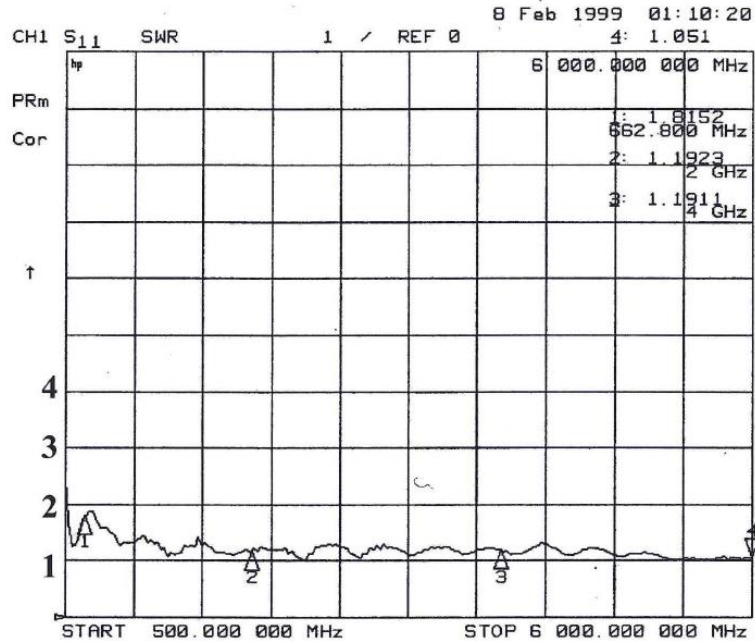


Figure F.2: SWR results for the GIMA antenna. Close to ideal impedance throughout the frequency range [28].

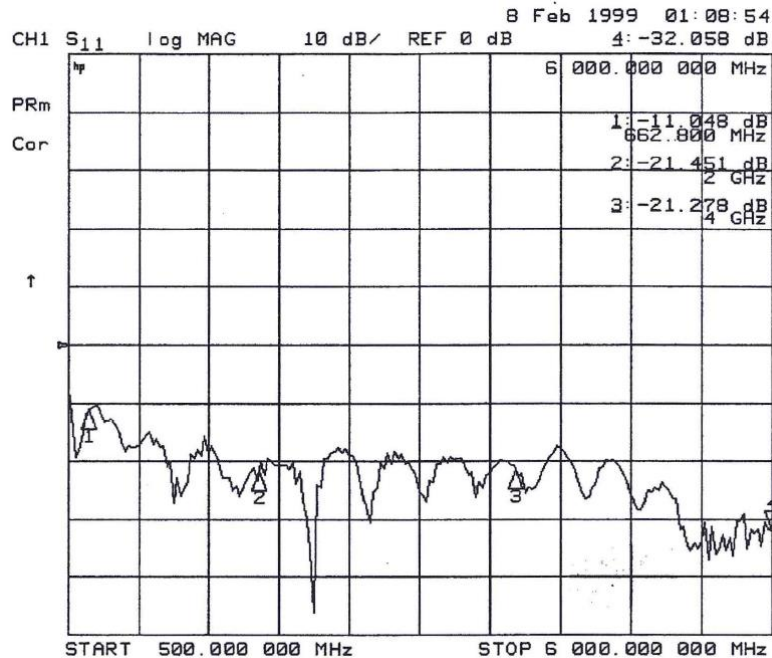


Figure F.3: Return loss results for the GIMA antenna. Average return loss of -20dB with an accepted power of approximately 99.2%. The antenna is frequency independent and has a high radiation efficiency [28].

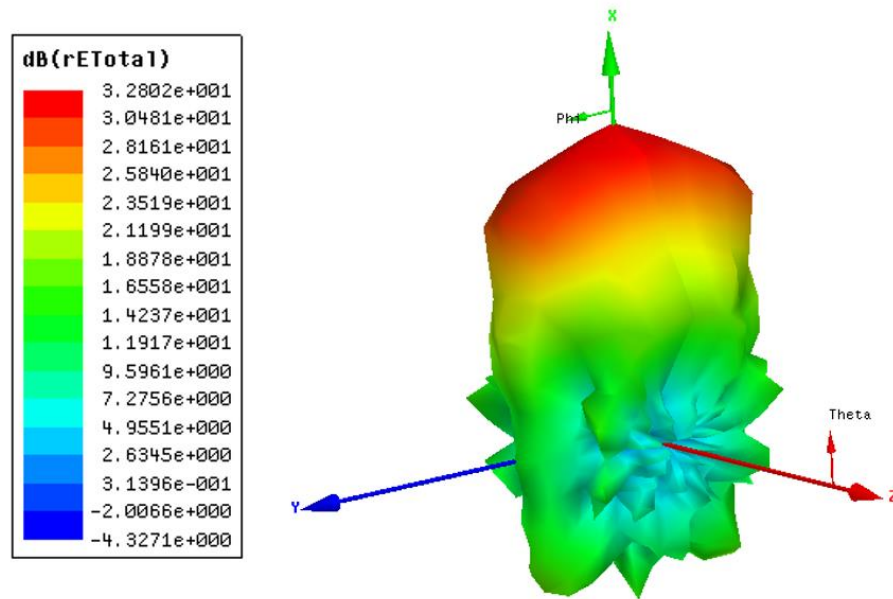


Figure F.4: Simulated radiation pattern of the home-made GIMA antenna using HFSS [28].

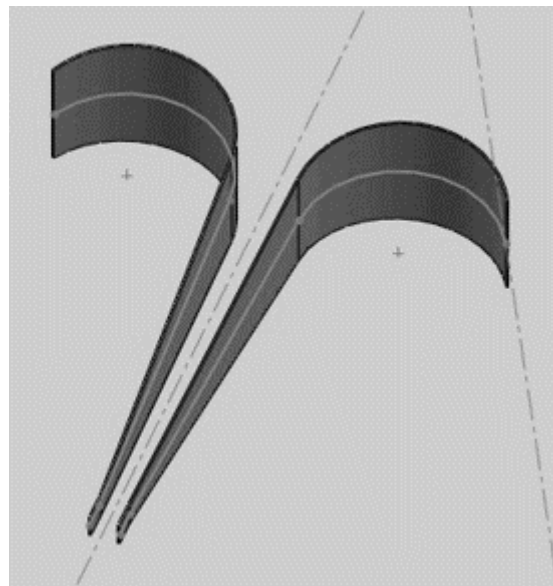


Figure F.5: Solidworks model of the GIMA antenna used to simulate the antenna radiation pattern [26].

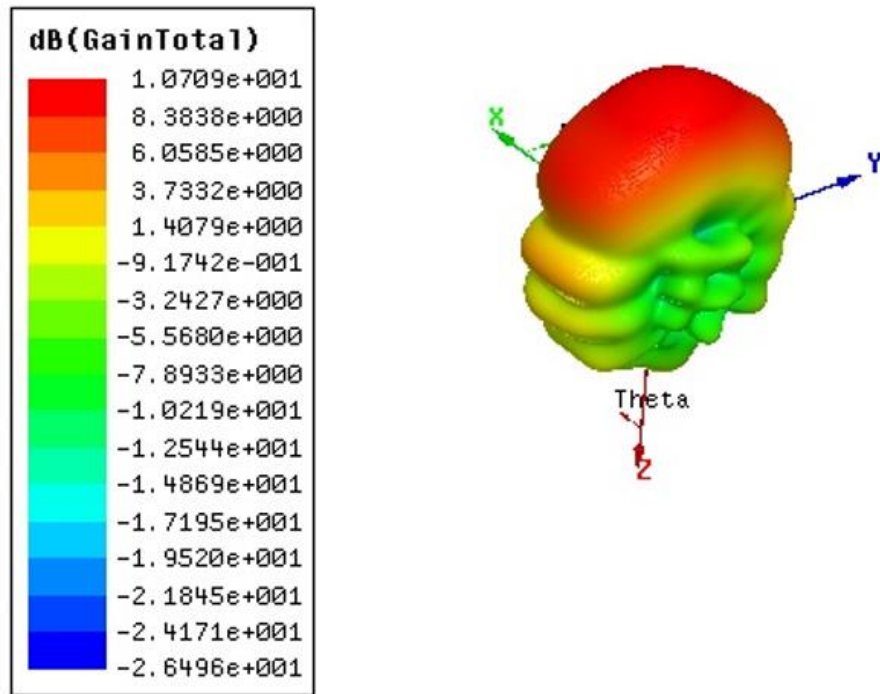


Figure F.6: Simulated radiation pattern of the home-made GIMA antenna at a frequency of 2.8 using HFSS [26].

APPENDIX G: MATLAB CODES USED TO ANALYZE DATA FROM EXPERIMENTS

Appendix.G.1: Code for tests 10-13

```
%Jonathan Razinger
%2013 Research
%9/3/13
% %% Phased Array Test .5" diameter rod moving at .5" increments

%% Get List of Files in Directory
clear

dirname = ('F:\2012-2014 Research\GPR Radar\Phase offset\Test 10 at
4GHz\Rod over concrete small spacing\Data'); % Finding Folder (Changed
for every test)
files = dir(fullfile(dirname, '*.csv')); % Specified files within
folder

fprintf('Files to process:\n'); %Recognizing the files that need to be
used
fprintf('    %s\n', files.name)
%% Run Wind Data Analysis
% Then, we loop through each file and perform the analysis, storing the
% results into a structure.

% Pre-allocate results structure
megawatts(length(files)) = struct('Phase', [], 'dB', [], 'Angle', [],
'Rad', [], 'mW', []);

for ii = 1:length(files);
    % Get filename
    filename = fullfile(dirname, files(ii).name);

    % Display filename
    fprintf('\nAnalyzing %s. \n', filename);

    % Generate and save results
    Megawatts(ii) = mw1(filename);

    snapnow;    % used for publishing
end

%% Create Full matrix of mW values

n=1:1:2; %Re-arranging positions, because of the way they are imported
s=16:1:22;
```

```

f=4:1:10;
z=11:1:12;
x=14:1:15;
positions1=horzcat(Megawatts(1,n).mW);
positions2=horzcat(Megawatts(1,s).mW);
positions3=Megawatts(1,13).mW;
positions4=Megawatts(1,3).mW;
positions5=horzcat(Megawatts(1,f).mW);
positions6=horzcat(Megawatts(1,z).mW);
positions7=horzcat(Megawatts(1,x).mW);
positions=horzcat(positions1,positions3,positions2,positions4,positions
5,positions6,positions7); %Finding the mW values from the Megawatts
structure for each position and creating a matrix from all the vectors

cb= repmat(Megawatts(1,1).mW,1,22); %Creates a 201:22 Matrix only made
up vector Megawatts(1,1).mW being repeated (Concrete background)
q=positions-cb; %Background subtract (Each position subtracting the
concrete background)
PhaseM= repmat(Megawatts(1,1).Phase,1,22); %Creates a 201:22 Matrix only
made up vector Megawatts(1,1).Phase being repeated
Real=(cos(PhaseM).*q); %Real part of Magnitude
Imaginary=(sin(PhaseM).*q); %Imaginary part of Magnitude
c=complex(Real,Imaginary); %Magnitude in complex form
Magnitude=sqrt((Real.^2)+(Imaginary.^2)); %Amplitude
%% Plotting Magnitude vs. Position

g=0:.012:.252; % Distance increments (m), moving the rod every 1/2"
a=1000000*ones(1,22); % Conversion to nW (Changed for antenna
configuration #2)

figure(1) % Creating plots at 45 degree phase offset intervals
plot(g,Magnitude(26,1:22).*a,'a','LineWidth',2) % Phase offset of 45
degrees
hold on
plot(g,Magnitude(51,1:22).*a,'r','LineWidth',2) % Phase offset of 90
degrees
hold on
plot(g,Magnitude(76,1:22).*a,'g','LineWidth',2) % Phase offset of 135
degrees
hold on
plot(g,Magnitude(101,1:22).*a,'k','LineWidth',2) % Phase offset of 180
degrees
hold on
plot(g,Magnitude(126,1:22).*a,'c','LineWidth',2) % Phase offset of 225
degrees
hold on
plot(g,Magnitude(151,1:22).*a,'m','LineWidth',2) % Phase offset of 270
degrees
hold on
plot(g,Magnitude(176,1:22).*a,'y','LineWidth',2) % Phase offset of 315
degrees
hold on

```

```

plot(g,Magnitude(201,1:22).*a,':','LineWidth',2) % Phase offset of 360
degrees

xlim([0 .26]) %Setting X axis limits
set(gca,'XTick',0:.012:.252,'FontSize',18); % Sets increments for X
axis
set(gcf,'Color',[1,1,1]); % Sets Border color to white
xlabel('Position (m)','FontSize',30);
ylabel('Amplitude (nW)','FontSize',30);
%title('Amplitude vs. Position at 4GHz','FontSize',20);
legend('45 Degree Phase Offest','90 Degree Phase Offest','135 Degree
Phase Offest','180 Degree Phase Offest','225 Degree Phase Offest','270
Degree Phase Offest','315 Degree Phase Offest','360 Degree Phase
Offest');

figure(2) % Plot at selected phase offsets (Would change depending on
test)
plot(g,Magnitude(51,1:22).*a,'r','LineWidth',2) % Phase offset of 90
degrees
hold on
plot(g,Magnitude(76,1:22).*a,'g','LineWidth',2) % Phase offset of 135
degrees
hold on
plot(g,Magnitude(151,1:22).*a,'m','LineWidth',2) % Phase offset of 270
degrees
xlim([0 .26]) %Setting X axis limits
set(gca,'XTick',0:.012:.252,'FontSize',18); % Sets increments for X
axis
set(gcf,'Color',[1,1,1]); % Sets Border color to white
xlabel('Position (m)','FontSize',30);
ylabel('Amplitude (nW)','FontSize',30);
%title('Amplitude vs. Position at 4GHz','FontSize',20);
legend('90 Degree Phase Offest','135 Degree Phase Offest','270 Degree
Phase Offest');

%s=swap(Magnitude,2,3,13);
%f=swap(Magnitude,2,4:10,16:22);
%csvwrite('F:\2012-2013 Research\2014 Masters Thesis\Exports\Test 10
phases.csv',[Magnitude(26,1:22);Magnitude(51,1:22);Magnitude(76,1:22);M
agnitude(101,1:22);Magnitude(126,1:22);Magnitude(151,1:22);Magnitude(17
6,1:22);Magnitude(201,1:22)]);

```

Appendix.G.2: Code for tests 3-5a, 13-15, 20-29, 30, 32

```
%Jonathan Razinger
%2013 Research
%9/3/13
% %% Phased Array Test .5" diameter rod moving at .25" increments

%% Get List of Files in Directory
clear

dirname = ('F:\2012-2014 Research\GPR Radar\Phase offset\Test 13 at
4GHz\Rod at .25 increments on whole slab'); % Finding Folder (Changed
for every test)
files = dir(fullfile(dirname, '*.csv')); % Specified files within
folder

fprintf('Files to process:\n'); %Recognizing the files that need to be
used
fprintf('    %s\n', files.name)
%% Run Wind Data Analysis
% Then, we loop through each file and perform the analysis, storing the
% results into a structure.

% Pre-allocate results structure
megawatts(length(files)) = struct('Phase', [], 'dB', [], 'Angle', [],
'Rad', [], 'mW', []);

for ii = 1:length(files);
    % Get filename
    filename = fullfile(dirname, files(ii).name);

    % Display filename
    fprintf('\nAnalyzing %s. \n', filename);

    % Generate and save results
    Megawatts(ii) = mw1(filename);

    snapnow;    % used for publishing
end

%% Create Full matrix of mW values

n=1:1:126;
positions=horzcat(Megawatts(1,n).mW);

cb= repmat(Megawatts(1,1).mW,1,126); %Creates a 201:22 Matrix only made
up vector Megawatts(1,1).mW being repeated (Concrete background)
```



```

q=positions-cb; %Background subtract (Each position subtracting the
concrete background)
PhaseM= repmat(Megawatts(1,1).Phase,1,126); %Creates a 201:22 Matrix
only made up vector Megawatts(1,1).Phase being repeated
Real=(cos(PhaseM).*q); %Real part of Magnitude
Imaginary=(sin(PhaseM).*q); %Imaginary part of Magnitude
c=complex(Real,Imaginary); %Magnitude in complex form
Magnitude=sqrt((Real.^2)+(Imaginary.^2)); %Amplitude

Angles=horzcat(Megawatts(1,n).Angle); % Matrix of phase angles
(degrees) at all positions
Angles(:,1)=0; % Making first column which represents concrete
background phase angles =0
Rad=horzcat(Megawatts(1,n).Rad); % Matrix of phase angles (Radians) at
all positions
Rad(:,1)=0; % Making first column which represents concrete background
phase angles =0
%% Plotting Magnitude vs. Position

g=0:.00635:.79375; % Distance increments (m), moving the rod every 1/2"
%g=transpose([0:.012:.252]);
a=1000000*ones(1,126); % Conversion to nW (Changed for antenna
configuration #2)

figure(1) % Creating plots at 45 degree phase offset intervals
plot(g,Magnitude(26,1:126).*a,'LineWidth',2) % Phase offset of 45
degrees
hold on
plot(g,Magnitude(51,1:126).*a,'r','LineWidth',2) % Phase offset of 90
degrees
hold on
plot(g,Magnitude(76,1:126).*a,'g','LineWidth',2) % Phase offset of 135
degrees
hold on
plot(g,Magnitude(101,1:126).*a,'k','LineWidth',2) % Phase offset of 180
degrees
hold on
plot(g,Magnitude(126,1:126).*a,'c','LineWidth',2) % Phase offset of 225
degrees
hold on
plot(g,Magnitude(151,1:126).*a,'m','LineWidth',2) % Phase offset of 270
degrees
hold on
plot(g,Magnitude(176,1:126).*a,'y','LineWidth',2) % Phase offset of 315
degrees
hold on
plot(g,Magnitude(201,1:126).*a,':','LineWidth',2) % Phase offset of 360
degrees

xlim([0 .8]) %Setting X axis limits
set(gca,'XTick',0:.05:.8,'FontSize',18); % Sets increments for X axis
set(gcf,'Color',[1,1,1]); % Sets Border color to white
xlabel('Position (m)','FontSize',30);

```

```

ylabel('Amplitude (nW)','FontSize',30);
%title('Amplitude vs. Position at 4GHz with Incremental Steps of .25in
','FontSize',20);
legend('45 Degree Phase Offest','90 Degree Phase Offest','135 Degree
Phase Offest','180 Degree Phase Offest','225 Degree Phase Offest','270
Degree Phase Offest','315 Degree Phase Offest','360 Degree Phase
Offest');
%s=linalg::swapCol(Magnitude, 3, 13);
%Magnitude(:,3)=Magnitude(:,13 3]

figure(2) % Plotting at selected phase offsets (Changed depending on
test)
plot(g,Magnitude(151,1:126).*a,'m','LineWidth',2) % Phase offset of 270
degrees
hold on
plot(g,Magnitude(176,1:126).*a,'y','LineWidth',2) % Phase offset of 315
degrees
hold on
plot(g,Magnitude(76,1:126).*a,'g','LineWidth',2) % Phase offset of 135
degrees
xlim([0 .8]) %Setting X axis limits
set(gca,'XTick',0:.05:.8,'FontSize',18); % Sets increments for X axis
set(gcf,'Color',[1,1,1]); % Sets Border color to white
xlabel('Position (m)','FontSize',30);
ylabel('Amplitude (nW)','FontSize',30);
%title('Amplitude vs. Position at 4GHz with Incremental Steps of .25in
','FontSize',20);
legend('135 Degree Phase Offest','270 Degree Phase Offest','315 Degree
Phase Offest');
%Magnitude(:,[4:10 16:22])=Magnitude(:,[16:22 4:10]);
%s=Magnitude;
% hold on
% Magnitude(:,[3 13])=Magnitude(:,[13 3]);

%s=swap(Magnitude,2,3,13);
%f=swap(Magnitude,2,4:10,16:22);

%csvwrite('F:\2012-2013 Research\2014 Masters Thesis\Exports\Test 13
phases.csv',[Magnitude(26,1:126);Magnitude(51,1:126);Magnitude(76,1:126
);Magnitude(101,1:126);Magnitude(126,1:126);Magnitude(151,1:126);Magnit
ude(176,1:126);Magnitude(201,1:126)]);

figure(3) % Plotting All Phase Angles (Degrees)
plot(g,Angles(26,1:126),'LineWidth',2) % Phase offset of 45 degrees
hold on
plot(g,Angles(51,1:126),'r','LineWidth',2) % Phase offset of 90 degrees
hold on
plot(g,Angles(76,1:126),'g','LineWidth',2) % Phase offset of 135
degrees
hold on
plot(g,Angles(101,1:126),'k','LineWidth',2) % Phase offset of 180
degrees
hold on

```

```

plot(g,Angles(126,1:126),'c','LineWidth',2) % Phase offset of 225
degrees
hold on
plot(g,Angles(151,1:126),'m','LineWidth',2) % Phase offset of 270
degrees
hold on
plot(g,Angles(176,1:126),'y','LineWidth',2) % Phase offset of 315
degrees
hold on
plot(g,Angles(201,1:126),':','LineWidth',2) % Phase offset of 360
degrees
xlim([0 .8]) %Setting X axis limits
set(gca,'XTick',0:.05:.8,'FontSize',18); % Sets increments for X axis
set(gcf,'Color',[1,1,1]); % Sets Border color to white
xlabel('Position (m)','FontSize',30);
ylabel('Phase Angle (degrees)','FontSize',30);
%title('Amplitude vs. Position at 4GHz with Incremental Steps of .25in
','FontSize',20);
legend('45 Degree Phase Offest','90 Degree Phase Offest','135 Degree
Phase Offest','180 Degree Phase Offest','225 Degree Phase Offest','270
Degree Phase Offest','315 Degree Phase Offest','360 Degree Phase
Offest');
%csvwrite('F:\2012-2013 Research\2014 Masters Thesis\Exports\Test 13
Angles.csv',[Angles(26,1:126);Angles(51,1:126);Angles(76,1:126);Angles(
101,1:126);Angles(126,1:126);Angles(151,1:126);Angles(176,1:126);Angles
(201,1:126)]);

figure(4) % Plotting Selected Phase Angles (Degrees) (Changed depending
on test)
plot(g,Angles(51,1:126),'r','LineWidth',2) % Phase offset of 90 degrees
hold on
plot(g,Angles(126,1:126),'c','LineWidth',2) % Phase offset of 225
degrees
hold on
plot(g,Angles(151,1:126),'m','LineWidth',2) % Phase offset of 270
degrees
xlim([0 .8]) %Setting X axis limits
set(gca,'XTick',0:.05:.8,'FontSize',18); % Sets increments for X axis
set(gcf,'Color',[1,1,1]); % Sets Border color to white
xlabel('Position (m)','FontSize',30);
ylabel('Phase Angle (degrees)','FontSize',30);
%title('Amplitude vs. Position at 4GHz with Incremental Steps of .25in
','FontSize',20);
legend('90 Degree Phase Offest','225 Degree Phase Offest','270 Degree
Phase Offest');

% figure(5) % Plotting in Radians
% plot(g,Rad(26,1:126),'LineWidth',2) % Phase offset of 45 degrees
% hold on
% plot(g,Rad(51,1:126),'r','LineWidth',2) % Phase offset of 90 degrees
% hold on
% plot(g,Rad(76,1:126),'g','LineWidth',2) % Phase offset of 135 degrees
% hold on

```

```

% plot(g,Rad(101,1:126),'k','LineWidth',2) % Phase offset of 180
degrees
% hold on
% plot(g,Rad(126,1:126),'c','LineWidth',2) % Phase offset of 225
degrees
% hold on
% plot(g,Rad(151,1:126),'m','LineWidth',2) % Phase offset of 270
degrees
% hold on
% plot(g,Rad(176,1:126),'y','LineWidth',2) % Phase offset of 315
degrees
% hold on
% plot(g,Rad(201,1:126),':','LineWidth',2) % Phase offset of 360
degrees
%
% xlim([0 .8]) %Setting X axis limits
% set(gca,'XTick',0:.05:.8,'FontSize',18); % Sets increments for X axis
% set(gcf,'Color',[1,1,1]); % Sets Border color to white
% xlabel('Position (m)','FontSize',30);
% ylabel('Phase Angle (Radians)','FontSize',30);
% %title('Amplitude vs. Position at 4GHz with Incremental Steps of
.25in ','FontSize',20);
% legend('45 Degree Phase Offest','90 Degree Phase Offest','135 Degree
Phase Offest','180 Degree Phase Offest','225 Degree Phase Offest','270
Degree Phase Offest','315 Degree Phase Offest','360 Degree Phase
Offest');
% figure(6)
% plotyy(g,Magnitude(101,1:126),g,Angles(101,1:126)) % Comparing
Magnitude and Phase Angle

```

Appendix.G.3: Function file used for all tests

```
function Megawatts = mw1( filename )

% Read columns of data according to format string.
N=1:201;
dataArray = xlsread(filename);

% Allocate imported array to column variable names
Phase = dataArray(N, 1); % Phase offset angle vector
dB = dataArray(N, 2); % Amplitude (dB) vector
Angle = dataArray(N,3);
Rad = ((Angle*pi)/180);
mW = (10.^(dB/10)); % Amplitude (mW) vector

[~, filename, ~] = fileparts(filename) ;

%Structure
Megawatts.Phase = Phase;
%Megawatts.Real = Real;
%Megawatts.Imaginary = Imaginary;
Megawatts.dB = dB;
Megawatts.Angle = Angle;
Megawatts.Rad = Rad;
Megawatts.mW = mW;
Megawatts.filename = filename;

End
```

Appendix.G.4: Code for comparing slab configurations

```
%Jonathan Razinger
%2013 Research
%3/5/14
% Comparing Tests 3, 4a and 5a (Slab Confugurations)

%Uploading Data
T3p = csvread('F:\2012-2014 Research\2014 Masters Thesis\Exports\Test 3
phases.csv');
T4ap = csvread('F:\2012-2014 Research\2014 Masters Thesis\Exports\Test
4a phases.csv');
T5ap = csvread('F:\2012-2014 Research\2014 Masters Thesis\Exports\Test
5a phases.csv');
T3a = csvread('F:\2012-2014 Research\2014 Masters Thesis\Exports\Test 3
Angles.csv');
T4aa = csvread('F:\2012-2014 Research\2014 Masters Thesis\Exports\Test
4a Angles.csv');
T5aa = csvread('F:\2012-2014 Research\2014 Masters Thesis\Exports\Test
5a Angles.csv');

g=0:.0762:.9906;% Distance increments (m), moving the bar every 3"
g1=0:.0762:.6096;% Distance increments (m), moving the bar every 3"
a=1000*ones(1,14); % Conversion to nW (Changed for antenna
configuration #2)
a1=1000*ones(1,9); % Conversion to \muW (Changed for antenna
configuration #2)

figure(1)% Comparing Antenna Configurations at Max amplitude
plot(g,T3p(4,1:14).*a,'k','LineWidth',2)%Plottnng at Max Ampitude signal
@ 180 phase offset
hold on
plot(g1,T4ap(4,1:9).*a1,'LineWidth',2) %Plottnng at Max Ampitude signal
@ 180 phase offset
hold on
plot(g1,T5ap(4,1:9).*a1,'r','LineWidth',2)%Plottnng at Max Ampitude
signal @ 180 phase offset

xlim([0 1]) %Setting X axis limits
set(gca,'XTick',0:.05:1,'FontSize',18); % Sets increments for X axis
set(gcf,'Color',[1,1,1]); % Sets Border color to white
xlabel('Position (m)','FontSize',30);
ylabel('Amplitude (\muW)','FontSize',30);
%title('Amplitude vs. Position at 4GHz with Incremental Steps of .25in
','FontSize',20);
legend('Slab Configuration #3','Slab Configuration #1','Antenna
Configuration #2');
```

Appendix.G.5: Code for comparing increment size

```
%Jonathan Razinger
%2013 Research
%3/5/14
% Comparing Tests 10 and 13 (Increment size)

%Uploading Data
T13p = csvread('F:\2012-2014 Research\2014 Masters Thesis\Exports\Test
13 phases.csv');
T10p = csvread('F:\2012-2014 Research\2014 Masters Thesis\Exports\Test
10 phases.csv');

g=0:.00635:.79375;
h=0:.012:.252;
k=.1678*ones(1,22); % Shifting test 10 data to agree with test 13 data.
a=1000000*ones(8,126); % Conversion to nW
a1=1000000*ones(8,22); % Conversion to nW
T13pn=T13p.*a;
T10pn=T10p.*a1;
figure(1)% Comparing Antenna Configurations
plot(g,T13pn(7,1:126),'r','LineWidth',2)%Plotting at Max Amplitude signal
@ 315 phase offset
hold on
plot(h+k,T10pn(3,1:22),'LineWidth',2) %Plotting at Max Amplitude signal @
180 phase offset

xlim([0 .8]) %Setting X axis limits
set(gca,'XTick',0:.05:.8,'FontSize',18); % Sets increments for X axis
set(gcf,'Color',[1,1,1]); % Sets Border color to white
xlabel('Position (m)','FontSize',30);
ylabel('Amplitude (nW)','FontSize',30);
%title('Amplitude vs. Position at 4GHz with Incremental Steps of .25in
','FontSize',20);
legend('Increment Size of .25"', 'Increment Size of .5"');
```

Appendix.G.6: Code for comparing antenna height

```
%Jonathan Razinger
%2013 Research
%3/5/14
% Comparing Tests 25 and 28 (Antenna Height)

%Uploading Data
T25p = csvread('F:\2012-2014 Research\2014 Masters Thesis\Exports\Test
25 phases.csv');
T28p = csvread('F:\2012-2014 Research\2014 Masters Thesis\Exports\Test
28 phases.csv');
T25a = csvread('F:\2012-2014 Research\2014 Masters Thesis\Exports\Test
25 Angles.csv');
T28a = csvread('F:\2012-2014 Research\2014 Masters Thesis\Exports\Test
28 Angles.csv');

g=0:.00635:.79375;% Distance increments (m), moving the rod every 1/2"
a=1000000*ones(1,126); % Conversion to nW (Changed for antenna
configuration #2)

figure(1)% Comparing Antenna Height Differences at Max Amplitude
plot(g,T25p(7,1:126).*a,'LineWidth',2) %Plotting at Max Amplitude signal
@ 315 phase offset
hold on
plot(g,T28p(5,1:126).*a,'r','LineWidth',2)%Plotting at Max Amplitude
signal @ 225 phase offset
xlim([0 .8]) %Setting X axis limits
set(gca,'XTick',0:.05:.8,'FontSize',18); % Sets increments for X axis
set(gcf,'Color',[1,1,1]); % Sets Border color to white
xlabel('Position (m)','FontSize',30);
ylabel('Amplitude (nW)','FontSize',30);
%title('Amplitude vs. Position at 4GHz with Incremental Steps of .25in
','FontSize',20);
legend('Antenna Height at 19.5"', 'Antenna Height at 26"');

figure(2)% Comparing Antenna Height Differences at 315 phase offse
plot(g,T25p(7,1:126).*a,'LineWidth',2) %Plotting Amplitude signal @ 315
phase offset
hold on
plot(g,T28p(7,1:126).*a,'r','LineWidth',2) %Plotting Amplitude signal @
315 phase offset
xlim([0 .8]) %Setting X axis limits
set(gca,'XTick',0:.05:.8,'FontSize',18); % Sets increments for X axis
set(gcf,'Color',[1,1,1]); % Sets Border color to white
xlabel('Position (m)','FontSize',30);
ylabel('Amplitude (nW)','FontSize',30);
%title('Amplitude vs. Position at 4GHz with Incremental Steps of .25in
','FontSize',20);
legend('Antenna Height at 19.5"', 'Antenna Height at 26"');
```



```

figure(3)% Comparing Antenna Height Differences at 225 phase offse
plot(g,T25p(5,1:126).*a,'LineWidth',2) %Plottnng Amplitude signal @ 255
phase offset
hold on
plot(g,T28p(5,1:126).*a,'r','LineWidth',2) %Plottnng Amplitude signal @
255 phase offset
xlim([0 .8]) %Setting X axis limits
set(gca,'XTick',0:.05:.8,'FontSize',18); % Sets increments for X axis
set(gcf,'Color',[1,1,1]); % Sets Border color to white
xlabel('Position (m)','FontSize',30);
ylabel('Amplitude (nW)','FontSize',30);
%title('Amplitude vs. Position at 4GHz with Incremental Steps of .25in
','FontSize',20);
legend('Antenna Height at 19.5"', 'Antenna Height at 26"');

```

```

figure(4)% Comparing differences in phase angles at max phase offset
plot(g,T25a(7,1:126),'LineWidth',2) %Plottnng Phase angle of signal @
315 phase offset
hold on
plot(g,T28a(5,1:126),'r','LineWidth',2) %Plottnng Phase angle of signal
@ 255 phase offset
xlim([0 .8]) %Setting X axis limits
set(gca,'XTick',0:.05:.8,'FontSize',18); % Sets increments for X axis
set(gcf,'Color',[1,1,1]); % Sets Border color to white
xlabel('Position (m)','FontSize',30);
ylabel('Phase Angle (degrees)','FontSize',30);
%title('Amplitude vs. Position at 4GHz with Incremental Steps of .25in
','FontSize',20);
legend('Antenna Height at 19.5"', 'Antenna Height at 26"');

```

```

figure(5)% Comparing differences in phase angles at 315 phase offset
plot(g,T25a(7,1:126),'LineWidth',2) %Plottnng Phase angle of signal @
315 phase offset
hold on
plot(g,T28a(7,1:126),'r','LineWidth',2) %Plottnng Phase angle of signal
@ 315 phase offset
xlim([0 .8]) %Setting X axis limits
set(gca,'XTick',0:.05:.8,'FontSize',18); % Sets increments for X axis
set(gcf,'Color',[1,1,1]); % Sets Border color to white
xlabel('Position (m)','FontSize',30);
ylabel('Phase Angle (degrees)','FontSize',30);
%title('Amplitude vs. Position at 4GHz with Incremental Steps of .25in
','FontSize',20);
legend('Antenna Height at 19.5"', 'Antenna Height at 26"');

```

Appendix.G.7: Code for comparing source frequencies

```
%Jonathan Razinger
%2013 Research
%3/5/14
% Comparing Tests 27 and 28 (Source Frequency)

%Uploading Data
T27p = csvread('F:\2012-2014 Research\2014 Masters Thesis\Exports\Test
27 phases.csv');
T28p = csvread('F:\2012-2014 Research\2014 Masters Thesis\Exports\Test
28 phases.csv');
T27a = csvread('F:\2012-2014 Research\2014 Masters Thesis\Exports\Test
27 Angles.csv');
T28a = csvread('F:\2012-2014 Research\2014 Masters Thesis\Exports\Test
28 Angles.csv');

g=0:.00635:.79375;% Distance increments (m), moving the rod every 1/2"
a=1000000*ones(1,126); % Conversion to nW (Changed for antenna
configuration #2)

figure(1)% Comparing Source Frequency Differences at Max Amplitude
plot(g,T27p(4,1:126).*a,'LineWidth',2) %Plotting at Max Amplitude signal
@ 180 phase offset
hold on
plot(g,T28p(5,1:126).*a,'r','LineWidth',2)%Plotting at Max Amplitude
signal @ 225 phase offset
% hold on
% plot(g,T27p(1,1:126),'k','LineWidth',2)%Plotting at Max Amplitude
signal @ 45 phase offset
xlim([0 .8]) %Setting X axis limits
set(gca,'XTick',0:.05:.8,'FontSize',18); % Sets increments for X axis
set(gcf,'Color',[1,1,1]); % Sets Border color to white
xlabel('Position (m)','FontSize',30);
ylabel('Amplitude (nW)','FontSize',30);
%title('Amplitude vs. Position at 4GHz with Incremental Steps of .25in
','FontSize',20);
legend('Source Frequency at 6GHz','Source Frequency at 4GHz','Source
Frequency at 6GHz 45 degree phase offset');

figure(2)% Comparing Source Frequency Differences at 180 phase offse
plot(g,T27p(4,1:126).*a,'LineWidth',2) %Plotting Amplitude signal @ 180
phase offset
hold on
plot(g,T28p(4,1:126).*a,'r','LineWidth',2) %Plotting Amplitude signal @
180 phase offset
xlim([0 .8]) %Setting X axis limits
set(gca,'XTick',0:.05:.8,'FontSize',18); % Sets increments for X axis
set(gcf,'Color',[1,1,1]); % Sets Border color to white
xlabel('Position (m)','FontSize',30);
ylabel('Amplitude (nW)','FontSize',30);
```

```

%title('Amplitude vs. Position at 4GHz with Incremental Steps of .25in
','FontSize',20);
legend('Source Frequency at 6GHz','Source Frequency at 4GHz');

figure(3)% Comparing Source Frequency Differences at 225 phase offse
plot(g,T27p(5,1:126).*a,'LineWidth',2) %Plottnng Amplitude signal @ 255
phase offset
hold on
plot(g,T28p(5,1:126).*a,'r','LineWidth',2) %Plottnng Amplitude signal @
255 phase offset
xlim([0 .8]) %Setting X axis limits
set(gca,'XTick',0:.05:.8,'FontSize',18); % Sets increments for X axis
set(gcf,'Color',[1,1,1]); % Sets Border color to white
xlabel('Position (m)','FontSize',30);
ylabel('Amplitude (nW)','FontSize',30);
%title('Amplitude vs. Position at 4GHz with Incremental Steps of .25in
','FontSize',20);
legend('Source Frequency at 6GHz','Source Frequency at 4GHz');

figure(4)% Comparing differences in phase angles at max phase offset
plot(g,T27a(4,1:126),'LineWidth',2) %Plottnng Phase angle of signal @
180 phase offset
hold on
plot(g,T28a(5,1:126),'r','LineWidth',2) %Plottnng Phase angle of signal
@ 255 phase offset
xlim([0 .8]) %Setting X axis limits
set(gca,'XTick',0:.05:.8,'FontSize',18); % Sets increments for X axis
set(gcf,'Color',[1,1,1]); % Sets Border color to white
xlabel('Position (m)','FontSize',30);
ylabel('Phase Angle (degrees)','FontSize',30);
%title('Amplitude vs. Position at 4GHz with Incremental Steps of .25in
','FontSize',20);
legend('Source Frequency at 6GHz','Source Frequency at 4GHz');

figure(5)% Comparing differences in phase angles at 180 phase offset
plot(g,T27a(4,1:126),'LineWidth',2) %Plottnng Phase angle of signal @
180 phase offset
hold on
plot(g,T28a(4,1:126),'r','LineWidth',2) %Plottnng Phase angle of signal
@ 180 phase offset
xlim([0 .8]) %Setting Xaxis limits
set(gca,'XTick',0:.05:.8,'FontSize',18); % Sets increments for X axis
set(gcf,'Color',[1,1,1]); % Sets Border color to white
xlabel('Position (m)','FontSize',30);
ylabel('Phase Angle (degrees)','FontSize',30);
%title('Amplitude vs. Position at 4GHz with Incremental Steps of .25in
','FontSize',20);
legend('Source Frequency at 6GHz','Source Frequency at 4GHz');
%% New antenna test
%4/4/14
%Using data gathered from Test 30 and 27

```

```

T30p = csvread('F:\2012-2014 Research\2014 Masters Thesis\Exports\Test
30 phases.csv');
T27p = csvread('F:\2012-2014 Research\2014 Masters Thesis\Exports\Test
27 phases.csv');

g=0:.00635:.79375;% Distance increments (m), moving the rod every 1/2"
a=1000000*ones(1,126); % Conversion to nW (Changed for antenna
configuration #2)

figure(6)% Comparing Source Frequency Differences at 180 phase offset
plot(g,T30p(4,1:126).*a,'LineWidth',2) %Plotting at Max Ampitude signal
@ 180 phase offset
hold on
plot(g,T27p(4,1:126).*a,'r','LineWidth',2)%Plotting at Max Ampitude
signal @ 180 phase offset

xlim([0 .8]) %Setting X axis limits
set(gca,'XTick',0:.05:.8,'FontSize',18); % Sets increments for X axis
set(gcf,'Color',[1,1,1]); % Sets Border color to white
xlabel('Position (m)','FontSize',30);
ylabel('Amplitude (nW)','FontSize',30);
%title('Amplitude vs. Position at 4GHz with Incremental Steps of .25in
','FontSize',20);
legend('New Source Antenna #2','Damaged Source Antenna #2');

```

Appendix.G.8: Code for comparing antenna orientations

```
%Jonathan Razinger
%2013 Research
%3/5/14
% Comparing Tests 13, 20 and 28 (Antenna Orientation)

%Uploading Data
T13p = csvread('F:\2012-2014 Research\2014 Masters Thesis\Exports\Test
13 phases.csv');
T20p = csvread('F:\2012-2014 Research\2014 Masters Thesis\Exports\Test
20 phases.csv');
T28p = csvread('F:\2012-2014 Research\2014 Masters Thesis\Exports\Test
28 phases.csv');
T20a = csvread('F:\2012-2014 Research\2014 Masters Thesis\Exports\Test
20 Angles.csv');
T28a = csvread('F:\2012-2014 Research\2014 Masters Thesis\Exports\Test
28 Angles.csv');
T13a = csvread('F:\2012-2014 Research\2014 Masters Thesis\Exports\Test
13 Angles.csv');

g=0:.00635:.79375;% Distance increments (m), moving the rod every 1/2"
a=1000000*ones(1,126); % Conversion to nW (Changed for antenna
configuration #2)
a1=1000*ones(1,126); % Conversion to \muW (Changed for antenna
configuration #2)

figure(1)% Comparing Antenna Configurations at Max amplitude
plot(g,T13p(7,1:126).*a1,'k','LineWidth',2)%Plotting at Max Amplitude
signal @ 315 phase offset
hold on
plot(g,T20p(4,1:126).*a1,'LineWidth',2) %Plotting at Max Amplitude signal
@ 180 phase offset
hold on
plot(g,T28p(5,1:126).*a1,'r','LineWidth',2)%Plotting at Max Amplitude
signal @ 225 phase offset

xlim([0 .8]) %Setting X axis limits
set(gca,'XTick',0:.05:.8,'FontSize',18); % Sets increments for X axis
set(gcf,'Color',[1,1,1]); % Sets Border color to white
xlabel('Position (m)','FontSize',30);
ylabel('Amplitude (\muW)','FontSize',30);
%title('Amplitude vs. Position at 4GHz with Incremental Steps of .25in
','FontSize',20);
legend('Antenna Configuration #1','Antenna Configuration #2','Antenna
Configuration #3');

figure(2)% Comparing Antenna Configurations #1 and #3
plot(g,T13p(7,1:126).*a,'k','LineWidth',2)%Plotting at Max Amplitude
signal @ 315 phase offset
hold on
```

```

% %plot(g,T20p(4,1:126).*a,'LineWidth',2) %Plotting at Max Amplitude
signal @ 180 phase offset
% hold on
plot(g,T28p(5,1:126).*a,'r','LineWidth',2)%Plotting at Max Amplitude
signal @ 225 phase offset

xlim([0 .8]) %Setting X axis limits
set(gca,'XTick',0:.05:.8,'FontSize',18); % Sets increments for X axis
set(gcf,'Color',[1,1,1]); % Sets Border color to white
xlabel('Position (m)','FontSize',30);
ylabel('Amplitude (nW)','FontSize',30);
%title('Amplitude vs. Position at 4GHz with Incremental Steps of .25in
','FontSize',20);
legend('Antenna Configuration #1','Antenna Configuration #3');

figure(7) %Plotting Phase Angles at 180 phase offset
a2=zeros(1,126);
a3=zeros(1,126);
a4=zeros(1,126);
r=T20a(4,1:126);
h=T13a(4,1:126);
% Manipulating Phase Angles to make the plots continuous
for n=1:126;
    if r(n)>0
        a2(n)=r(n)-540;
    end
end
for n=1:126;
    if h(n)<0
        a3(n)=r(n)+540;
    end
end
for n=1:126;
    if a3(n)>400
        a4(n)=r(n)-540;
    end
end
plot(g,T13a(4,1:126)+a3+a4,'k','LineWidth',2)%Plotting at Max Amplitude
signal @ 180 phase offset
hold on
plot(g,T20a(4,1:126)+a2,'LineWidth',2) %Plotting Phase angle of signal @
180 phase offset
hold on
plot(g,T28a(4,1:126),'r','LineWidth',2) %Plotting Phase angle of signal
@ 180 phase offset
xlim([0 .8]) %Setting X axis limits
set(gca,'XTick',0:.05:.8,'FontSize',18); % Sets increments for X axis
set(gcf,'Color',[1,1,1]); % Sets Border color to white
xlabel('Position (m)','FontSize',30);
ylabel('Phase Angle (degrees)','FontSize',30);
%title('Amplitude vs. Position at 4GHz with Incremental Steps of .25in
','FontSize',20);

```

```
legend('Antenna Configuration #1','Antenna Configuration #2','Antenna  
Configuration #3');
```

Appendix.G.9: Code for measuring the amount of antenna coupling

```
%Jonathan Razinger
%2013 Research
%3/5/14
% Test 29 Comparing S41 and S43 (Antenna Coupling/Cross talk)

%Uploading Data
s41 = csvread('F:\2012-2014 Research\2014 Masters Thesis\Exports\S41
Retest Reflection Subtract Slab.csv');
s43 = csvread('F:\2012-2014 Research\2014 Masters Thesis\Exports\S43
Retest Reflection Subtract Slab.csv');
g=0:.00635:.79375;
a=1000000*ones(1,126); % Conversion to nW
k=.0375*ones(1,126); % Half wavelength
s41r=s41.*a;
s43r=s43.*a;
plot(g,s41r,'LineWidth',2) %S41 data
hold on
plot(g,s43r,'r','LineWidth',2) %S43 data
% hold on
% plot(g+k,s41r,'g','LineWidth',2) %Plotting S41 signal with 180 degree
offset
xlim([0 .8]) %Setting X axis limits
set(gca,'XTick',0:.05:.8,'FontSize',18); % Sets increments for X axis
set(gcf,'Color',[1,1,1]); % Sets Border color to white
xlabel('Position (m)','FontSize',30);
ylabel('Amplitude (nW)','FontSize',30);
%title('Amplitude vs. Position at 4GHz with Incremental Steps of .25in
','FontSize',20);
%legend('S41','S43','S41 180 offset');
% legend('S43','S41 180 offset');
legend('S41','S43')
```


Appendix.G.10: Code for determining mutual coupling between antennas

```
%Jonathan Razinger
%2013 Research
%3/5/14
% The extent of mutual coupling between the antennas

%Uploading Data
S41f = xlsread('F:\2012-2014 Research\GPR Radar\Phase offset\Test
33\s41\full frequency sweep 7ft.csv');
S43f = xlsread('F:\2012-2014 Research\GPR Radar\Phase offset\Test
33\s43\full frequency sweep 7ft.csv');
S43c = xlsread('F:\2012-2014 Research\GPR Radar\Phase offset\Test
33\s43\full frequency sweep 4ft.csv');
F = S41f(:,1); %Frequencies
S41air=(10.^(S41f(:,4)/10))*1000; %S41 signal into air (\muW)
S41m=(10.^(S41f(:,2)/10))*1000; %S41 signal into air with metal object
at 7ft (range of array) (\muW)
S43air=(10.^(S43f(:,4)/10))*1000; %S43 signal into air (\muW)
S43m=(10.^(S43f(:,2)/10))*1000; %S43 signal into air with metal object
at 7ft (range of array) (\muW)
S43mc=(10.^(S43c(:,2)/10))*1000; %S43 signal into air with metal object
at 4ft (range of array) (\muW)

figure(1) %Comparisons of coupling at all frequencies (S41 and S43 only
coupling)
plot(F,S41air)
hold on
%plot(F,S41m,'r')
hold on
plot(F,S43air,'k')
hold on
%plot(F,S43m,'g')
xlim([0 6000000000]) %Setting X axis limits
set(gca,'XTick',0:1000000000:6000000000,'FontSize',18); % Sets
increments for X axis
set(gcf,'Color',[1,1,1]); % Sets Border color to white
xlabel('Frequency (GHz)','FontSize',30);
ylabel('Amplitude (\muW)','FontSize',30);
%title('Amplitude vs. Position at 4GHz with Incremental Steps of .25in
','FontSize',20);

figure(2) %Comparisons of coupling at all frequencies in dBm (S43)
plot(F,S43f(:,4),'LineWidth',2)
hold on
plot(F,S43f(:,2),'r','LineWidth',2)
hold on
plot(F,S43c(:,2),'k','LineWidth',2)
hold on
%plot(F,S43m,'g')
```

```

xlim([0 6000000000]) %Setting X axis limits
set(gca,'XTick',0:1000000000:6000000000,'FontSize',18); % Sets
increments for X axis
set(gcf,'Color',[1,1,1]); % Sets Border color to white
xlabel('Frequency (Hz)','FontSize',30);
ylabel('Amplitude (dBm)','FontSize',30);
legend('Signal due to Mutual Coupling','Reflection of Object at 7ft
(2.14m) + Mutual Coupling','Reflection of Object at 4ft (1.22m) +
Mutual Coupling');

figure(3) %Comparisons of coupling at all frequencies (S41)
plot(F,S41f(:,4))
hold on
plot(F,S41f(:,2),'r')
hold on
%plot(F,S43air,'k')
hold on
%plot(F,S43m,'g')
xlim([0 6000000000]) %Setting X axis limits
set(gca,'XTick',0:1000000000:6000000000,'FontSize',18); % Sets
increments for X axis
set(gcf,'Color',[1,1,1]); % Sets Border color to white
xlabel('Frequency (GHz)','FontSize',30);
ylabel('Amplitude (\muW)','FontSize',30);
%%
%Finding mean amplitude of coupling att 4GHz
S41_4g = xlsread('F:\2012-2014 Research\GPR Radar\Phase offset\Test
33\s41\4ghz.csv');
S43_4g = xlsread('F:\2012-2014 Research\GPR Radar\Phase offset\Test
33\s43\4ghz.csv');
S41_4g_air=(10.^(S41_4g(:,2)/10))*1000000; %S41 signal into air (nW)
S43_4g_air=(10.^(S43_4g(:,2)/10))*1000000; %S41 signal into air (nW)
m1=mean(S41_4g_air);
m2=mean(S43_4g_air);
%%
%Finding mean amplitude of coupling att 6GHz
S41_6g = xlsread('F:\2012-2014 Research\GPR Radar\Phase offset\Test
33\s41\6ghz.csv');
S43_6g = xlsread('F:\2012-2014 Research\GPR Radar\Phase offset\Test
33\s43\6ghz.csv');
S41_6g_air=(10.^(S41_6g(:,2)/10))*1000000; %S41 signal into air (nW)
S43_6g_air=(10.^(S43_6g(:,2)/10))*1000000; %S41 signal into air (nW)
m3=mean(S41_6g_air);
m4=mean(S43_6g_air);

```

Appendix.G.11: Code for comparing experimental S41 reflected signal to theoretical model of an S41 reflected signal with coupling

```
% Jonathan Razinger
% Comparing S41 Reflected Signal Test with Theoretical Reflected Signal
% Model with Mutual Coupling
% 4/7/14

%% Ideal Theoretical Reflected Signal

f=4E9; % Source signal frequency
c=3E8; % Speed of light
lambda=c/f; % Wavelength
d=.762; % Distance between both source antennas (m), which is 30in
yr=.5715; % Vertical distance from antennas to reflective object (m),
22.5in
x=-.6:.02:.6; % Position in the Horizontal direction
r1=sqrt((x+(d/2)).^2+(yr^2)); % Distance of antenna 1 to reflective
object
r2=sqrt((x-(d/2)).^2+(yr^2)); % Distance of antenna 2 to reflective
object
r3=d/2; % coupling distance
delta1=((2*pi*r1)/lambda); % Additional phase angles from time phase
lag
delta2=((2*pi*r2)/lambda); % Additional phase angles from time phase
lag
delta3=((2*pi*r3)/lambda); % Additional phase angles from time phase
lag for coupling

%%
figure(1)
A1=5; % Approximated Amplitude
A2=5; % Approximated Amplitude
o=.6*ones(1,61); % x-axis shift
phi1=0; % Source 1 antenna with no phase shift
%phi2=0; % Source 2 antenna with pi/4 phase shift (45 degrees)
phi2=(90*pi/180); % Source 2 antenna with pi/4 phase shift (45 degrees)
beta1=phi1+delta1; % Phase shift + additional shift from time lag
(source 1)
%beta2=0;
beta2=phi2+delta3; % Phase shift + additional shift from time lag
(source 2)
sig=A1^2+A2^2+A1*A2*(cos(beta1-beta2)+sin(beta1-
beta2))+A1*A2*(cos(beta2-beta1)+sin(beta2-beta1));
plot(x+o,sig) % Shifted Theoretical Reflected Signal with Coupling
hold on
%%
figure(2)
%Uploading Data
s41 = csvread('F:\2012-2014 Research\2014 Masters Thesis\Exports\S41
Retest Reflection Subtract Slab.csv');
```

```

s43 = csvread('F:\2012-2014 Research\2014 Masters Thesis\Exports\S43
Retest Reflection Subtract Slab.csv');
g=0:.00635:.79375; % Position
o1=50*ones(1,126); % y-axis shift
o2=transpose(50*ones(1,8));
g1=transpose(g);
a=1000000*ones(1,126); % Conversion to nW
%k=.0375*ones(1,126); % Half wavelength
s41r=s41.*a;
w=transpose(s41r+o1);
s43r=s43.*a;
plot(g,s41r+o1,'k','LineWidth',2) %S41 data
%f=excludedata(g,s41r+o1,'d',[ 0 .4 -60 0]); % Fitting curve to data
%fitobject = fit(g1,w,'power1','Exclude', f);
%d=fit(g1,w,'expl','Exclude', f);
%d=polyfit(g,s41r,2);
%f=polyval(d,g);
x1=[.3683;.4635;.5334;.5969;.6477;.6921;.743;.7874]; % Peaks of data
y=[52.03;50.45;36.51;11.26;8.331;9.376;5.8;6.238];
[h,gof,output]=fit(x1,y+o2,'exp2') % Fitting exponential curve
hold on
plot(x+o,sig,'LineWidth',2) % Shifted Theoretical Reflected Signal with
Coupling
hold on
plot(h) % Exponetial tapering curve

xlim([0 .8]) %Setting X axis limits
set(gca,'XTick',0:.05:.8,'FontSize',18); % Sets increments for X axis
set(gcf,'Color',[1,1,1]); % Sets Border color to white
xlabel('Position (m)','FontSize',30);
ylabel('Amplitude (nW)','FontSize',30);
legend('Experimental S41 Reflected Signal','Theoretical S41 with Mutual
Coupling','Tapering of Experimental S41 Reflected Signal')

```